



Crystallization of the energetic oxidizer salt ammonium dinitramide: Theoretical and experimental considerations

Promotionsschrift

zur Erlangung des akademischen Grades

Dr.-Ing.

vorgelegt dem

Zentrum für Ingenieurwissenschaften
der Martin-Luther-Universität Halle-Wittenberg

von

Frau Dipl.-Ing. Indra Fuhr

geb. am 04.01.1976 in Schwetzingen (Deutschland)

Gutachter:

1. Prof. Joachim Ulrich
2. Dr. Matthew Jones (AstraZeneca, Schweden)

Halle, 11.08.08

Verteidigungsdatum: 08.12.08

urn:nbn:de:gbv:3-000014655

[<http://nbn-resolving.de/urn/resolver.pl?urn=nbn%3Ade%3Agbv%3A3-000014655>]

Danksagung

Diese Arbeit entstand während meiner Tätigkeit als wissenschaftlicher Mitarbeiter am Fraunhofer Institut für Chemische Technologie (ICT) in Pfinztal bei Karlsruhe unter wissenschaftlicher Betreuung der Martin-Luther-Universität Halle-Wittenberg.

Ich möchte Herrn Prof. Dr.-Ing. habil. Joachim Ulrich herzlich dafür danken, dass er mir die Möglichkeit zur Promotion gegeben hat und mich als externe Doktorandin seiner Arbeitsgruppe betreut und jederzeit unterstützt hat.

Herrn Dr. Matthew Jones danke ich sehr für die wertvollen Diskussionen während der Entstehung der Arbeit und die Übernahme des Zweitgutachtens.

Herzlich bedanken möchte ich mich bei der Arbeitsgruppe von Prof. Ulrich, insbesondere bei Frau Dr.-Ing. Anke Fiebig und bei Herrn M.Sc. Caner Yürüdü, für die freundliche Aufnahme während meiner Aufenthalte an der Universität Halle und die mir entgegengebrachte Hilfsbereitschaft.

Mein besonderer Dank geht an Herr Dr. Horst Krause, meinen Produktbereichsleiter am Fraunhofer ICT. Er hat mir während der Entstehung und gesamten Dauer dieser Arbeit jederzeit seine volle Unterstützung zukommen lassen und die Arbeit damit erst ermöglicht. Hierfür möchte ich ihm sehr herzlich danken.

Herrn Prof. Dr.-Ing. Ulrich Teipel danke ich sowohl für die organisatorische als auch für die fachliche Betreuung während der Entwicklung meines Themas und während der Anfangsphase dieser Arbeit.

Herr Dr. Michael Herrmann und Herr Dr. Paul Bernd Kempa möchte ich für die ständige Diskussionsbereitschaft und Hilfsbereitschaft sowie die fachliche Betreuung am Fraunhofer ICT danken.

Frau Heike Schuppler danke ich sehr für die schnellen und präzisen thermischen Analysen meiner vielen Proben trotz erschwelter Umstände, die durch den zeitweiligen Ausfall der Messgeräte verursacht waren. Frau Maria Juez-Lorenzo und Frau Birgitt Eickershoff danke ich für ihre Geduld und Ausdauer bei der Erstellung der REM-Aufnahmen meines hygroskopischen Probenmaterials. Bei Herr Karlfred Leisinger, Herr Werner Reinhard und Herr Christoph Birke bedanke ich mich für die tatkräftige Unterstützung bei der Durchführung der Experimente.

Meinen lieben Kollegen aus Geb. 23 danke ich für ihre moralische Unterstützung, das jederzeit freundschaftliche Arbeitsklima und für die reichliche Versorgung mit Süßigkeiten aller Art besonders während der Schlussphase der Arbeit.

Eidesstattliche Erklärung

Hiermit erkläre ich an Eides Statt, dass ich die vorliegende Arbeit selbständig und ohne fremde Hilfe angefertigt habe. Andere als die angegebenen Quellen und Hilfsmittel sind nicht verwendet worden. Die in den benutzen Werken wörtlich oder inhaltlich entnommenen Stellen sind als solche kenntlich gemacht.

Indra Fuhr

Karlsruhe, den 11.08.08

Table of contents

1	Introduction.....	1
2	State of the art	3
2.1	Crystals	3
2.1.1	Crystal lattice and Miller indices	3
2.1.2	Crystal bonding	3
2.1.3	Crystal growth from solutions.....	4
2.1.4	Influencing the crystal morphology	5
2.1.5	Morphology prediction	6
2.2	Ammonium dinitramide.....	8
2.2.1	Production of ADN particles.....	8
2.2.2	Computer simulation of ammonium dinitramide (ADN).....	9
2.3	Computer simulation	11
2.3.1	Force field methods	11
2.3.2	Energy minimization	11
2.3.3	Morphology calculation: Main methods	11
3	Aim of the work	13
4	Materials and methods	14
4.1	Experimental.....	14
4.1.1	Ammonium dinitramide.....	14
4.1.2	Solvents	15
4.1.3	Electrolytic conductivity measurement.....	15
4.1.4	Solubility data.....	16
4.1.5	Crystallization.....	17
4.1.5.1	Experimental setup.....	17
4.1.5.2	Crystallization procedure	19
4.2	Computer simulation	19
4.2.1	Software	19
4.2.1.1	Discover minimization.....	19
4.2.1.2	COMPASS force field.....	19
4.2.1.3	Morphology calculation	20
4.2.2	Simulation procedure	20
4.2.2.1	Preparation of the unit cell model.....	20
4.2.2.2	Energetic consideration of the unit cell	20
4.2.2.3	Morphology calculation	20
4.2.2.4	Determination of interaction energies	21
5	Results.....	22
5.1	Simulation	22
5.1.1	Unit cell.....	22
5.1.2	Vacuum morphology	25
5.1.2.1	Minimized unit cell	25
5.1.2.2	Original unit cell	27
5.1.3	Crystal faces.....	28
5.1.4	Interactions energies.....	29
5.1.4.1	Minimized unit cell	29
5.1.4.2	Original unit cell	31
5.2	Experimental results.....	34
5.2.1	Electrolytic conductivity measurement: Characteristic curves.....	34

5.2.2	Solubility data.....	36
5.2.3	Crystallization.....	37
5.2.3.1	Natural cooling.....	37
5.2.3.2	Alcohol screening.....	38
5.2.3.3	1-propanol.....	42
5.2.3.4	1-octanol.....	49
5.2.4	Dynamic viscosity.....	59
5.2.5	X-ray powder diffraction of ADN.....	60
5.3	Comparison of simulated and experimental morphology.....	61
5.3.1	ADN / 1-propanol.....	61
5.3.2	ADN / 1-octanol.....	62
6	Discussion.....	64
6.1	The ADN unit cell.....	64
6.1.1	Geometrical setup.....	64
6.1.2	The application of the COMPASS force field to the dinitramide ion.....	65
6.1.3	Comparison of the minimized and original ADN unit cell.....	66
6.2	Computer simulation of the crystal shape of ADN.....	67
6.2.1	Vacuum morphology calculation.....	67
6.2.2	The growth faces and their interactions with building blocks and foreign molecules.....	68
6.2.3	Experimental morphology versus simulated vacuum morphology.....	70
6.3	Process monitoring.....	72
6.3.1	The application of the electrolytic conductivity measurement.....	72
6.3.1.1	Range of the measured data.....	72
6.3.1.2	Solubility data.....	74
6.3.2	Supersaturation and nucleation.....	74
6.4	Solvent crystallization of ADN.....	76
6.4.1	Choice of the solvents.....	76
6.4.2	Crystal morphology.....	76
6.4.3	Thermal analysis of recrystallized ADN.....	78
6.5	Conclusions.....	80
7	Summary.....	82
8	Zusammenfassung.....	84
9	Notations.....	86
10	References.....	89
11	Annex.....	93

1 Introduction

Ammonium dinitramide (ADN) was first synthesized in the 70s in the former USSR at the Zilinsky Institute, Moscow. It has received much attention during the past fifteen years, mainly due to its potential as an oxidizer in minimum- or reduced-smoke rocket propellants.

A solid propellant basically consists of an oxidizer, a fuel and a binder. Many types of propellants use ammonium perchlorate (AP) as an oxidizer because of its high energy, its relatively low hazards and its burn rate tailorability. The drawback of AP is the huge amount of hydrochloric acid formed during combustion. As an example, the European space launcher Ariane-5, containing 476 tons of AP-based propellant respectively, will produce 270 tons of concentrated hydrochloric acid during each launch.

ADN is currently the only high performance oxidizer that has the potential to replace AP today. As ADN does not contain any chlorine, no hydrochloric acid is produced during combustion. Because ADN propellant formulations have a higher specific impulse compared to AP propellants, the application of ADN will lead to an increase of the rocket payload.

Commercially available raw ADN is of a needle-like shape. For the incorporation into the binder matrix, a compact shape is preferred to avoid breakage of the crystals during processing. The change of the particle size distribution by damaging the crystals can influence the burning characteristics of a propellant in an uncontrollable way. Therefore, one of the challenges involved in the development of ADN propellants is the formation of suitable compact-shaped particles from the raw ADN. Progress was achieved in this field when an emulsion prilling process was established by Teipel et al. [TEI00].

Crystallization processes from solution are generally used for purification and separation of soluble solid compounds. Additionally, crystallization offers the possibility to influence the properties of the product. One important attribute of a crystalline solid is its shape. It is responsible for both material properties (e.g. bulk density) and processing behaviour. The internal crystal structure defines the molecular composition of the habit defining crystal faces. By varying the growth velocities of the individual faces, it is possible to modulate the crystal shape. The growth velocities depend on various parameters like the composition of the system including habit modifiers and impurities, temperature run and supersaturation, stirrer geometry and the stirring speed.

Nowadays, molecular modelling is a widely used tool in the field of crystallization as computing power increased during the last years. Especially for high-priced substances like pharmaceuticals, and dangerous goods like explosives, it is reasonable to reduce the experimental effort by adopting molecular modelling methods. Commercially available

simulation software, e.g. Materials Studio by Accelrys, allows the calculation of the crystal morphology based on the internal crystal structure by using different simulation methods. A direct calculation of the influence of the crystallization environment on the crystal shape is not possible until today. Different approaches are made to determine the influence of additives and solvents e.g. by Lu et al. [LU04] [LU05] and Fuhr et al. [FUH05_1].

2 State of the art

2.1 Crystals

Crystalline solids are consisting of atoms, ions or molecules as building units that are arranged in a periodic lattice. The two main properties of a crystal are homogeneity and anisotropy. Homogeneity means that a material shows the same behaviour in parallel directions. Anisotropy means that physical properties like the growth velocity or the hardness are depending on the direction in space. This is in contrast to isotropic materials (gases and liquids) whose physical properties do not depend on the direction in space [HÜT96].

2.1.1 Crystal lattice and Miller indices

The geometry of a crystal structure is represented by its repeat unit, the crystal unit cell. It is specified by three basic vectors and the three included angles [KLE98]. The sets of the three axes in particular geometrical arrangements lead to the seven crystal systems. By combining the crystal systems with the possible lattice centerings, the fourteen Bravais lattices are obtained. They describe the geometric arrangement of the lattice points, and thereby the translational symmetry of the crystal. The combination of non-translational symmetry elements (rotation, reflection, inversion and improper rotation) are leading to the 32 possible crystal classes. A crystal space group is composed of both the translational symmetry operations in addition to the operations of the crystal classes. Altogether, there are 230 distinct space groups [WIK08].

The Miller indices are used to describe the position of a crystal face related to a coordinate system. Equation 2-1 describes a plane whereas h , k and l are the reciprocal axis intercepts corresponding to the basis vectors of the unit cell [KLE98]. If a plane is parallel to a given axis its Miller indices is zero. The notation $\{hkl\}$ represents all planes or crystal faces that are parallel to the plane (hkl) [LU04].

$$\frac{x}{m} + \frac{y}{n} + \frac{z}{p} = h \cdot x + k \cdot y + l \cdot z = 1 \quad \text{Equation 2-1}$$

2.1.2 Crystal bonding

The structure of a crystal is dominated by the geometrical principles of the packing as well as by crystal-chemical interactions [KLE98]. The different types of crystalline solids are based on different types of bonds inside the crystal (Table 2-1). Ionic bonding is produced whenever an element with relatively low ionization energy is combined with an element with a relatively high electron affinity [IBA03]. Hydrogen bonds are most common between strongly electronegative atoms, but are not limited to this case alone. Van-der-Waals (VDW) interactions are always present but only significant in cases where

other types of bonding are not possible, e.g. atoms with closed electron shells or saturated molecules. The interactions are caused by arising dipole moments due to charge fluctuations in the atoms. Ionic bonding and covalent bonding are the two limiting cases. The crystal energy or lattice energy is the energy that is needed to separate the structural units at $T = 0$ K to an infinite distance from each other [VAI00]. This decomposition of the crystal structure is done by breaking the crystal bonds.

Table 2-1: Types of crystalline solids [MOR80]

type of crystal	building units	interactions
ionic	positive and negative ions	electrostatic attraction
molecular	polar molecules	Van-der-Waals forces (London and dipole-dipole attraction)
	non-polar molecules	London attraction
atom	atoms	covalent bond
metal	positive ions and movable electrons	metal bond

2.1.3 Crystal growth from solutions

A crystallization process from a crystal-free mother phase is divided into two kinetic steps: nucleation and growth.

For both steps, a supersaturated solution is required. The supersaturation is determined by referring the actual concentration c_{REAL} of a solution to the equilibrium concentration c_{EQU} at a defined temperature. Supersaturation can be achieved either by a change of temperature (cooling), the removal of solvent (mostly by evaporation) or by adding an antisolvent. Mostly, supersaturation is defined as described in Equation 2-2. The definition for the supersaturation that is used in this work is shown in Equation 2-3 [GNI93].

$$\sigma = \frac{c_{REAL} - c_{EQU}}{c_{EQU}} \quad \text{Equation 2-2}$$

$$S = \frac{c_{REAL}}{c_{EQU}} \quad \text{Equation 2-3}$$

The first step of a crystallization process is the formation of nuclei that are able to grow in a clear solution. This nucleation can occur homogeneously in the solution bulk or heterogeneously at the wall of the apparatus and especially at micro and nano particles that can not be excluded from being present in the solution [LAC99].

The second step is the growth of the nuclei in the solution whereas the crystallizing material has to be incorporated into the crystal lattice. For diffusion controlled crystal growth, the growth rate is limited by the transportation of the crystallizing material from the fluid bulk phase [GNI93].

If mass transport is forced e.g. by using a stirrer, an integration controlled growth is assumed. The two basic approaches that are made for the growth mechanisms are described in brief in the following:

The birth-and-spread (B+S) model is based on the formation of nuclei on smooth crystal growth faces. As with the three-dimensional case, two-dimensional nucleation and growth take place only when a definite minimum supersaturation is reached [LAC99]. The growth rate r_{B+S} of a crystal face is given by Equation 2-4 [GNI93]. K_{B+S} and k_{B+S} are coefficients describing the B+S-model.

$$r_{B+S} = k_{B+S} \cdot \sigma^{\frac{5}{6}} \cdot \exp\left[-\frac{K_{B+S}}{T^2} \cdot \frac{1}{\sigma}\right] \quad \text{Equation 2-4}$$

The BCF (Burton, Cabrera, Frank) model described the addition of growth units on the steps of screw dislocations. As no surface nucleation is required, growth is taking place even at low supersaturations [LU05]. The growth rate r_{BCF} is expressed in Equation 2-5 [GNI93]. K_{BCF} and k_{BCF} are coefficients describing the BCF-model.

$$r_{BCF} = k_{BCF} \cdot T \cdot \sigma^2 \cdot \tanh\left[\frac{K_{BCF}}{T} \cdot \frac{1}{\sigma}\right] \quad \text{Equation 2-5}$$

2.1.4 Influencing the crystal morphology

The crystal morphology is changing when the growth velocities of the individual crystal faces are influenced. Faces with high relative growth rates are disappearing. They are growing out of the crystal so the morphology is defined by the slow growing faces (see also Figure 2-1). Equations 2-4 and 2-5 show that the growth rates depend on the physical and chemical conditions of the system represented by the temperature, the supersaturation and the coefficients of the growth models.

It is demonstrated in different publications that supersaturation can influence the crystal morphology. Guangyu et al. [GUA06] observed the crystal shape of potassium dihydrogen phosphate grown from water for different temperature runs and different seed crystal loadings. Lu et al. [LU05] showed that the crystal shape of paracetamol (solvents: water, ethanol, acetone) is getting more compact with increasing supersaturation. For caprolactam, the opposite behaviour was observed for water as solvent.

Solvent molecules are interacting differently with the single crystal faces. As a result, they are strongly influencing the crystal shape by changing the growth rate of individual faces [DAV86]. This was proved experimentally by Fuhr et al. [FUH05_2] for the energetic material 1,1-diamino-2,2-dinitroethylene (FOX-7) and various solvents. Lu et

al. [LU05] did observe a variation of the crystal shape of paracetamol by varying the solvents.

The use of additives in crystallization processes is also a prevalent method to take influence on the crystal shape [NIE97]. For the crystallization of inorganic compounds multifunctional additives are used. They are working in a low concentration range of parts per million because an additive molecule can interact with various sites of the crystal faces at the same time. The morphology of organic crystals is influenced by tailor-made additives that are, on the one hand, similar to the crystallizing material in terms of chemical and structural properties so they are incorporated into the crystal lattice. On the other hand, the interruption of the crystal lattice requires a specific difference to the crystallizing material. The growth of a crystal face is hindered sterically, by the development of voids or a change in the lattice conformation. The minimum effective concentration is relatively high; it can be more than 10 %.

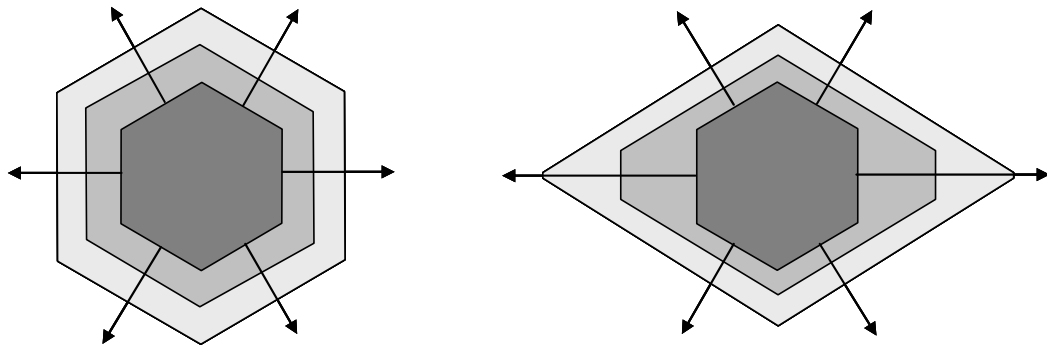


Figure 2-1: Variation of the growth rates of the crystal faces is influencing the morphology

2.1.5 Morphology prediction

The increasing interest in predicting the crystal morphology shows the importance of this field of study. This chapter gives a brief overview (see also Table 2-2) on the methods that are used for the habit prediction of various systems: crystals grown from solution and from the melt, and the influence of habit modifiers on crystal growth.

Table 2-2: Morphology prediction: Overview on literature

citation	main focus
[HAR80]	Influence of the attachment energy on the crystal habit
[BER85]	Modelling the effect of solvent on the crystal habit
[MEE91]	Morphology of ionic solids, influence of additives on the crystal shape
[LIU96]	Morphology prediction by considering growth mechanisms
[NIE97]	Shape of organic crystals influenced by additives: build-in approach
[LU04]	Influence of additives on the crystal shape: surface docking approach
[SCH04]	Improvement of the build-in approach by applying PBC-vectors
[FIE05]	Correction factor to consider additive concentrations

Hartman and Bennema [HAR80] discussed the role played by the attachment energy E_{ATT} in controlling the growth and shape of crystals growing according to different growth mechanisms. They demonstrated that for crystals growing at low supersaturations, the relative growth rate of a face is approximately proportional to its attachment energy.

Berkovitch-Yellin [BER85] studied the habit of organic crystals from known crystallographic structure and symmetry. To obtain the habit of solution grown crystals, the solvent – solute and crystal – solution interactions are considered. It was assumed that the solvent affects the habit of the crystals through preferential adsorption of solvent molecules on specific crystal faces. The remove of the solvation layer prior to the deposition of crystallizing material causes retardation of growth of these faces. Electrostatic potential maps were used for the study of the relative polarities of the various crystal faces. This information is crucial for the prediction of the habits of crystals obtained from solutions in polar or nonpolar solvents.

Meenan et al. [MEE91] predicted the crystal shape of different carbonates, sulphates and phosphates by using the BFDH method. They found out that it is difficult to modify crystal faces consisting of both cations and anions because a close topotactic relationship between the modifier and the substrate is needed for adsorption.

Liu and Bennema [LIU96] developed an approach where the relation between the relative growth rate and habit-controlling factors is derived according to crystal growth mechanisms. To calculate the relevant internal and external habit-controlling factors, a periodic bond chain analysis and an interfacial structure analysis are carried out. An excellent agreement of the predicted and experimental morphologies was achieved.

Niehörster [NIE97] worked out a method to predict the additive depending morphology of organic crystals grown from the melt. The so called “build-in” approach is based on the substitution of crystal molecules by additive molecules inside the unit cell for each symmetry position. The modified unit cells are minimized and the attachment energies are calculated. Starting from averaged attachment energies, the new theoretical morphology is constructed.

Lu [LU04] investigated the influence of additives on the crystal shape during crystal growth from the melt. She compared two different computer simulation methods: the build-in approach (developed by Niehörster [NIE97]) and the surface docking approach. The surface docking approach is analyzing the effect of additives on the individual crystal faces cleaved from the pure crystal. Strong interactions lead to a slow growth of the crystal face and therefore to a high morphological importance.

Schmiech et al. [SCH04] used the model of periodic chains of strong bonds developed by Hartman and Perdok [HAR55] to improve Niehörster’s build-in approach [NIE97] for organic crystals grown from the melt under the influence of additives. The number of bonds perpendicular or transversal to the faces of the pure crystal is determined and compared to the number of bonds of an additive influenced crystal. This is done for

each morphological important crystal face and is used as correction factor for the build-in model. In this approach, the additive concentration can not be taken into account. Fiebig et al. [FIE05] present a modelling approach to predict the crystal morphology depending on the additive concentrations for benzophenone melt crystallization. A mathematical expression was determined from experimental investigations that describes the dependencies of the aspect ratio values from the additive concentration. This expression was combined with the surface-docking approach developed by Lu [LU04] and it was used to improve the correction factor developed by Schmiech et al. [SCH04]. As a result, the concentration dependant morphology can be predicted based on the two approaches.

2.2 Ammonium dinitramide

2.2.1 Production of ADN particles

The production of ADN particles that are applicable for the use in formulations is still to be improved. This chapter gives an overview on the different processes that are used to produce ADN particles including the purification from the reaction mixture (Table 2-3).

Table 2-3: Production methods for ADN particles

citation	main focus
[MAL99]	Purification of crude ADN by recrystallization (precipitation)
[TEI00]	Emulsion crystallization process
[JOH06]	Spray crystallization of ADN
[BEN06]	Solution crystallization under the influence of additives

Malesa et al. [MAL99] investigated the separation of ADN from reaction mixture. This process included the recrystallization of crude ADN for purification reasons. The recrystallization process was mainly based on dissolving ADN in boiling ethyl acetate and cooling down the solution to -18 °C to precipitate the ADN. Different variations of this procedure have been applied. The focus of this work was put on the properties of the precipitated ADN. DSC, TGA and elementary analysis were used to analyse the thermal behaviour (melting point) and the composition of the products. Crystal size and shape was not a subject of the publication.

In 2000, Teipel et al. [TEI00] developed an emulsion crystallization process to produce spherical ADN particles. A suspension consisting of crude ADN and an anti-solvent (paraffin oil) was prepared. The mixture was heated up above the melting point of ADN and droplets of ADN are formed. By cooling down the emulsion spherical particles are obtained. Because molten ADN exhibits a strong tendency towards undercooling, crystallization must be initiated by mechanical energy input (stirrer, solid particle – droplet interaction). The particle size is mainly influenced by the size of the crude ADN.

Johansson et al. [JOH06] were using a spray prilling process for the formation of spherical ADN particles. The ADN was first melted and then atomized by spraying through a nozzle by the use of pressurized nitrogen into liquid nitrogen. The solidification of the ADN melt was only possible when the relative humidity in the working chamber was decreased. The particle size can be varied by using nozzles with different diameters.

Benazet et al. [BEN06] focused on cooling crystallization of ADN supported by growth modifiers to improve the aspect ratio of the crystals. As solvents, mixtures of ethanol and methanol are used. Calcium and magnesium salts that are soluble in ethanol and methanol can be used as growth modifiers. The anions of the salts do not influence the crystal growth of ADN. Different temperature profiles (linear, stepped profiles) are applied. The aspect ratio could be reduced from 10 (crude ADN) to 1.5 – 5. The modified crystals were used in an energetic formulation containing ADN, hexogen, aluminium and a binder material. The processability of the formulation was improved by reducing the viscosity from 1020 Pa·s (crude ADN) to 560 Pa·s (improved crystals).

2.2.2 Computer simulation of ammonium dinitramide (ADN)

ADN was also investigated by computer simulation methods to get more information about its structure and properties. A literature survey is given in Table 2-4.

Table 2-4: Literature survey: Computer simulation of ADN

citation	main focus
[IWA94]	Interactions of ADN crystal faces with different binder molecules
[CHR96]	Structure of the dinitramide anion: isolated, in solid state, in solution
[NAG98]	Visualization of important crystal faces and possible hydrogen bonds
[SOR99]	Structural properties by plane-wave ab initio calculations
[SOR01]	Hydrostatic compression effects on ADN properties
[VEL03]	Investigation of the melting of ADN
[BEA04]	Ab initio solid state heats of formation
[FUH07_01]	Calculation of the vacuum morphology and dominant faces

Iwamoto [IWA94] calculated the interactions of crystalline ADN with different types of binder materials that are used in solid propellant formulations. The crystal structure of ADN was first simulated according to its X-ray data. The charges were assigned using MOPAC 5.0. For mechanics and dynamics calculations, Discover 7.0 was used. By replicating the ADN unit cell, a large surface was created to place the binder. To get an average of the interaction energies, the binder molecules were pulled across the surface by using a lateral forcing constraint.

Christe et al. [CHR96] measured the infrared and Raman spectra of ADN in the solid state and in solution. In addition, ab initio calculations at two different levels of theory (HF/6-31G* and MP2/6-31+G*) were used to determine the geometry of the dinitramide ion. Starting from this, the infrared and Raman spectra of the dinitramide ion were calculated. The results were compared to the experimental spectra of dinitramide salts like ADN.

Nagao [NAG98] used Cerius² v.2.0 and crystallographic data obtained by Gilardi [GIL97] to build a model of the ADN unit cell. The molecular structures of the experimentally observed crystal faces were visualized. The hydrogen bonds between ammonium ion and dinitramide ion are discussed for each face. Energy calculations were not carried out in Nagao's work.

Sorescu and Thompson [SOR99] investigated the structural properties of crystalline ADN at ambient pressure. They used plane-wave ab initio calculations based on density functional theory (DFT) and the pseudopotential method with periodic boundary conditions in all three directions. They compared their results to experimental X-ray data. To describe the crystal structure in the approximation of rigid ions they developed an intermolecular potential which was composed of pairwise Lennard-Jones, hydrogen-bonding terms and Coulomb interactions. The predicted structure is in good agreement to X-ray data. No internal symmetry for the dinitramide ion was found. The hydrostatic compression effects on structural and electronic properties were also simulated [SOR01]. ADN changes its structure at about 10 GPa from monoclinic lattice to a triclinic lattice with P-1 symmetry. By increasing the pressure, a significant charge redistribution among the atoms leads to a decrease in the ionic character of ADN due to formation of new covalent O-H and N-H bonds.

Velardez et al. [VEL03] investigated the behaviour of ADN during the solid-liquid phase transition by molecular dynamic calculations. Intramolecular interactions were calculated by using the Generalized AMBER force field (GAFF) functional form. To describe intermolecular interactions (especially hydrogen bonds) properly, the model developed by Sorescu et al. [SOR99] was used.

Beaucamp et al. [BEA04] compared two different methods to estimate the solid heat of formation of ammonium salts with experimental data. The semi-empirical PM3 method did not lead to accurate results (standard error 0.67 kJ/g) due to its extensive parameterization mostly against gas-phase neutral molecules. The P2 method, based on DFT energy and atom equivalents, can be used to predict the solid heat of formation of ammonium salts including ammonium dinitramide. The cohesive energy was estimated for the experimental crystal structure by two simulation methods: the point charge model and the SCC-DFTB model.

Fuhr et al. [FUH07_1] described the setting up of an adequate ADN unit cell as a basis for morphology calculation. The vacuum morphology of ADN was calculated by using

the purely geometrical BFDH method and the growth method that is taking the attachment energies of the individual crystal faces into account.

2.3 Computer simulation

2.3.1 Force field methods

Force field methods are used to perform energy calculations on systems containing significant numbers of atoms what results in a drastic reduction of computing time compared to quantum mechanical methods [LEA01]. The energy of a system is calculated only as a function of the positions of the atomic nuclei while the electron motion is neglected. This makes force field methods inapplicable for the calculation of chemical reactions.

Force fields are empiric and consist of energy functions often making a compromise between accuracy and efficiency. They provide a simple mechanical model to calculate inter- and intramolecular energies of a system. All force fields have at least terms to calculate bond length energies, bond angle energies, torsion energies and non-bond energies like VDW-interactions, Coulomb interactions or hydrogen bonds.

Most of the force fields are working with the so-called "atom-typing" which includes information like the atomic number and which defines attributes like the hybridization.

A more precise kind of force fields are the so-called "ab initio"-force fields (ab initio = from the beginning).

2.3.2 Energy minimization

To find the most stable state of a system, the energy hyperface which is represented by the force field functions has to be examined [LEA01]. For systems with several atoms, the energy hyperface is a complex, multidimensional function with mostly more than one minimum. The requested minimum is the one with the lowest energy, the so-called global energy minimum. To identify the geometry of the system that corresponds to minimum points of the energy surface, minimization algorithms are applied.

Minimized structures also serve as starting basis for molecular dynamics calculations.

2.3.3 Morphology calculation: Main methods

Vacuum morphologies can already be simulated with commercialized programs. Materials Studio offers a module that is able to determine the morphology by using different calculation methods. A big disadvantage for all methods is that the influence of the ambiance (e.g. the solvent) is neglected. In the following, two well-established methods for the morphology prediction are introduced:

BFDH method

The BFDH (Bravais-Friedel-Donnay-Harker) method is a purely geometrical consideration only based on the lattice parameters and the symmetry [ACC04] where faces with great interplanar spacing are dominating the morphology according to Bravais [BRA13]. Due to not taking intermolecular energies into account the method is very fast, but also very inaccurate if strong interactions (e.g. electrostatic forces, H-bonds) are occurring.

Growth method

The calculation of the growth morphology is based on the attachment energy theory described by Hartman and Bennema [HAR80]. This approach attempts to simulate crystal habits as obtained under non-equilibrium growth conditions [ACC04]. The attachment energy E_{ATT} is the fraction of the total lattice energy released when a complete growth layer is attached to the growth surface [DOC91]. Faces with low attachment energies are growing more slowly and are therefore the morphologically important ones [ACC04].

3 Aim of the work

The overall aim of this work is the investigation of the crystallization behaviour of ADN with regard to influence the crystal morphology towards a more compact shape.

As the literature survey in Chapter 2.2.1 shows, only few approaches toward a modification of the crystal shape were successful in the past. The two methods that are working best in terms of particle shape are the emulsion prilling process and the spray prilling process where the particles are formed by recrystallizing melt droplets. This provides the handling of a molten explosive at a process temperature $T > T_{\text{MELT}} = 90\text{ }^{\circ}\text{C}$ what exhibits a certain endangerment. The third method is a crystallization process patented by Benazet et al. [BEN06] where different cations are used as habit modifiers to vary the growth rates of the individual crystal faces what is influencing the crystal shape.

The first objective of this work is to study the crystallization behaviour of ADN from pure solvents without using additives. It is intended to investigate if supersaturation can influence the crystal shape during the process by crystallizing ADN from different solvents. This will imply choosing suitable solvents as well as setting-up appropriate monitoring methods for surveying the crystallization process in terms of nucleation and growth. The crystal shape will be visualized by SEM and microscopy. Additionally, the recrystallized ADN will be characterized by thermal analysis methods.

The second objective is the investigation of ADN by means of molecular modelling tools. The vacuum morphologies of ADN are to be calculated and the morphology defining crystal faces and their molecular structures are to be determined. The interactions of the faces with the different molecules present in the crystallization process are to be calculated. For all energetic considerations, the commercially available force field COMPASS (by Accelrys) is tested for its applicability to ADN. To proof the quality of the computer simulation, the crystal shapes from simulation are compared to the crystals from experiments.

This study is done to figure out if solvent crystallization is an appropriate instrument to influence the crystal shape specifically to obtain ADN crystals appropriate for the use in propellant formulations. Additionally, it is tested if the prediction of the crystal morphology is possible by applying computer simulation methods.

4 Materials and methods

This chapter gives an overview on the materials and methods used in this work:

In Chapter 4.1, the raw materials are presented as well as the crystallization process, the measurement methods to determine the saturation curves and the methods that are used to survey the crystallization process.

Chapter 4.2 is dedicated to the computer simulation part of this work. The simulation software as well as the computer simulation methods for the construction and minimization of molecular structures are introduced.

Standard analysis methods that are applied are listed in Chapter 11, Table 11-4.

4.1 Experimental

4.1.1 Ammonium dinitramide

ADN is an inorganic, hygroscopic salt. Its main physical and chemical properties are listed in Table 4-1. Two batches of ammonium dinitramide (Figure 4-1: 2005-7014 and Figure 4-2: 2007-9003) were used for crystallization experiments, both provided by Eurenco Bofors, Sweden. The specifications of the two ADN charges are summarized in Chapter 11, Table 11-1. The classification of ADN as an explosive material requires a special infrastructure for storing, handling and processing. Experiments are all done under safety and are remote controlled.

Table 4-1: Properties of ADN

molecular formula	$\text{NH}_4\text{N}(\text{NO}_2)_2$	crystal system	monoclinic
molar mass	124.06 g/mol	space group	$P2_1/c$ [RIT03]
classification	1.1 explosive	lattice parameters	$a = 6.908 \text{ \AA}$
oxygen balance	+25.79%		$b = 11.895 \text{ \AA}$
colour	transparent		$c = 5.638 \text{ \AA}$
friction sensitivity	54 N [HEI04]		$\beta = 100.278^\circ$
impact sensitivity	4 Nm [HEI04]		(see also Chapter 5.1.1)
T_{MELT}	91-92 °C	density	1.807 g/cm ³

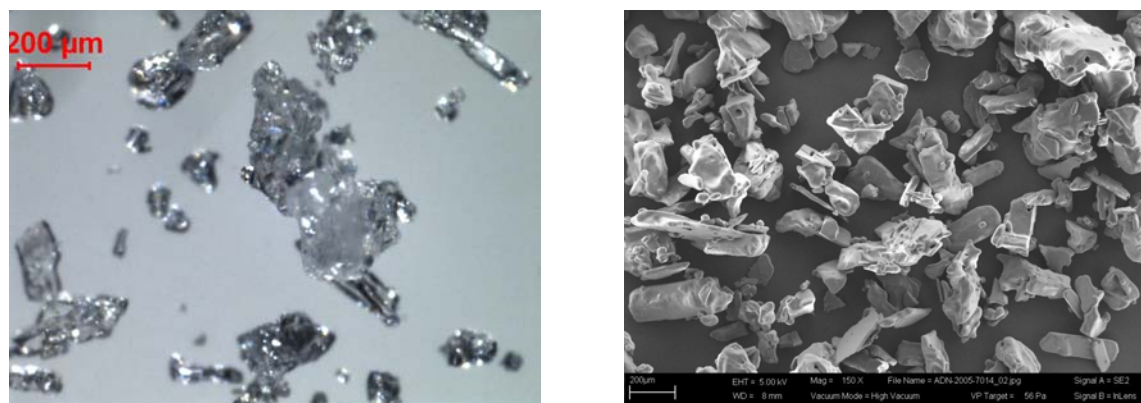


Figure 4-1: ADN 2005-7014: Microscope and SEM pictures

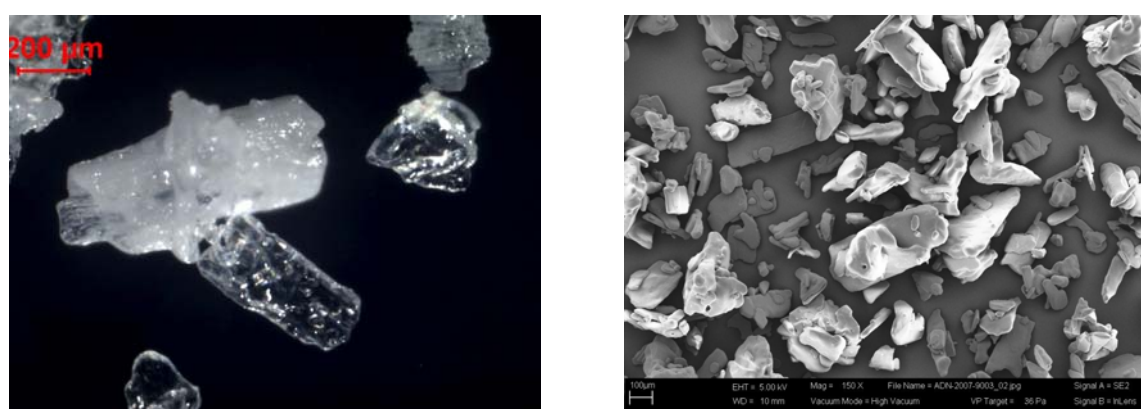


Figure 4-2: ADN 2007-9003: Microscope and SEM pictures

4.1.2 Solvents

For this work, different alcohols (1-propanol, 2-propanol, 1-pentanol and 1-octanol) were used as solvents for ADN. All alcohols were bought from Merck. The product specifications are shown in Chapter 11, Table 11-2.

4.1.3 Electrolytic conductivity measurement

Electrolytic conductivity (EC) measurement was used for comparing the different ADN charges (2005-7014 and 2007-9003), for the determination of the solubility curves and for the process monitoring of the crystallization process where EC was serving as a measure for supersaturation.

The EC measurement was carried out by using a measuring device consisting of a TetraCon® 325 as probe, a MultiLab 540 as measurement device and the software Achat II Version 1.04 for continuous data collection. The specification of TetraCon® 325 is shown in Chapter 11, Table 11-3. The advantage of the 4-electrode design of TetraCon® 325 is the non-sensitivity to faults like polarization effects, long connecting units and fouling [JUM].

4.1.4 Solubility data

The solubility data of ADN in 1-propanol and 1-octanol was determined at temperatures in the range of 20 °C to 40 °C in 2.5 °C steps. For each temperature, a suspension of ADN and the solvent was provided in a jacket vessel the way that an excess of ADN was always present. A magnetic stirrer was used to homogenize the suspension. Temperature control was done by using a PT100 as temperature sensor, placed inside the suspension, in combination with a Lauda RC6 thermostat.

The EC was measured continuously to survey the solvation process. The equilibration time was chosen the way that the electrolytic conductivity was constant. When constant EC was reached, the magnetic stirrer was turned off to get the EC of the particle-free solution after the sedimentation of the solid.

To determine the ADN concentration of the saturated solutions, two different methods were applied:

For the first method, the electrolytic conductivity of the saturated, particle-free solutions EC_{EQU} was used as a measure for the mass concentration of ADN. The concentration-dependant EC-values were determined for undersaturated solutions at constant temperatures. By extrapolating these curves, the concentrations of the saturated solutions c_{EQU} were determined for each temperature. The principle of this method is visualized in Figure 4-3.

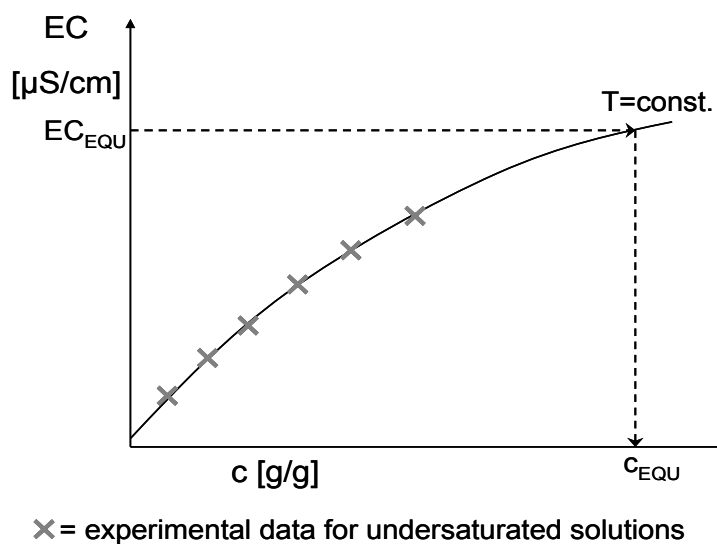


Figure 4-3: Determination of the concentration of saturated solutions from EC measurements

The second method involves taking samples of the saturated, particle-free solutions at defined temperatures with a defined mass m_{SOLUTION} . After evaporation the solvent, the mass of the remaining ADN m_{ADN} was determined. The mass concentration c_{EQU} of ADN

was defined by the quotient of m_{ADN} and the amount of evaporated solvent $m_{SOLVENT}$ according to Equation 4-1.

$$c_{EQU} = \frac{m_{ADN}}{m_{SOLVENT}} = \frac{m_{ADN}}{m_{SOLUTION} - m_{ADN}} \quad \text{Equation 4-1}$$

4.1.5 Crystallization

4.1.5.1 Experimental setup

All crystallization experiments were carried out in an air-conditioned safety working room. The relative humidity was 30 %, the temperature was 20 – 22 °C.

Two experimental setups have been used for the crystallization processes:

The small scale experimental setup consists of a 250 mL jacket vessel made of glass. It is covered with a lid made of polytetrafluorethylene (PTFE). The lid provides lead-throughs for the EC probe, the stirrer and the PT100. A propeller stirrer is used for homogenization. The stirrer motor is equipped with a time switch that allows a periodic stoppage of the stirrer. The experimental and measurement setup is shown in Figure 4-4.

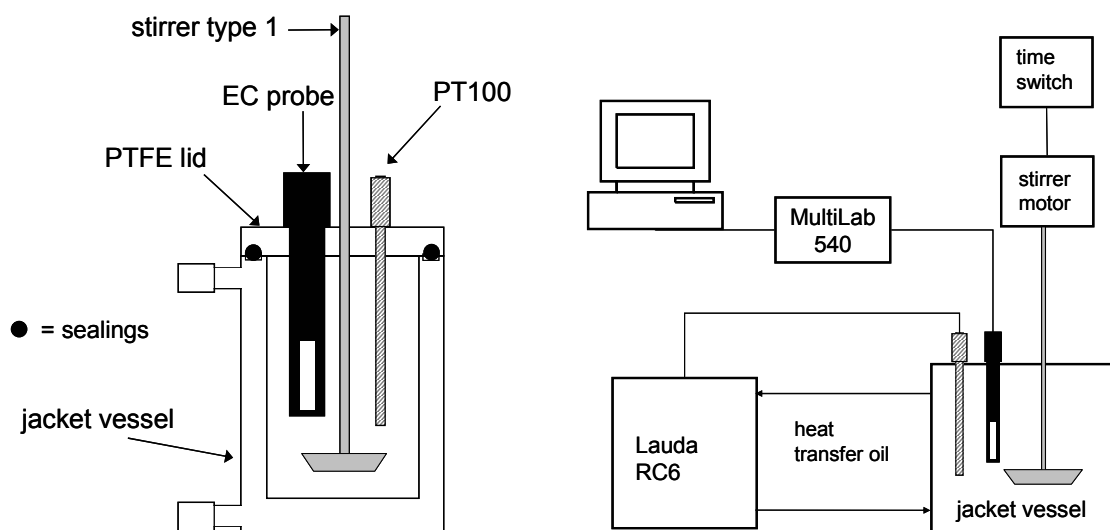


Figure 4-4: Small scale crystallization reactor (left); measurement setup (right)

The large scale setup scheme of the crystallization reactor is visualized in Figure 4-5 on the left hand side. It consists of a 600 mL jacket vessel made of glass that is covered with a lid made of PTFE. The lid provides o-ring sealed lead-throughs for the EC probe, a probe for the laser backscattering (Lasentec FBRM) and the PT100 thermocouple to minimize evaporation of the solvent during the crystallization process. The lead-through for the stirrer is not o-ring sealed but it provides a tight fit that allows the stirrer to turn while solvent evaporation is reduced. A filling orifice offers the possibility to take samples during the process and to add e.g. additives. Figure 4-5 (right) shows the

measuring setup. Both, the Lasentec and the EC data are collected continuously by a computer. The stirrer motor is equipped with a time switch.

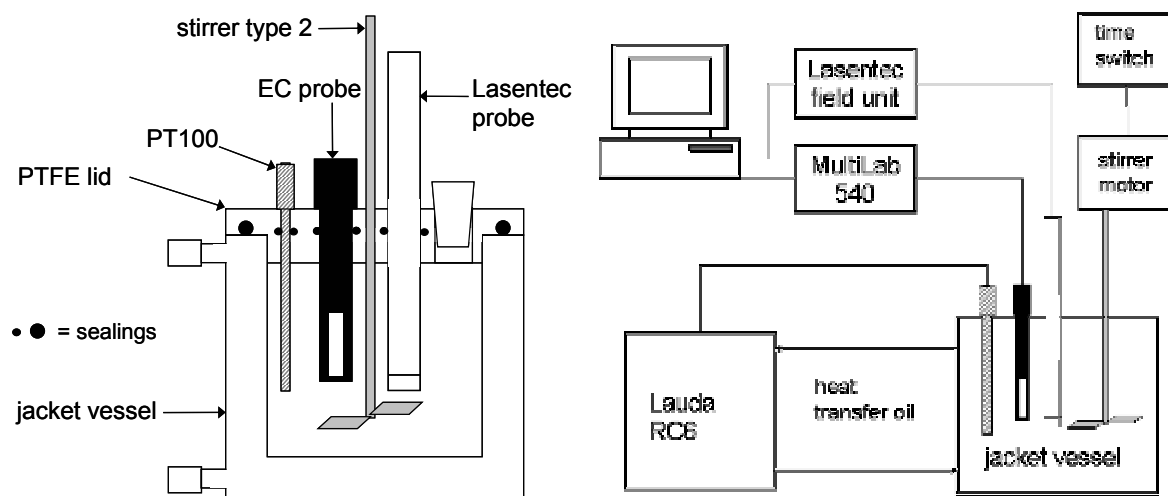


Figure 4-5: Large scale crystallization reactor (left); measurement setup (right)

A blade stirrer and a propeller stirrer are used for the experiments. The stirrer types are schematically displayed in Figure 4-6. A comparison of the two setups is given in Table 4-2.

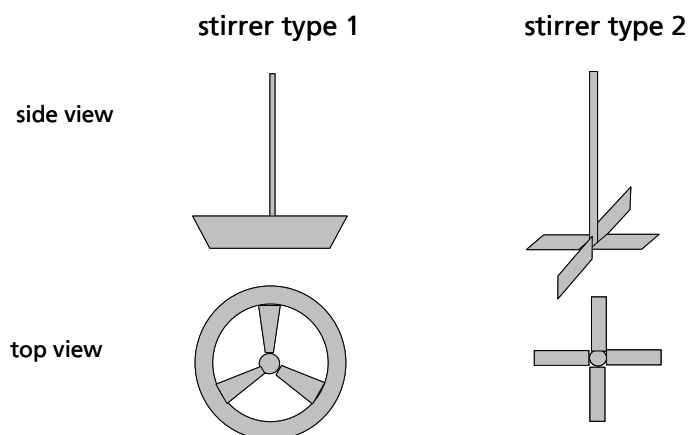


Figure 4-6: Types of stirrers used for the crystallization experiments

Table 4-2: Comparison of the experimental setups

	small scale	large scale
V_{VESSEL}	250 mL	600 mL
EC measurement	yes	yes
Laser backscattering	not possible	yes
stirrer type	type 1 impeller stirrer with 3 blades inclination angle approx. 45°	type 2 propeller stirrer with 4 blades blades distorted
stirrer speed	400 min ⁻¹	400 min ⁻¹

4.1.5.2 Crystallization procedure

Batch cooling crystallization experiments of ADN from different alcohols were carried out.

The ADN concentration that is used for a crystallization process is defined by the solubility curves and the chosen saturation temperature. Both, ADN and solvent are filled into the jacket vessel. The vessel is closed with the lid and the measurement probes are installed. The temperature run is programmed the way that the ADN-solvent mixture is heated above saturation temperature to ensure the complete dissolution of the solid. After reducing temperature to the saturation temperature $T_{SAT} = 40\text{ }^{\circ}\text{C}$, the cooling of the solution is started with a defined cooling rate. The cooling is ended when $T = 20\text{ }^{\circ}\text{C}$ is reached. After a relaxation phase of 1 h, the experiment is finished.

Because the electrolytic conductivity measurement is interfering with crystals that are present in the slot of the EC probe, the stirrer is stopped periodically (9 min ON, 1 min OFF) to let the ADN crystals sediment. After the crystallization process, the ADN crystals are filtered, washed with iso-heptane and dried in a vacuum dryer.

4.2 Computer simulation

4.2.1 Software

The simulation software that is used in this work is Materials Studio (version 3.1 and version 3.2, by Accelrys) and Gaussian 03.

Materials Studio is a modular program package that offers modules for different kinds of simulation tasks. Chapters 4.2.1.1 to 4.2.1.3. specify the most frequently used simulation methods provided by Materials Studio.

Gaussian 03 is an ab-initio program that allows the calculation of energies, molecular structures and vibration frequencies of molecular structures based on quantum mechanics. The DFT method B3LYP and the basis set 6-13G(d,p) was used in this work.

4.2.1.1 Discover minimization

The minimization of molecular models is done by means of the Discover minimization module. The appropriate minimization method is chosen automatically by the Smart Minimizer at appropriate times of the process. The methods that are provided by Discover are Steepest Descent, Conjugate Gradient and Newton Methods.

4.2.1.2 COMPASS force field

The ab initio force field COMPASS (= Condensed-Phase Optimized Molecular Potentials for Atomistic Simulation Studies) from Accelrys is applied for all energy calculations. [ACC04] It is the first ab initio-based force field that is parameterized by using extensive data for molecules in the condensed phase. Consequently, COMPASS is able to make accurate predictions of structural, conformational, vibrational, cohesive and

thermophysical properties for a broad range of compounds both in isolation and condensed phase.

4.2.1.3 Morphology calculation

The Morphology module allows the calculation of vacuum morphologies based on the crystal structure. Three calculation methods are applicable: The BFDH morphology, the growth morphology and the equilibrium morphology. It is also possible to generate new crystal habits by varying properties like the centre-to-face distance.

4.2.2 Simulation procedure

4.2.2.1 Preparation of the unit cell model

The ADN unit cell serves as basis for all computer simulation. It is constructed by combining the lattice parameters determined at ANKA (Angströmquelle Karlsruhe) with the atomic positions reported by Gilardi [GIL97] (see also Chapter 11, Table 11-5).

The first step of the energy calculation is to assign the bond types for each bond and the force field type for each atom whereas the force field types depend on the intramolecular bonds of the atoms and their neighbor atoms. Then, the atomic charges are calculated. For the ammonium ion, the atomic charges are calculated with the COMPASS force field. Because the COMPASS force field was not capable to calculate the atomic charges of the dinitramide ion properly, the charges are assigned by using Gaussian 03; the results are compared to literature data. These atomic charges are used for all further energetic calculations; they are kept constant during the simulation.

4.2.2.2 Energetic consideration of the unit cell

The minimization of the unit cell is done to obtain the energetically optimized crystal structure of ADN. During the minimization procedure, the unit cell dimensions are fixed and the atoms are allowed to move. Because of the periodicity of crystal lattices, the Ewald summation is chosen for the calculation of VDW and Coulomb interactions. The minimized unit cell is the basis for the cleaving of the morphological important crystal faces.

4.2.2.3 Morphology calculation

The vacuum morphology of ADN is calculated on the basis of the energetically minimized crystal structure. The morphology module of Materials Studio is used for this task. Both the BFDH morphology and the growth morphology are calculated. For the determination of the growth morphology COMPASS is used as force field. The resulting morphologies serve as the basis for the consideration of the effect of solvents on the crystal growth. The simulated crystal shapes are also compared to ADN crystals obtained from different solvents by considering the included angles of the crystal faces.

4.2.2.4 Determination of interaction energies

To determine the influence of additives (e.g. solvent molecules and ions) on the crystal morphology, the interaction energy of these additional molecules with the crystal faces is used as a measure.

The crystal faces of morphological importance are identified by the previously calculated BFDH and growth morphologies. By cleaving the crystal faces (hkl), a visualization of their molecular structure is received. A vacuum slab is attached to the cleaved faces to provide a vacuum volume where additive molecules can be inserted. The additive molecules are placed on the different lattice positions of the dinitramide and the ammonium ion as starting position for the energy minimization. The minimization is done by means of the Discover Minimization module of MS. The interaction energy of additives and the crystal face is calculated according to Equation 4-2

$$\Delta E_{SYSTEM} = -(E_{FACE} + E_{SOLVENT}) + E_{TOTAL} \quad \text{Equation 4-2}$$

with ΔE_{SYSTEM} = Energy difference after attaching the solvent to the face

E_{FACE} = Energy of the cleaved crystal face

$E_{SOLVENT}$ = Energy of the solvent molecule

E_{TOTAL} = Energy of the system consisting of the crystal face and the additive molecule

5 Results

5.1 Simulation

5.1.1 Unit cell

Crystallographic data of ADN are available in a broad temperature range (Table 5-1). Östmark et al. [ÖST00] showed that density decreases linearly with increasing temperature. For room temperature (295 K) the density measured by ICT/ANKA fits best to the density data provided by Gilardi et al. [GIL97] and Ritchie et al. [RIT03] (Figure 5-1). The atom positions are given by Gidasov [GID95] and Gilardi et al. [GIL97]. The atom positions given by Gilardi et al. are combined with the lattice parameters measured by ICT/ANKA to create a basic geometric model of the ADN unit cell.

Table 5-1: Comparison of crystallographic data of ADN

data from	[GID95]	[GIL97]	[ÖST00]	[RIT03]	ICT / ANKA
temperature	-	223 K	293 K	90 K	295 K
radiation	-	Mo K α	Mo K α	Mo K α	synchrotron
a [Å]	6.84	6.914(1)	5.6228	6.933(1)	6.908
b [Å]	11.90	11.787(3)	11.8750	11.603(1)	11.895
c [Å]	5.61	5.614(1)	6.8954	5.567(1)	5.638
β [°]	99.8	100.40(2)	100.17	100.58	100.278
density [g/cm ³]	1.831	1.831	1.8184	1.872	1.807
atom positions	✓	✓	-	-	-

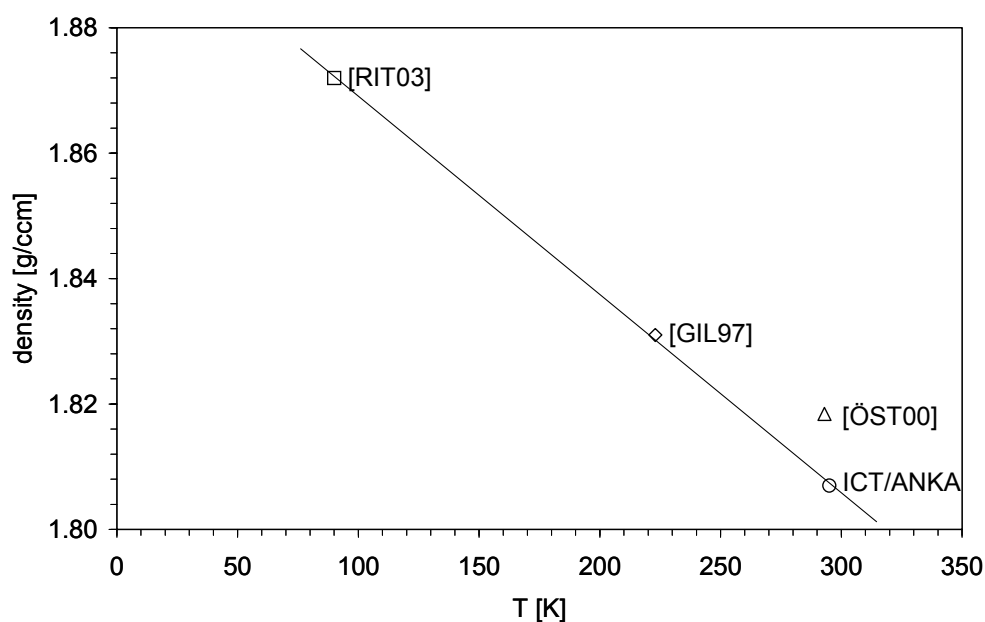


Figure 5-1: ADN densities at different temperatures

The next step was the energy minimization of the unit cell by using the COMPASS force field. The results were not satisfying in terms of the calculated force field types and atomic charges of the atoms of the dinitramide ion. The total charge $q_{\text{DN,COMPASS}}$ of the dinitramide ion (DN) was $q_{\text{DN,COMPASS}} = 0$ instead of $q_{\text{DN}} = -1$. Therefore, the dinitramide ion (Figure 5-2) was examined separately by density functional theory (DFT) methods. The whole procedure is described in detail by Fuhr et al. [FUH07_01]. The atomic charges $q_{\text{DN,DFT}}$ of the dinitramide ion resulting from DFT calculation are listed in Table 5-2 together with the atomic charges published by Ritchie et al. [RIT03] and Nagao [NAG98]. For all further simulation work, atomic charges $q_{\text{DN,DFT}}$ are used. The intramolecular bonds of the dinitramide ion are set to partial double bonds. The geometry of the dinitramide ion before and after minimization of the unit cell is described by the bond lengths d_{BOND} , the bond angles α_{BOND} and the torsion angles α_{TORSION} . (Table 5-3 to 5-5). The minimized unit cell is visualized in Figure 5-3. For comparison, the unit cell geometry published by Gilardi et al. [GIL97] is displayed in Figure 5-4.

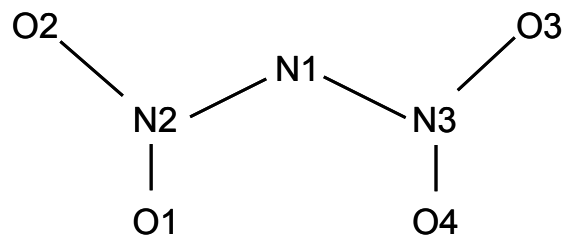


Figure 5-2 : Dinitramide ion, schematic

Table 5-2 : Dinitramide ion, atomic charges

	N1	N2	N3	O1	O2	O3	O4
FFT	n2a	n3o	n3o	o12	o12	o12	o12
$q_{\text{DN,DFT}}$ [e]	-0.242	0.559	0.559	-0.461	-0.477	-0.477	-0.461
q^* [e]	-0.18	0.69	0.67	-0.54	-0.55	-0.55	-0.55
q^{**} [e]	-0.47	0.48	0.45	-0.28	-0.43	-0.3	-0.45

*[RIT03] **[NAG98]

Table 5-3: Dinitramide ion: Bond lengths

d_{BOND} [Å]	after minimization (DFT)	before minimization [GIL97]
N1 – N2	1.342	1.359
N1 – N3	1.343	1.376
N2 – O1	1.213	1.223
N2 – O2	1.214	1.253
N3 – O3	1.216	1.236
N3 – O4	1.213	1.227

Table 5-4: Dinitramide ion: Bond angles

α_{BOND} [°]	after minimization (DFT)	before minimization [GIL97]
N2 – N1 – N3	118.05	113.19
N1 – N2 – O2	108.20	112.40
N1 – N2 – O1	110.59	125.14
N1 – N3 – O3	106.76	113.03
N1 – N3 – O4	108.66	123.38
O3 – N3 – O4	126.26	123.34
O1 – N2 – O2	125.14	122.18

Table 5-5: Dinitramide ion: Torsion angles

α_{TORSION} [°]	after minimization (DFT)	before minimization [GIL97]
N3 – N1 – N2 – O1	-63.01	-23.74
N3 – N1 – N2 – O2	156.57	162.19
N2 – N1 – N3 – O3	175.69	157.24
N2 – N1 – N3 – O4	-45.39	-28.27

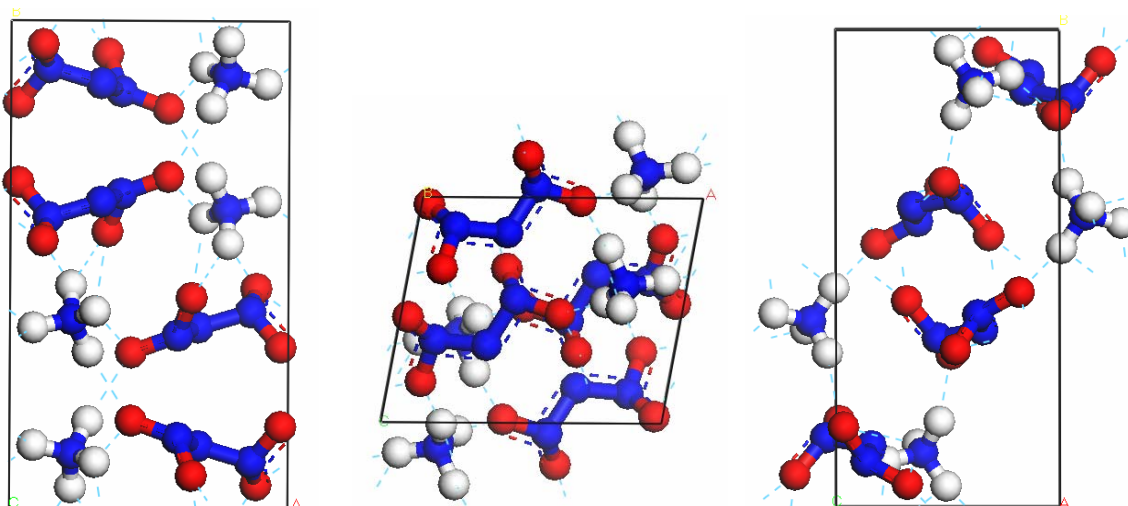


Figure 5-3: Minimized ADN unit cell: projection in (001), (010), (100) direction

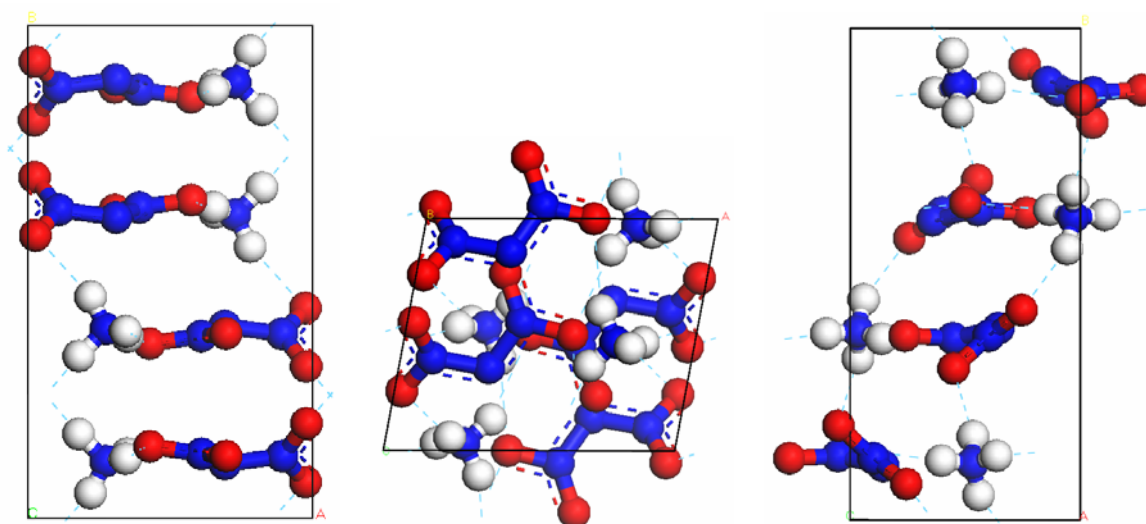


Figure 5-4: ADN unit cell, geometry from experiment [GIL97], same projections as Figure 5-3

5.1.2 Vacuum morphology

5.1.2.1 Minimized unit cell

Starting from the minimized ADN unit cell (Figure 5-3), the vacuum morphology was calculated using the purely geometric BFDH method (Figure 5-5) and the growth morphology method (Figure 5-6) where energetic considerations are made. Table 5-6 summarizes the ratio of the appearing crystal faces, their center-to-face distances and their corresponding lattice spacing d_{hkl} . The attachment energies E_{ATT} of the individual crystal faces are also given.

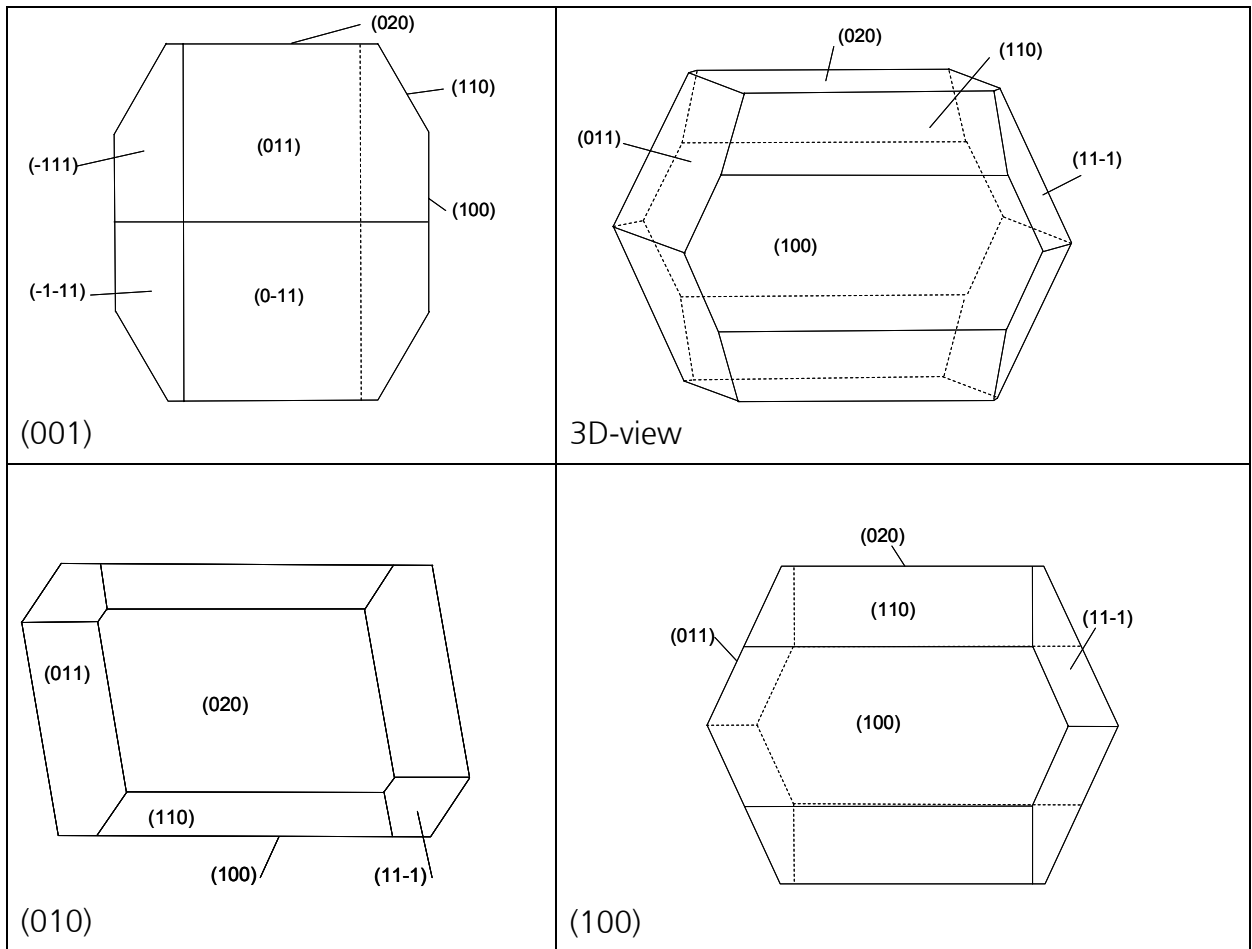


Figure 5-5: Minimized unit cell: Vacuum morphology based on BFDH method

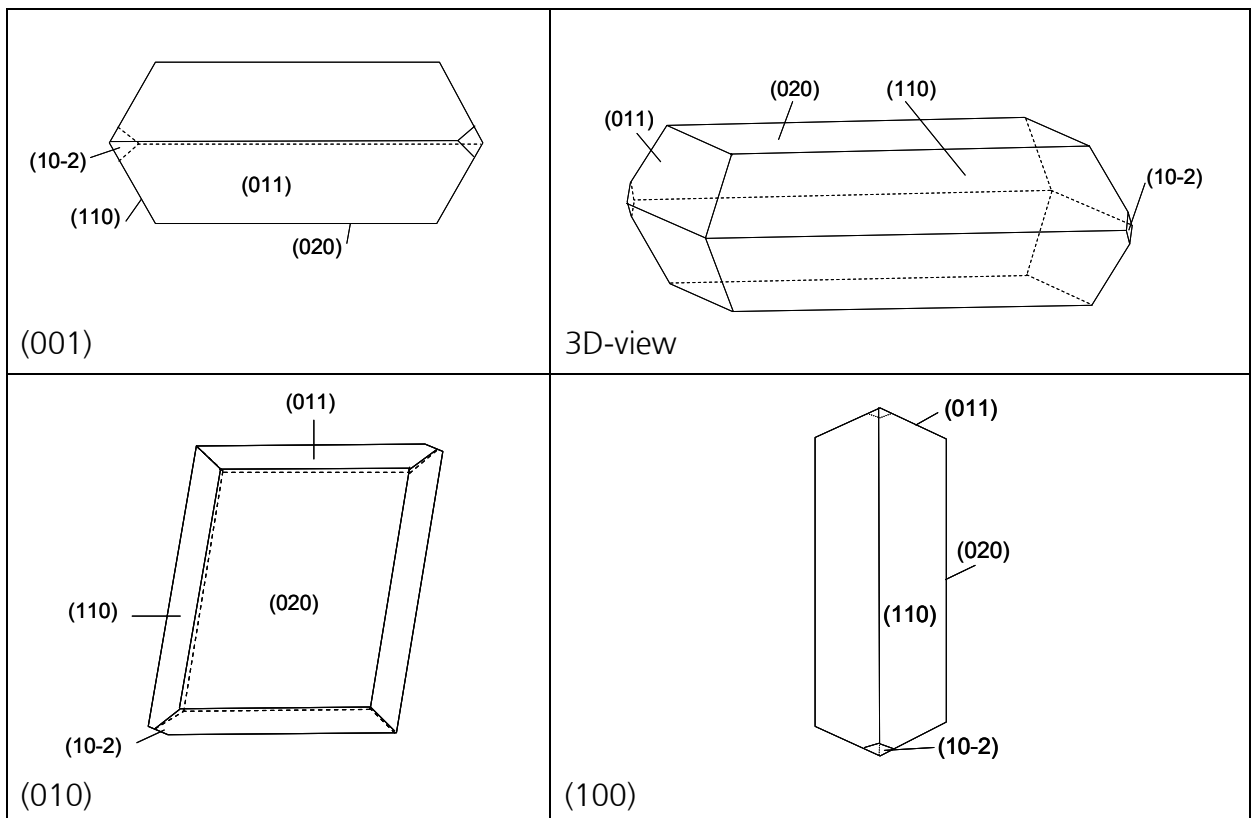


Figure 5-6: Minimized unit cell: Vacuum morphology based on growth method

Table 5-6: Minimized unit cell: Face list

face	d_{hkl} [Å]	BFDH		growth		
		%	center-to-face	%	center-to-face	E_{ATT} [kJ/mol]
(1 0 0)	6.797	21.38	14.71	0	112.80	-472.26
(0 2 0)	5.947	20.40	16.81	43.74	35.82	-149.97
(1 1 0)	5.902	20.46	16.94	31.03	73.39	-307.26
(0 1 1)	5.028	29.62	19.89	25.00	87.21	-364.76
(1 1 -1)	4.396	8.13	22.74	0	127.99	-535.87
(1 0 -2)	2.745	0	36.43	0.23	123.86	-518.57

5.1.2.2 Original unit cell

The BFDH and the growth morphology were additionally calculated for the original unit cell geometry. The lattice parameters and the symmetry as well as the atomic charges and the bond types are the same as for the minimized unit cell. The only difference is that no minimization was done and therefore the atom positions remain those published by Gilardi et al. [GIL97]. In Table 5-7 the faces of the calculated morphologies, their geometrical properties and the attachment energies are listed. The BFDH morphology is not illustrated here because it is the same as for the minimized unit cell (Figure 5-5) with only small variations. Figure 5-7 shows the growth morphology obtained from the original unit cell.

Table 5-7: Original unit cell: Face list

face	d_{hkl} [Å]	BFDH		growth		
		%	center-to-face	%	center-to-face	E_{ATT} [kJ/mol]
(1 0 0)	6.800	21.53	14.70	0	142.26	-3044.58
(0 2 0)	5.893	20.10	16.97	52.04	27.54	-115.24
(1 1 0)	5.890	20.61	16.98	21.54	76.28	-318.85
(0 1 1)	5.000	29.51	20.00	21.25	74.30	-310.57
(1 1 -1)	4.385	8.26	22.80	2.91	106.48	-445.09
(1 1 1)	3.746	0	26.68	2.25	93.97	-392.79

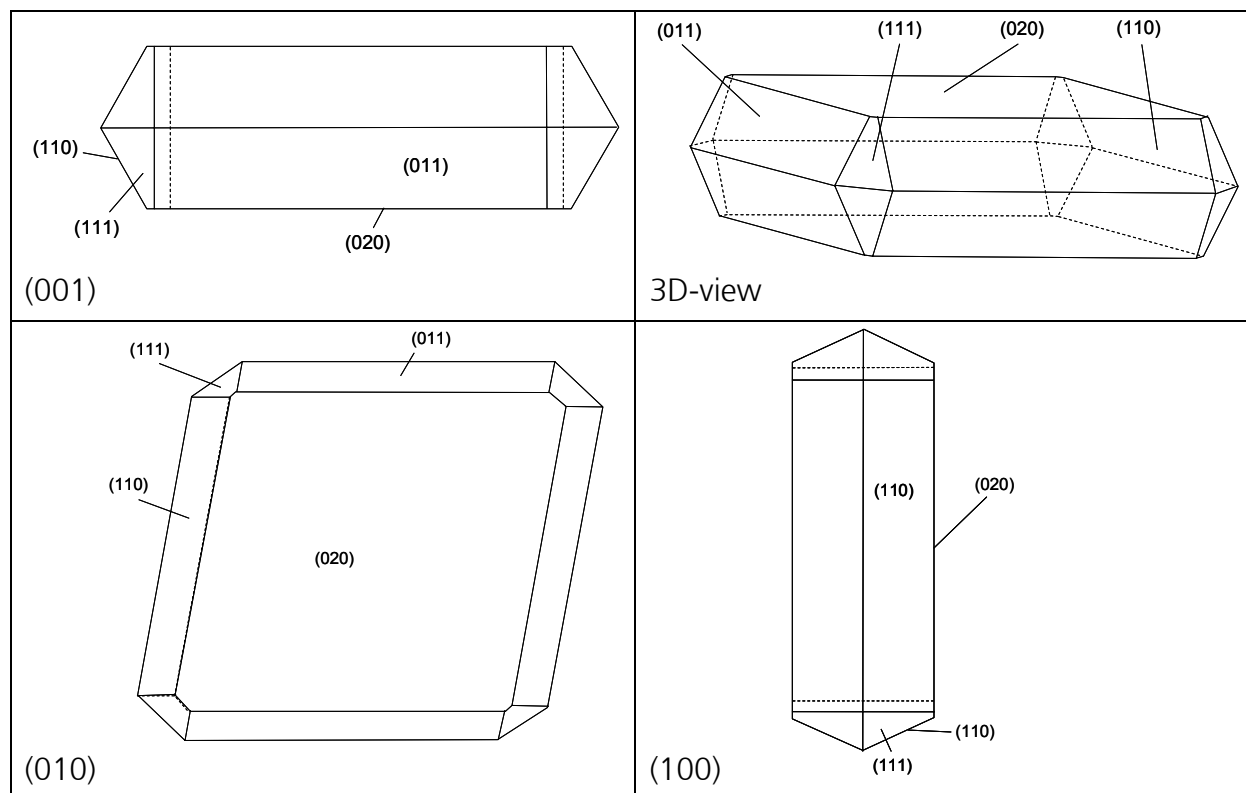


Figure 5-7: Original unit cell: Vacuum morphology based on the growth method

5.1.3 Crystal faces

The molecular structures of the crystal faces resulting from the vacuum morphology calculations are visualized in Figure 5-8 to 5-10. In addition to the faces resulting from the morphology calculations, the (002)-face is displayed because it is defined by the unit cell vectors [100] and [010].

There are two types of crystal faces present in ADN. The first type consists of layers that are built of both the ammonium ion (AM) and the dinitramide ion (DN). These layers have an overall charge of zero and provide a smooth topology. The second type consists of alternating positive and negative charged layers build from either AM or DN. In contrast to the first type, their surface topology is rough.

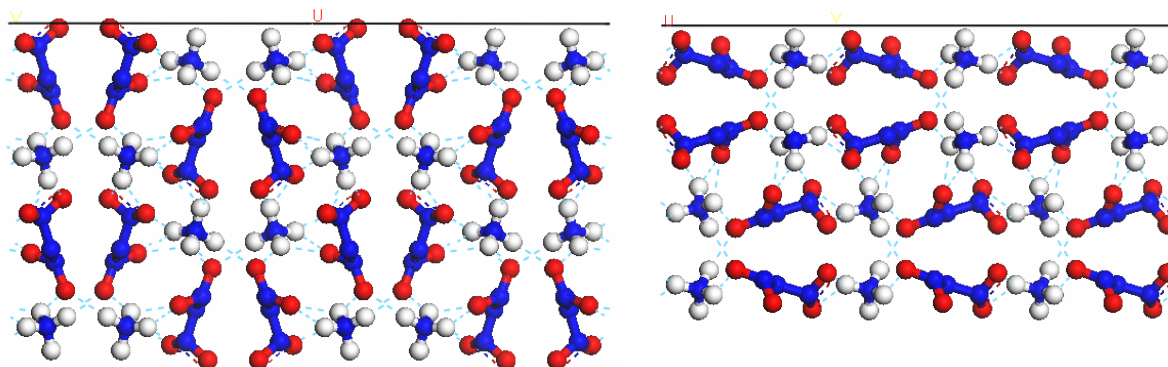


Figure 5-8: left: (100)-face; right: (020)-face: crystal layers consisting of both AM and DN ions, layers are neutral in charge, smooth topology

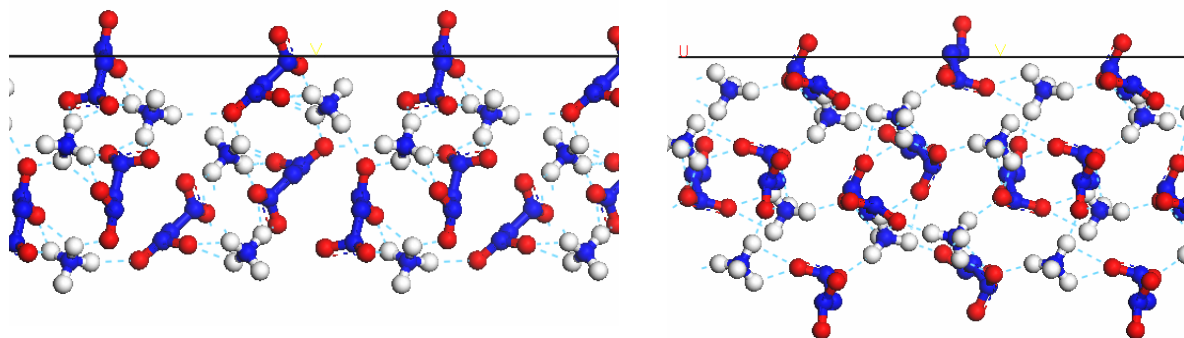


Figure 5-9: left: (110) face; right: (011) face: alternating positive and negative charged layers resulting in two configurations for each face, rough topology

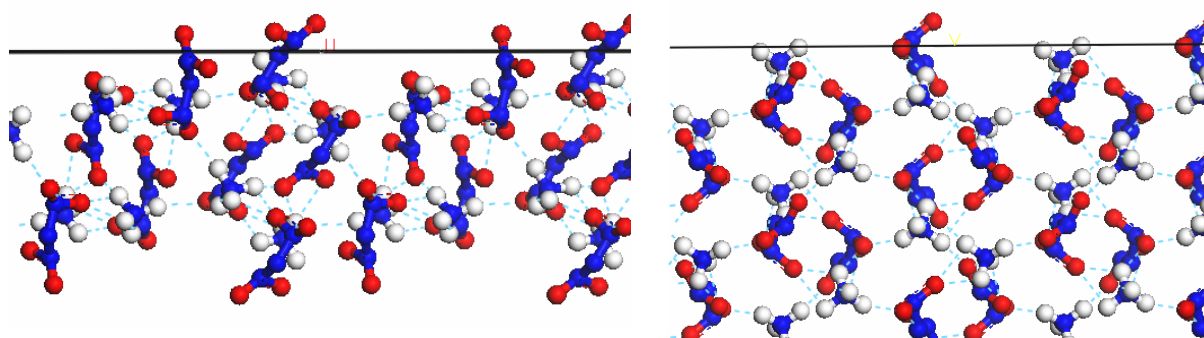


Figure 5-10: left: (11-1) face consists of two differently charged layers, one with a surplus of AM ions, one with a surplus of DN ion. Right: (002) face, neutral layers, smooth topology

5.1.4 Interactions energies

5.1.4.1 Minimized unit cell

The calculation of the interaction energies was done on the basis of the minimized unit cell. The solvent molecules 1-propanol and 1-octanol as well as the dinitramide ion and the ammonium ion were regarded as additives during the crystallization process. The additives were placed on the different lattice positions of the dinitramide ion or ammonium ion of the crystal faces (Table 5-8). Potassium is also considered an additive because it is present in both ADN batches as an impurity. For each combination of crystal face and additive the minimum (MIN), maximum (MAX) and average (AV) interaction energies are determined. For the faces (110), (011) and (11-1), both possible layers are taken into account.

Figure 5-11 shows the interaction energies of the crystal faces and the solvent molecules. The interaction energies are in a range of -220 kJ/mol to -22 kJ/mol for the different faces. The interaction energies of the solvent molecules 1-octanol and 1-propanol with the crystal faces are in the same range, there is no significant difference for the two substances when the same lattice position is examined. Faces that consist of two different crystal layers show a higher absolute value of the interaction energy if the

additive molecule is placed on a dinitramide ion position than if it is placed on an ammonium ion position.

Figure 5-12 shows the interaction energies of the crystal faces with the dinitramide ion and the ammonium ion that are substituted by the solvent molecules in the previous calculations. The resulting interaction energies for the potassium ion are also plotted and, for comparison, the results for the solvent molecules are displayed again. For most of the crystal faces, the interaction energies are in a range of -6000 kJ/mol to -2000 kJ/mol. The potassium ion shows interaction energies in the same range as the ammonium ion. When the potassium ion is placed on a dinitramide ion position, there are still strong interactions in the range of approximately -4200 kJ/mol to -1000 kJ/mol. The crystal faces (100) and (020) show interaction energies for the ions (ammonium, dinitramide and potassium) that are in the same range as the interaction energies of the solvent molecules.

Table 5-8: Number of lattice positions that are considered during computer simulation

face		# of AM positions	# of DN positions	total # of positions
(011)	1	-	2	2
(011)	2	4	-	4
(110)	1	-	2	2
(110)	2	4	-	4
(100)		2	2	4
(002)		3	3	6
(020)		1	1	2
(11-1)	1	-	4	4
(11-1)	2	4	-	4

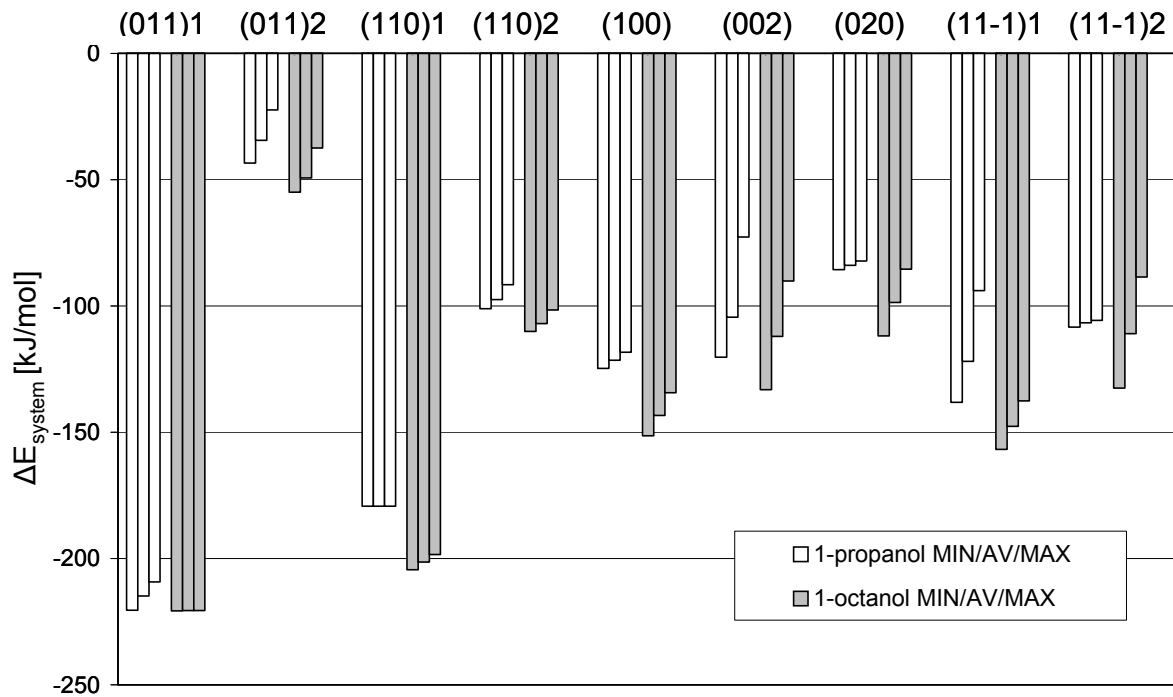


Figure 5-11: Interaction energies of the solvent molecules and the different crystal faces obtained from the minimized unit cell

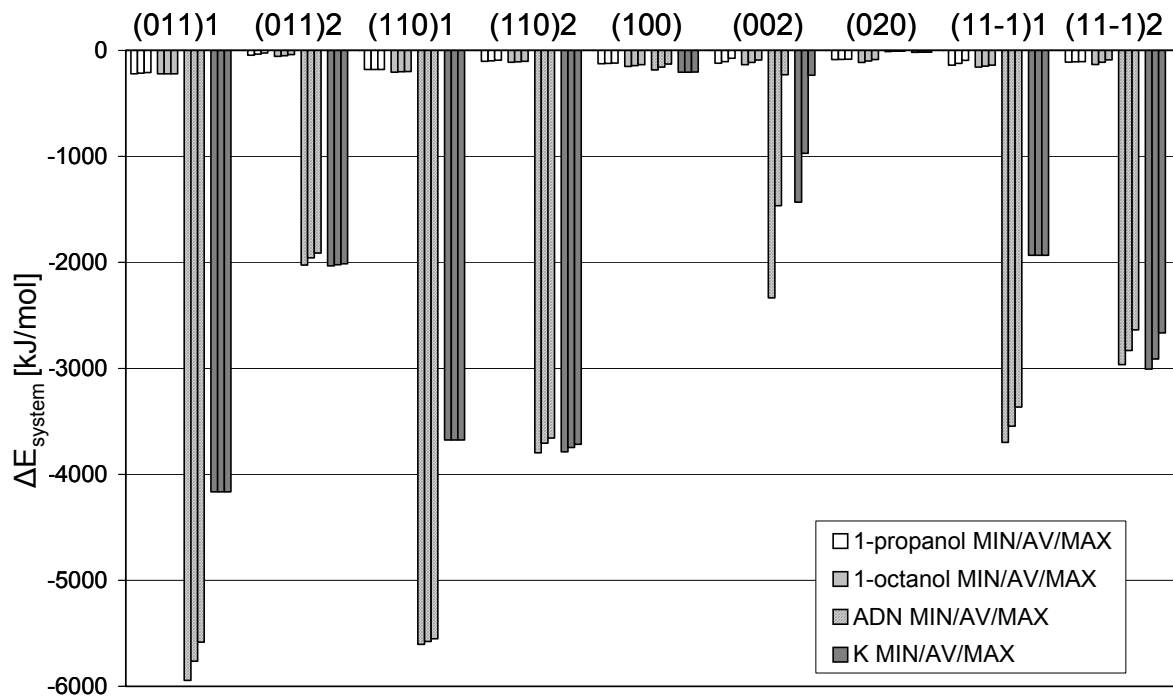


Figure 5-12: Interaction energies of the ions (ADN represented by ammonium ion and dinitramide ion, potassium ion) with the different crystal faces. Interaction energies for the solvent molecules are plotted for better comparison

5.1.4.2 Original unit cell

The interaction energies of the additives and the crystal faces were also calculated on the basis of the original unit cell (see Figure 5-4). No energy minimization of the crystal structure was done before cleaving the crystal faces. The atom positions obtained from

literature [GIL97] were kept fixed while calculating the interaction energies with the additives. The atomic charges obtained from the DFT-calculation were applied to the dinitramide ion. As additives, the solvent molecules, the ammonium and the dinitramide ion were taken into account for the calculation of the interaction energies. The crystal faces that were considered are reduced to the morphologically important ones. The results are compared to the interaction energies obtained from the minimized unit cell.

The results for the solvent molecules are shown in Figure 5-13 (1-propanol) and Figure 5-14 (1-octanol). The interaction energies for the solvent molecules and the crystal faces obtained from the minimized and the not minimized unit cell are in the same range for most crystal faces. For (011)1, the interaction energy of the unminimized structure relates as $\frac{1}{2}$ to $\frac{2}{3}$ compared to the minimized structure. The most significant difference in interaction energies is noticed for the face (011)2. The minimized structure shows a low interaction energy (approximately. -35 kJ/mol for 1-propanol and -50 kJ/mol for 1-octanol) compared to the original geometrical structure (approximately. -110 kJ/mol for 1-propanol and -160 kJ/mol for 1-octanol).

The interaction energies of the ammonium ion and dinitramide ion with the crystal faces are compared in Figure 5-15. For the (011)1, (011)2, (110)1 and (110)2 face, the relative difference of the interaction energies is in the same range as for the solvent molecules. For the (100) and the (002) faces, the maximum interaction energies for the original structure are positive. For the (020) face, all interaction energies (minimum, average, maximum) are positive.

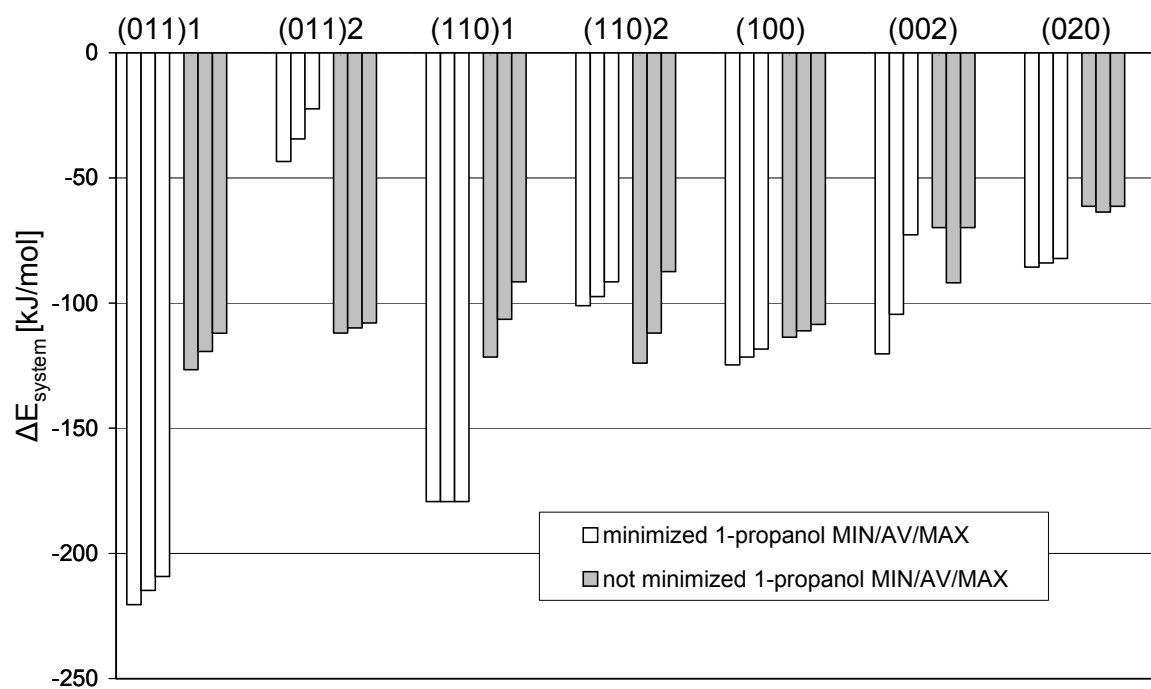


Figure 5-13: Original unit cell: Comparison of the interaction energies of the crystal faces and 1-propanol

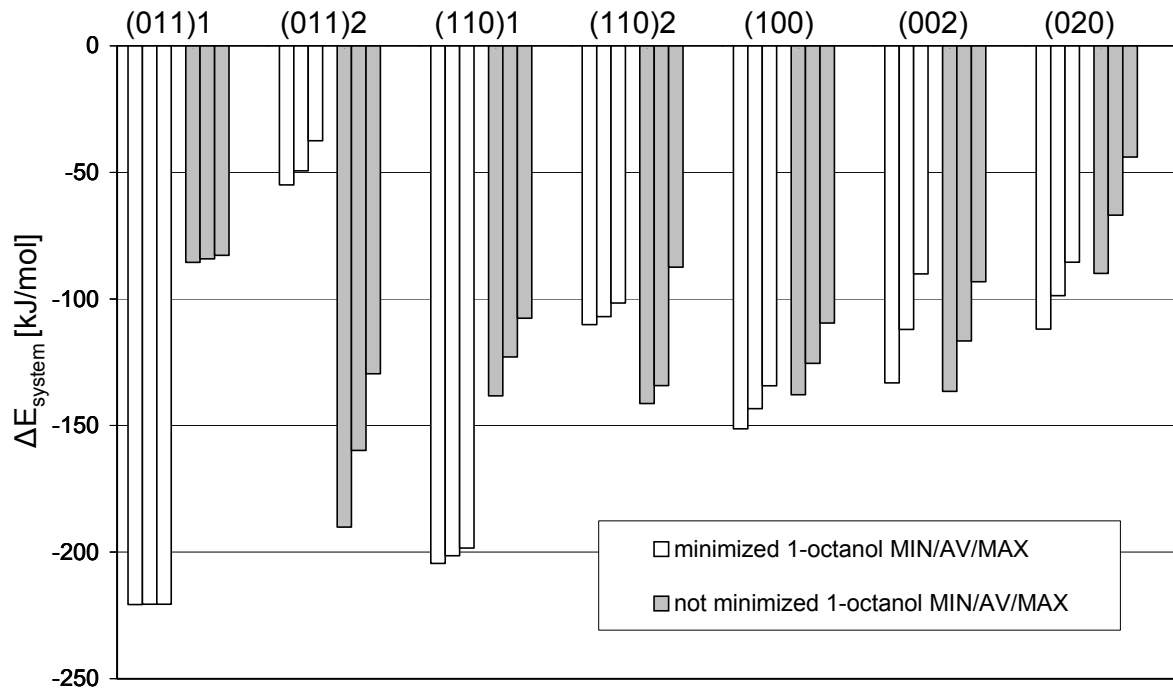


Figure 5-14: Original unit cell: Comparison of the interaction energies of the crystal faces and 1-octanol

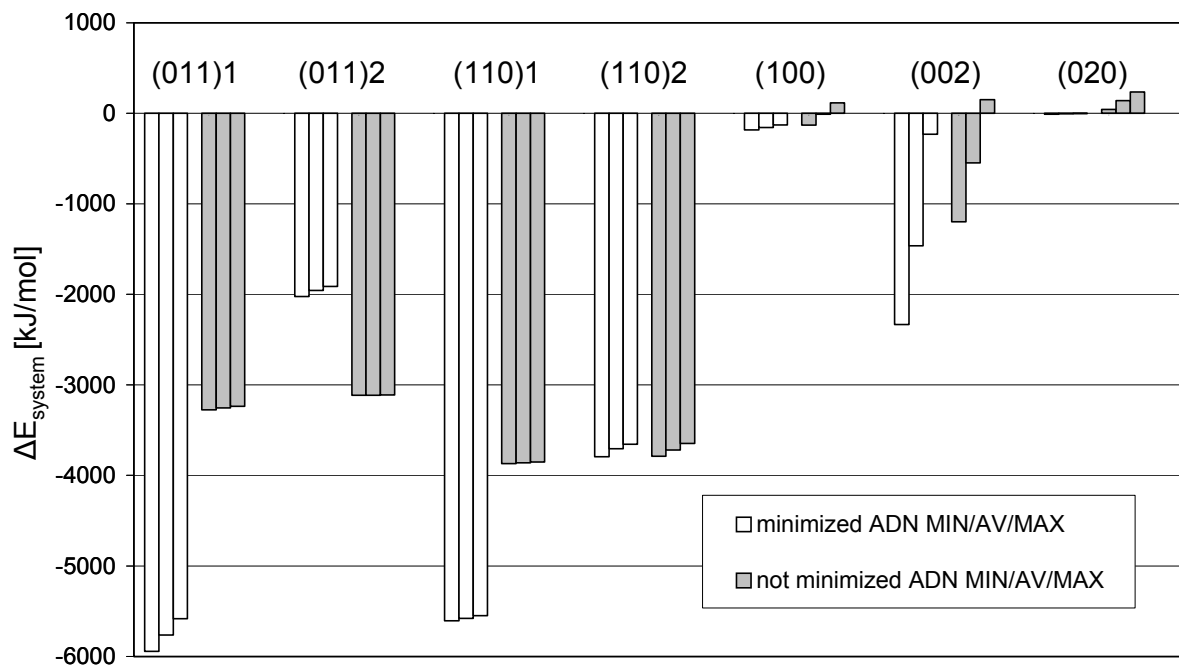


Figure 5-15: Original unit cell: Comparison of the interaction energies of the crystal faces and the ammonium respectively dinitramide ion

5.2 Experimental results

5.2.1 Electrolytic conductivity measurement: Characteristic curves

Electrolytic conductivity (EC) measurement is applied to monitor the crystallization process. This includes the verification of a complete dissolution of the solid ADN for T_{SAT} and the detection of the nucleation temperature T_{NUC} as well as the determination of the concentration in the solution and the supersaturation during the process.

The preliminary work in terms of EC measurement was the determination of the temperature and concentration dependence for ADN dissolved in 1-propanol and 1-octanol. Different solutions with defined concentrations are cooled down from 40 °C to 20 °C while EC is measured continuously (Figure 5-16 and 5-17).

EC is plotted against the concentration and is approximated by a second order polynomial. As a result characteristic curves (a family of curves with the temperature as variable) are obtained. Figure 5-18 and 5-19 show the characteristic curves in the range of 20 °C to 40 °C for temperature steps of 2.5°C. It is possible to plot the characteristic curve for any temperature. This is important for the evaluation of the EC data obtained from the crystallization processes.

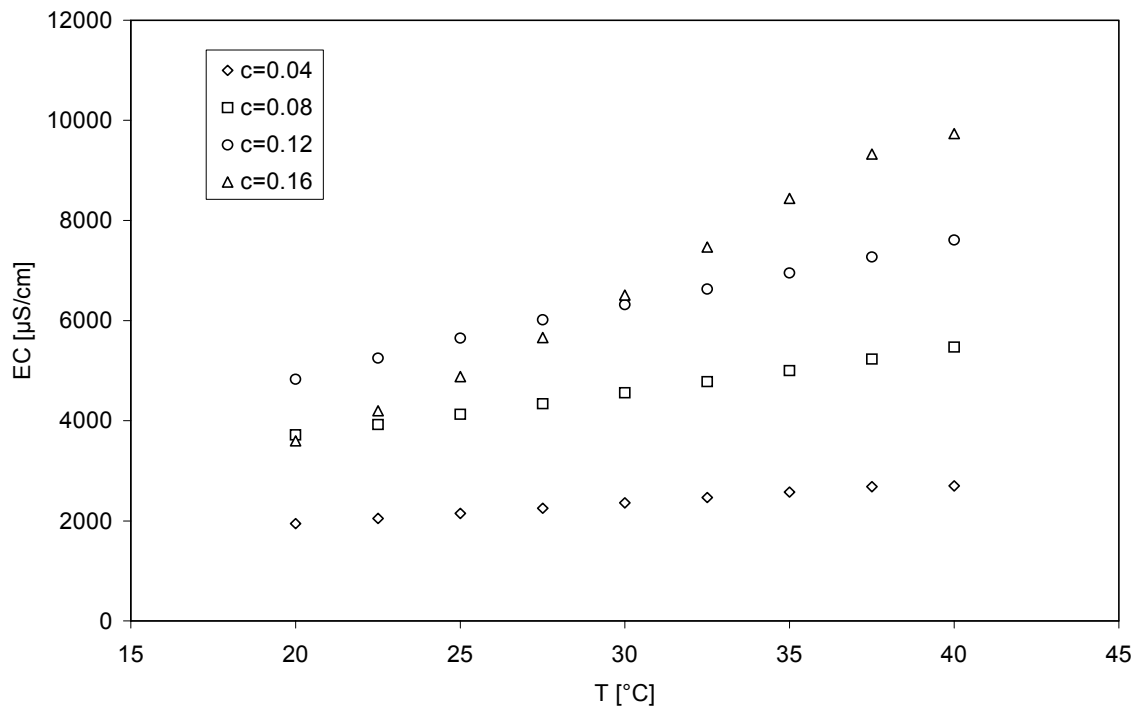


Figure 5-16: ADN in 1-propanol: temperature dependent EC for different constant concentrations c

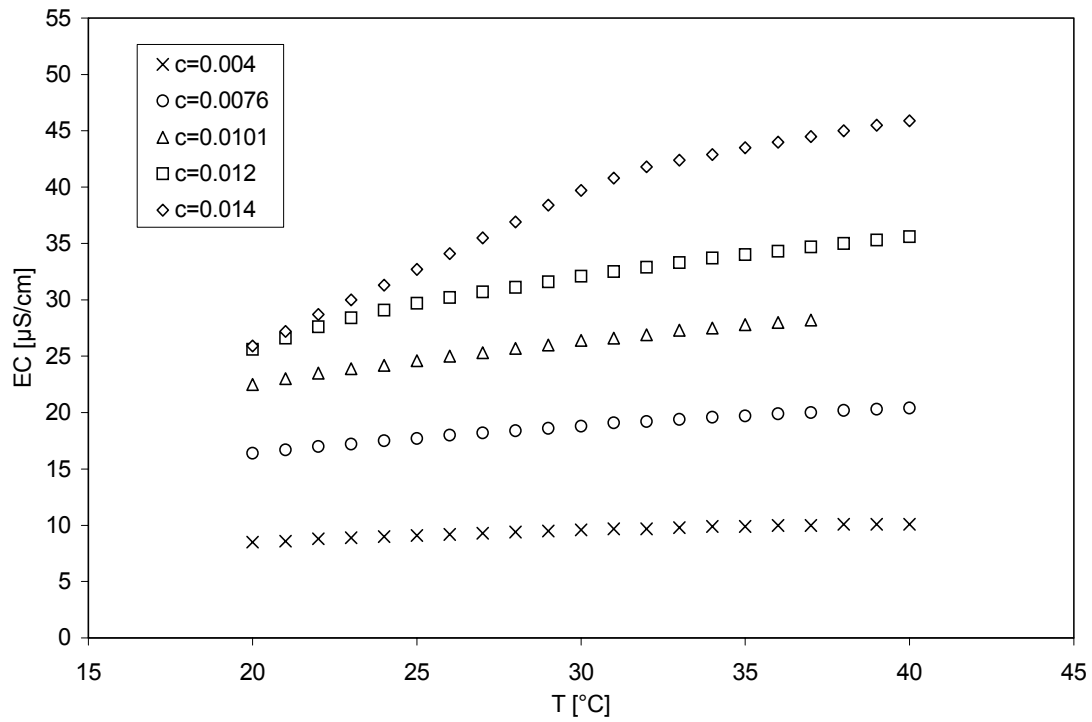


Figure 5-17: ADN in 1-octanol: temperature dependent EC for different constant concentrations c

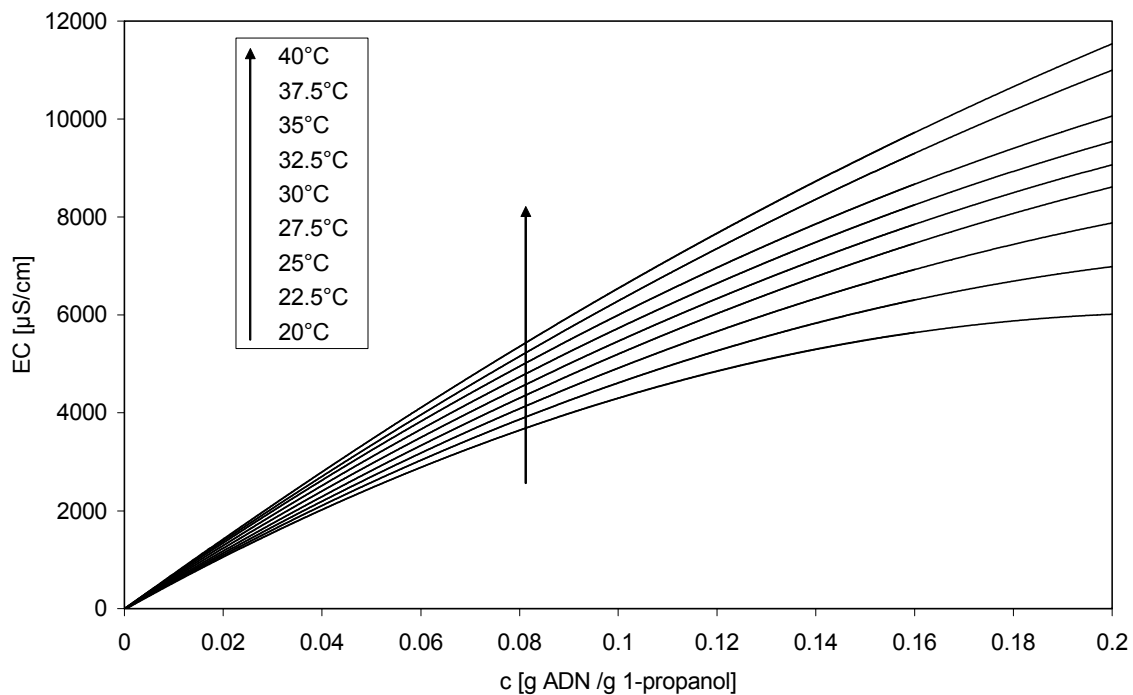


Figure 5-18: ADN in 1-propanol: characteristic curves for the temperature range 20 °C to 40 °C in steps of 2.5 °C

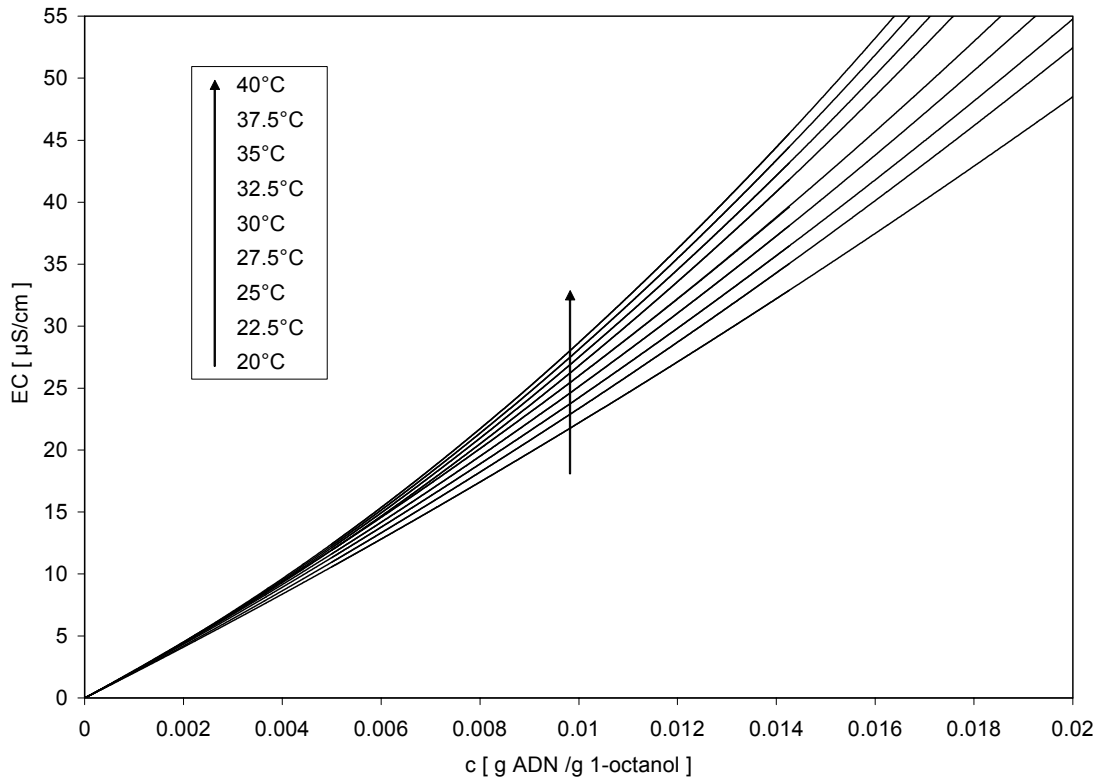


Figure 5-19: ADN in 1-octanol: characteristic curves for the temperature range 20 °C to 40 °C in steps of 2.5 °C

5.2.2 Solubility data

To obtain the solubility data for ADN in 1-propanol and 1-octanol, the ECs of saturated solutions are measured for different temperatures. The corresponding concentrations are extrapolated by using the previously determined characteristic curves. For both solvents, the saturation concentrations are also determined by the evaporation method. Figure 5-20 and 5-21 show the ECs and the solubility curves for the two solvents.

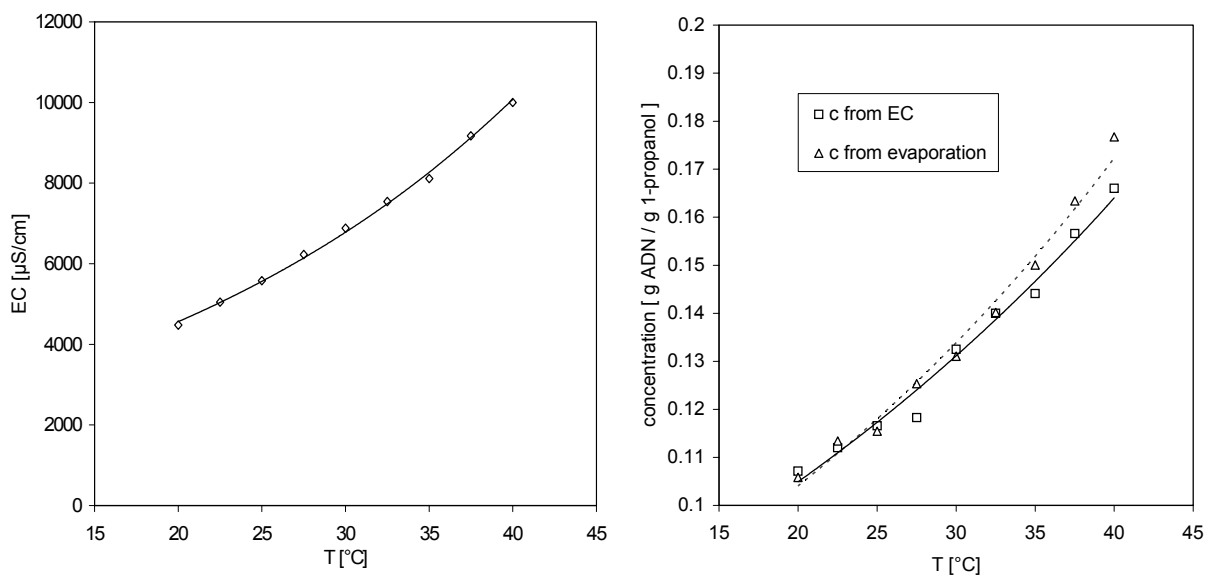


Figure 5-20: ADN/1-propanol: EC-T (left) and solubility curves (right) obtained from EC measurement and from evaporation experiment

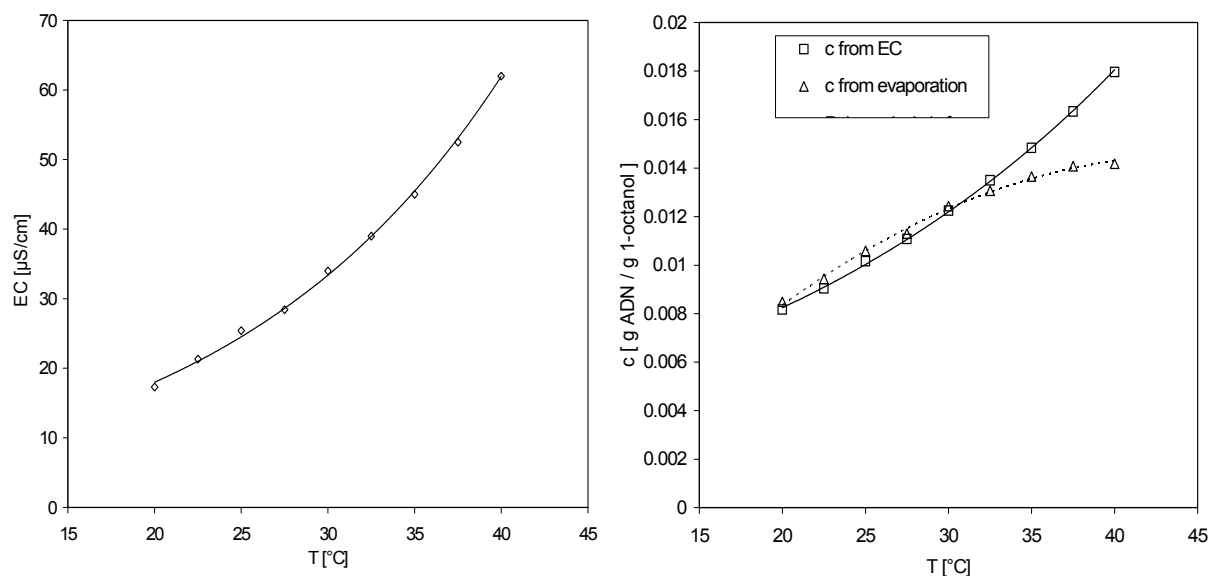


Figure 5-21: ADN/1-octanol: EC-T (left) and solubility curves (right) obtained from EC measurement and from evaporation experiment

5.2.3 Crystallization

The crystallization work was done in three steps:

First, a solvent screening was carried out to find appropriate solvents. This is described in detail by Fuhr et al. [FUH07_02]. For the selection of solvents, natural cooling experiments were done to get a first impression of the crystallization behaviour (Chapter 5.2.3.1). The crystal shape is visualized by light microscopy. The solvent content of the crystals was measured by HPLC.

Starting from the above-mentioned, selected alcohols were used as solvents (Chapter 5.2.3.2) in the second step of the crystallization work. These preliminary experiments were all carried out without EC measurement. The products were characterized by SEM and microscopy (crystal shape) as well as by DSC and TG analysis (thermal behaviour).

The third step was to go more into detail by carrying out small scale and large scale experiments with different cooling rates for the two solvents 1-propanol (Chapter 5.2.3.3) and 1-octanol (Chapter 5.2.3.4). In addition to the characterization methods used for the crystals obtained from the alcohol screening, particle detection with a Lasentec FBRM was applied (only for the large scale experiments).

5.2.3.1 Natural cooling

All natural cooling experiments were carried out without EC measurements. A saturated solution ($T_{\text{SAT}} = 40\text{ }^{\circ}\text{C}$) served as basis for all preliminary experiments. The crystallization behaviour of ADN by natural cooling was investigated for tetrahydrofuran (Figure 5-22), acetonitrile (Figure 5-23) and 1-propanol (Figure 5-24) as solvents. The resulting ADN crystals were investigated by microscopy and the solvent content was analyzed (Table 5-9).

Table 5-9: Natural cooling experiments

solvent	solvent content	crystal shape
tetrahydrofuran	0.34 %	needle-shaped
acetonitrile	0.09 %	twinned crystals
1-propanol	0.24 %	plate-shaped

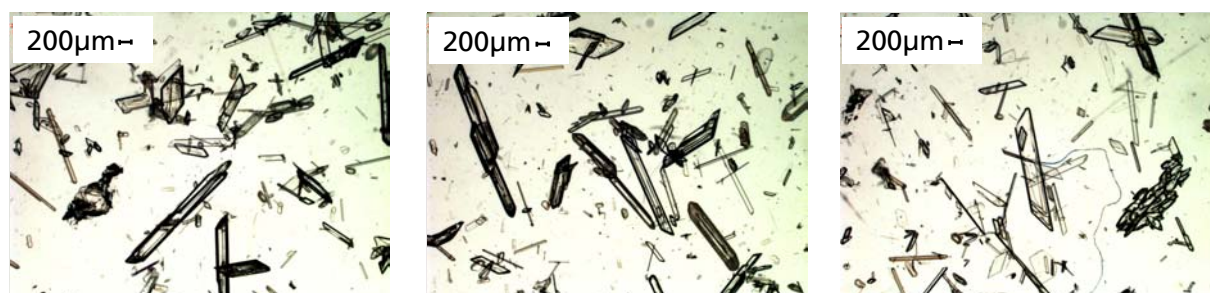


Figure 5-22: ADN from tetrahydrofuran, natural cooling

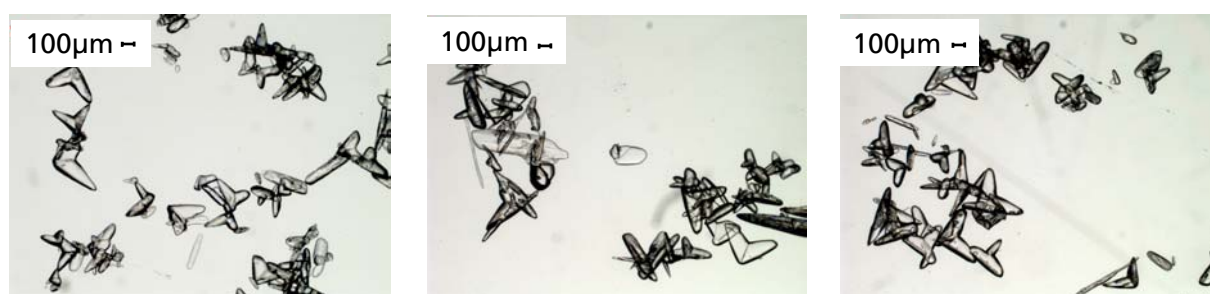


Figure 5-23: ADN from acetonitrile, natural cooling

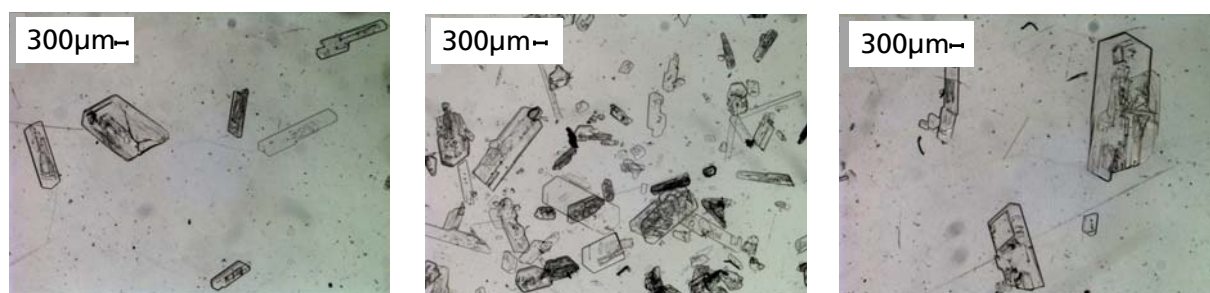


Figure 5-24: ADN from 1-propanol, natural cooling

5.2.3.2 Alcohol screening

From the natural cooling experiments, 1-propanol turned out to be the most promising solvent to obtain crystals with a low aspect ratio. Consequently, a preliminary screening was done for different alcohols to see if there is an influence of the solvent on the crystal shape and quality. Saturated solutions are cooled down from $T = 40\text{ °C}$ to $T = 20\text{ °C}$ with a linear cooling rate of 10 K/h . The suspension was homogenized by using a paddle stirrer.

The quality of the recrystallized ADN was examined by SEM as well as by DSC and TG analysis. From the DSC analysis, the thermal behaviour from 20 °C to 110 °C is plotted as this is the temperature range where melting occurs.

The experiments resulted in plate-shaped crystals for 1-propanol. The surface is smooth with small, secondary crystals on it (Figure 5-25). The DSC (Figure 5-29, left) shows a sharp melting peak at $T_{\text{ONSET}} = 93.47$ °C, the melting enthalpy is $H_{\text{MELT}} = 145.8$ J/g. A mass loss of 0.44 % for $T < 100$ °C is detected and a total mass loss of 98.43 % is measured by TG analysis when $T = 205$ °C is reached (Figure 5-29, right).

By using 2-propanol as solvent, a sharp melting peak is observed at $T_{\text{ONSET}} = 91.90$ °C, ($H_{\text{MELT}} = 112.4$ J/g) in the DSC analysis (Figure 5-30). Additionally, a small endothermic peak at $T_{\text{ONSET}} = 58.08$ °C ($H_{\text{PEAK}} = 2.80$ J/g) is present. A mass loss of 1.44 % occurs below $T = 100$ °C (TG analysis, Figure 5-30). The total mass loss is 99.03 % for $T = 205$ °C. The crystals are flat, plate-shaped similar to those obtained from 1-propanol (Figure 5-26).

The ADN crystals from the solvent 1-pentanol are flat and plate-shaped but more compact than those obtained from 1-propanol and 2-propanol. The surface of ADN from 1-propanol is slightly fissured (Figure 5-27). The DSC (Figure 5-31, left) shows a small, broad peak ($T_{\text{ONSET}} = 71.64$ °C, $H_{\text{MELT}} = 26.76$ J/g) about 20 °C below the expected melting temperature. A mass loss of 5.22 % is detected by TG analysis (Figure 5-31, right) for $T < 100$ °C, the total mass loss is 97.86 % ($T = 205$ °C).

The crystals obtained from 1-octanol are of a flat shape. The basis area has a length-width-ratio of approximately 1.5. The surface of the crystals is very smooth (Figure 5-28). DSC and TG analysis results are plotted in Figure 5-32. DSC analysis shows a sharp melting peak ($T_{\text{ONSET}} = 93.43$ °C, $H_{\text{MELT}} = 145.2$ J/g). A mass loss of 1.87 % for $T < 100$ °C is resulting from the TG analysis, the total mass loss is 96.42 % ($T = 205$ °C). The solvents used in the following experiments are limited to 1-propanol (Chapter 5.2.3.3) and 1-octanol (Chapter 5.2.3.4).

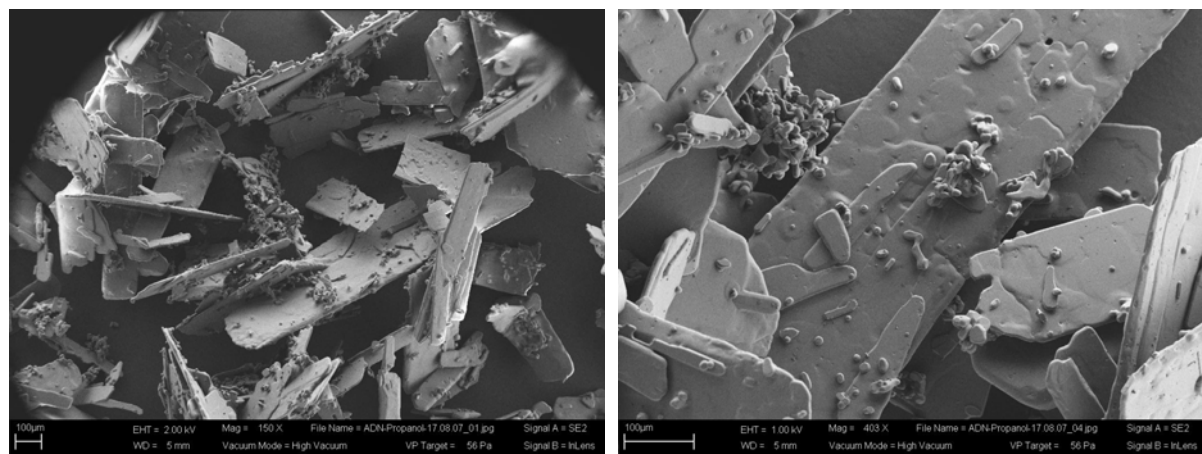


Figure 5-25: ADN from 1-propanol, SEM

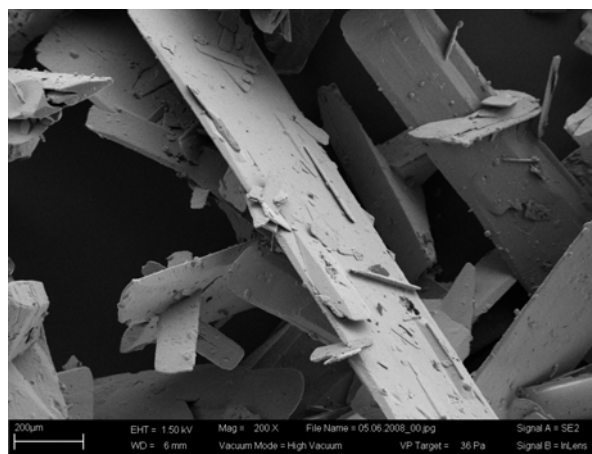
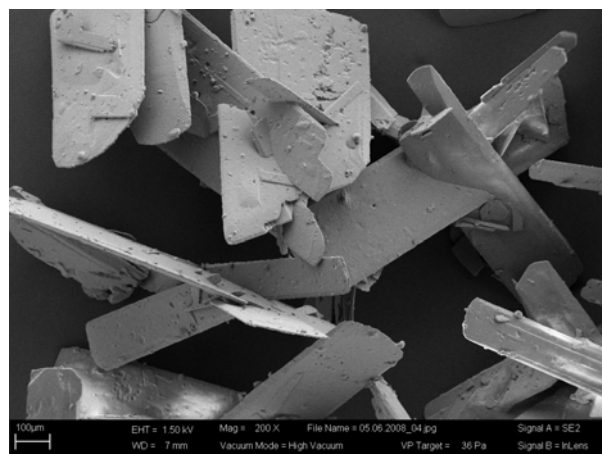


Figure 5-26: ADN from 2-propanol, SEM

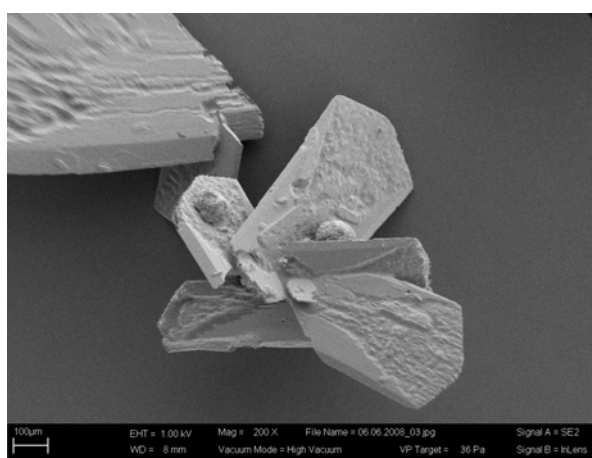
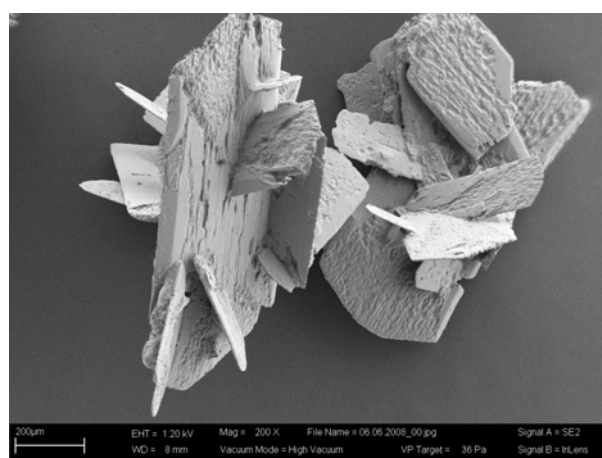


Figure 5-27: ADN from 1-pentanol, SEM

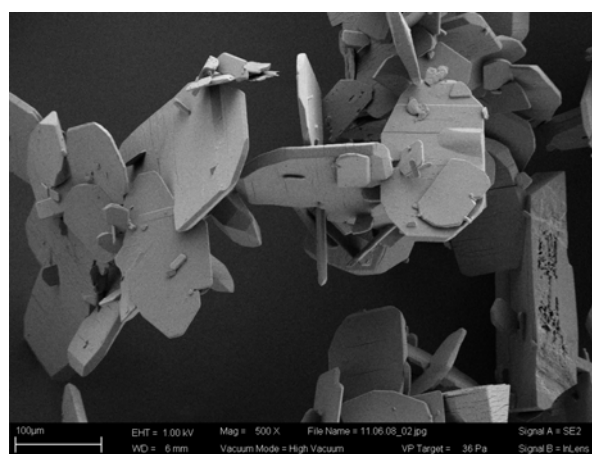
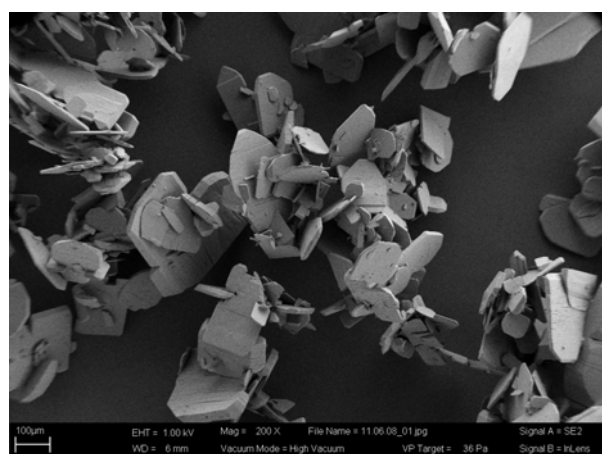


Figure 5-28: ADN from 1-octanol, SEM

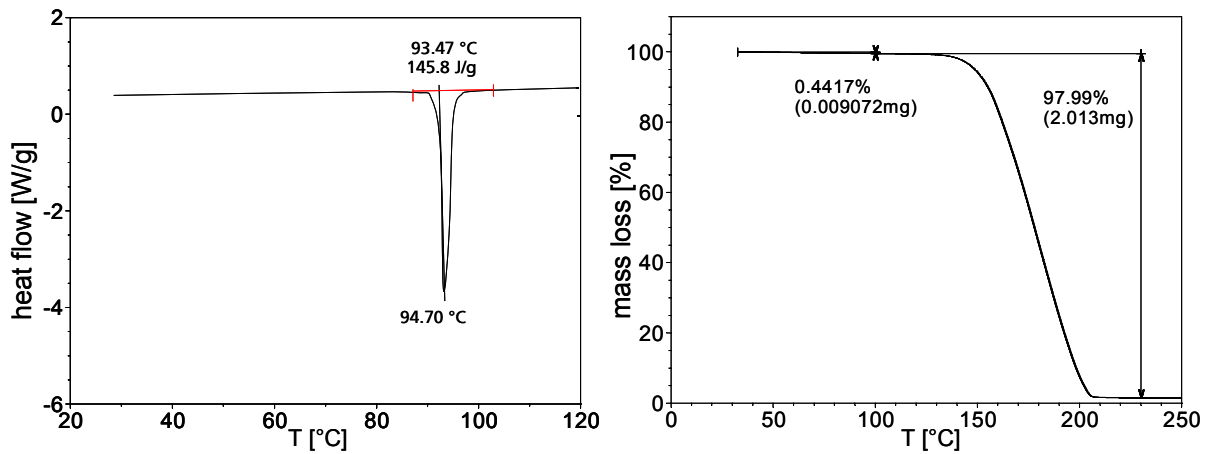


Figure 5-29: ADN from 1-propanol: DSC (left), TGA (right)

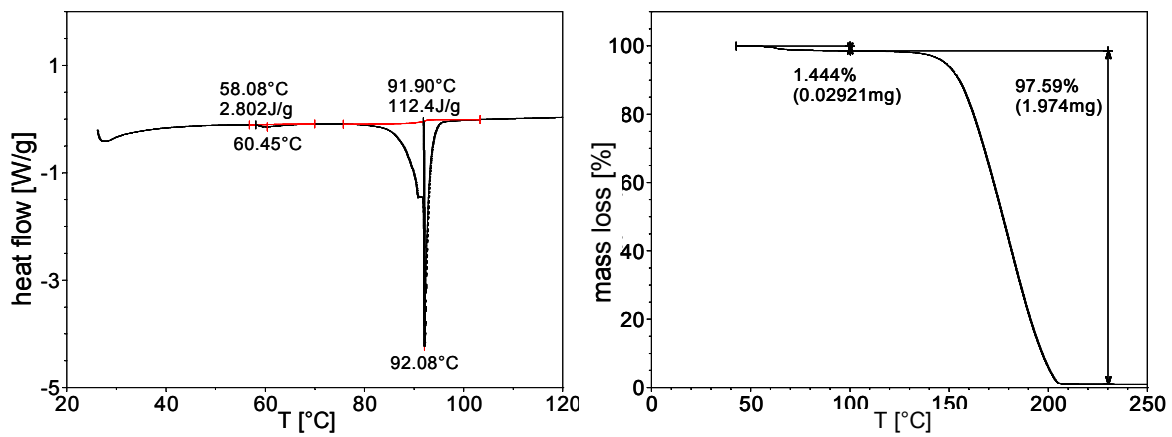


Figure 5-30: ADN from 2-propanol: DSC (left), TGA (right)

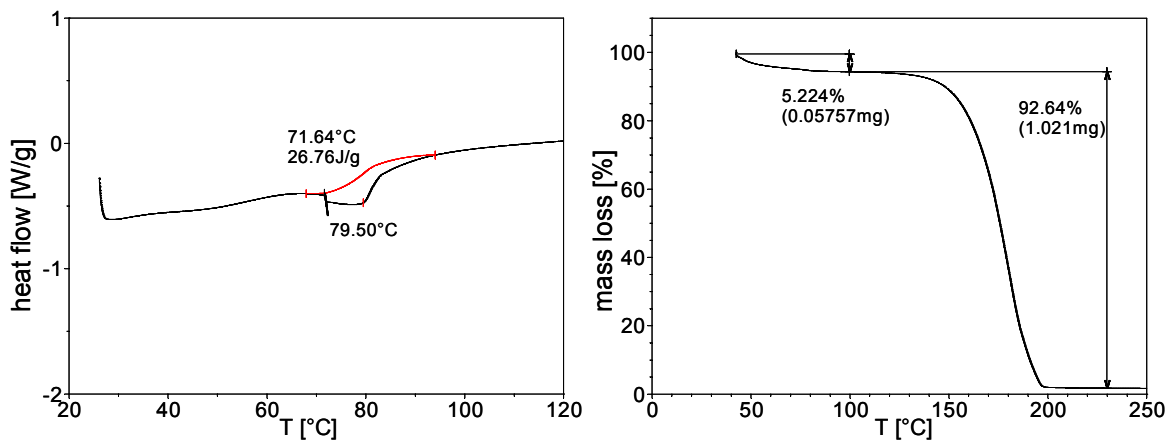


Figure 5-31: ADN from 1-pentanol: DSC (left), TGA (right), x-axis in T [°C]

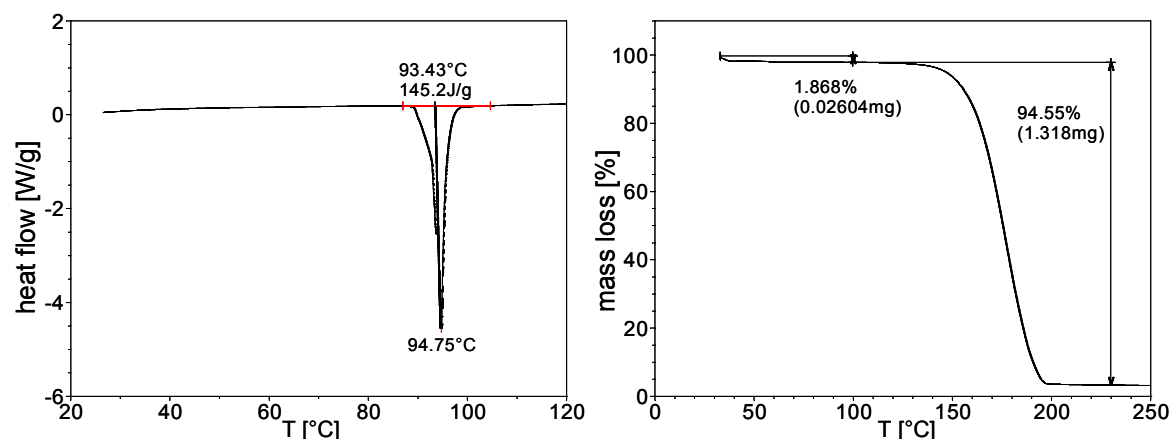


Figure 5-32: ADN from 1-octanol: DSC (left), TGA (right), x-axis in T [°C]

5.2.3.3 1-propanol

This chapter focuses on the use of 1-propanol as solvent for ADN crystallization. The experimental setup and the crystallization procedure are described in Chapter 4.1.5.1 and Chapter 4.1.5.2. An overview on these crystallization experiments and the analysis is given in Table 5-10 and 5-11.

Table 5-10: 1-propanol: Overview on experiments

experiment	solvent	concentration c (g/g)	cooling rate	set up
P-5-s	1-propanol	0.1760	5 K/h	small
P-5-L	1-propanol	0.1763	5 K/h	large
P-10-s	1-propanol	0.1760	10 K/h	small
P-10-L	1-propanol	0.1761	10 K/h	large

Table 5-11: 1-propanol: Overview on analytics

experiment	SEM and microscopy	thermal analysis (DSC and TGA)	S(t)	Lasentec; EC(t)
P-5-s	Figure 5-33	Figure 5-37	Figure 5-43	—
P-5-L	Figure 5-34	Figure 5-38	Figure 5-43	Figure 5-41
P-10-s	Figure 5-35	Figure 5-39	Figure 5-44	—
P-10-L	Figure 5-36	Figure 5-40	Figure 5-44	Figure 5-42

Morphology

The crystals from the experiments with 1-propanol are all of the same basic morphology: They are flat, needle shaped particles with similar length-width-ratios.

The ADN particles from P-5-s (Figure 5-33) and P-10-s (Figure 5-35) have smooth surfaces with only some few secondary crystals on them. P-10-L (Figure 5-36) also provides a smooth surface but with a larger amount of fine secondary crystals. The surfaces of P-5-L (Figure 5-34) are not as smooth as the surfaces from the other experiments. Craters and scratches are visible on the crystals.



Figure 5-33: P-5-s: SEM and microscopy

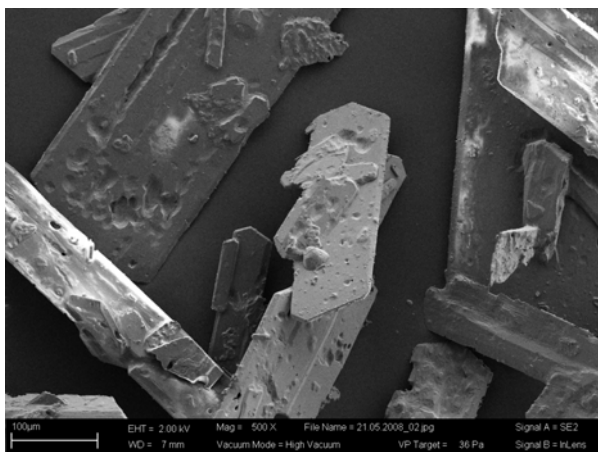
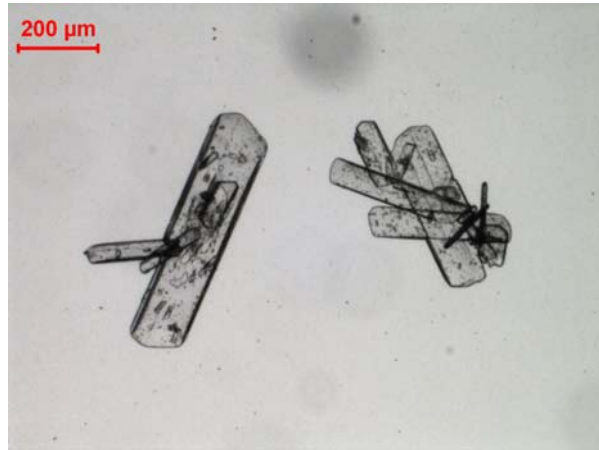


Figure 5-34: P-5-L: SEM and microscopy

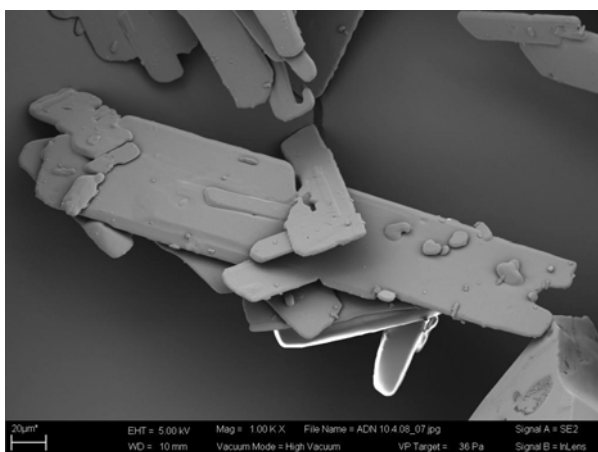
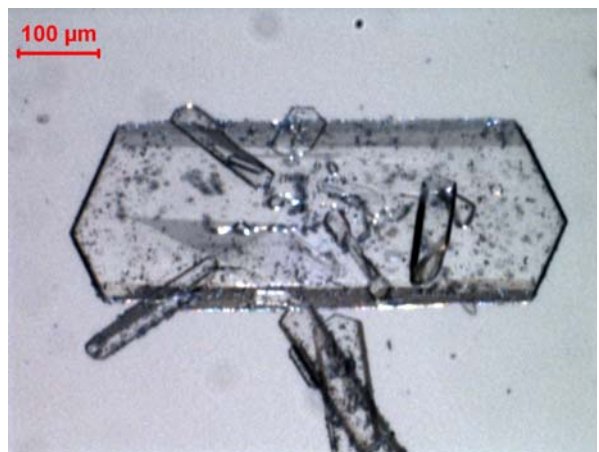
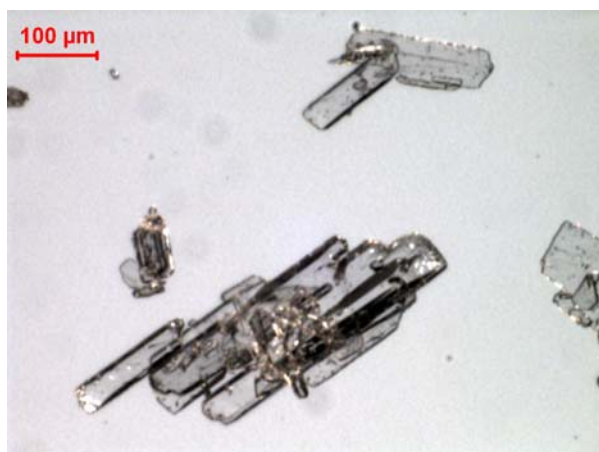


Figure 5-35: P-10-s: SEM and microscopy



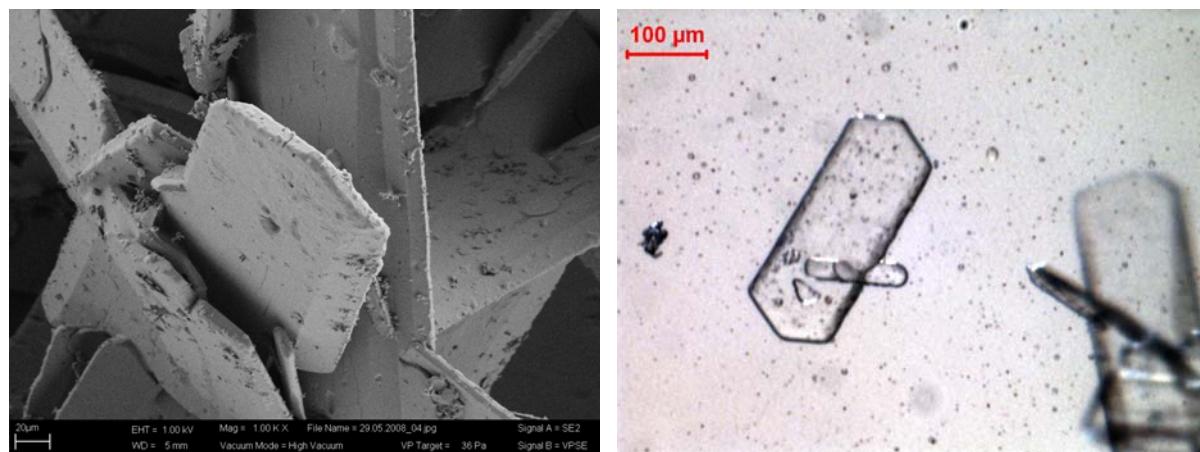


Figure 5-36: P-10-L: SEM and microscopy

Thermal analysis

The DSC analysis of the samples P-5-s (Figure 5-37), P-10-s (Figure 5-39) and P-10-L (Figure 5-40) show a sharp melting peak with melting temperatures $T_{\text{ONSET, P-5-s}} = 91.98\text{ }^{\circ}\text{C}$, $T_{\text{ONSET, P-10-s}} = 93.72\text{ }^{\circ}\text{C}$ and $T_{\text{ONSET, P-5-L}} = 93.53\text{ }^{\circ}\text{C}$. The corresponding phase transition enthalpies are $H_{\text{MELT, P-5-s}} = 136.1\text{ J/g}$, $H_{\text{MELT, P-10-s}} = 153.6\text{ J/g}$ and $H_{\text{MELT, P-10-L}} = 153.1\text{ J/g}$. For P-5-s, an additional, small endothermic peak is observed at $T_{\text{ONSET}} = 59.44\text{ }^{\circ}\text{C}$ ($H_{\text{PEAK}} = 6.147\text{ J/g}$). P-5-L (Figure 5-38) exhibits a broad endothermic peak at $T_{\text{ONSET}} = 71.70\text{ }^{\circ}\text{C}$ ($H_{\text{PEAK}} = 38.49\text{ J/g}$) but not a sharp melting peak like the other samples.

The TG analysis for P-5-s (Figure 5-37) and P-5-L (Figure 5-38) show first-step mass losses of 0.75 % and 7.17 % for $T < 100\text{ }^{\circ}\text{C}$. The total mass losses of the samples are 98.75 % and 98.20 % when $T = 205\text{ }^{\circ}\text{C}$ is reached. For P-10-s (Figure 5-39), a two-step mass loss occurs for temperatures $T < 100\text{ }^{\circ}\text{C}$: the first step is a mass loss of 2.80 % ($T = 67\text{ }^{\circ}\text{C}$), the second step a mass loss of 2.44 % ($T = 100\text{ }^{\circ}\text{C}$) so the total mass loss for $T < 100\text{ }^{\circ}\text{C}$ is 5.24 %. The total mass loss is 98.22 % at $T = 210\text{ }^{\circ}\text{C}$. P-10-L (Figure 5-40) shows a mass loss of 0.34% for $T < 100\text{ }^{\circ}\text{C}$; the total mass loss is 97.64 % at $T = 197\text{ }^{\circ}\text{C}$.

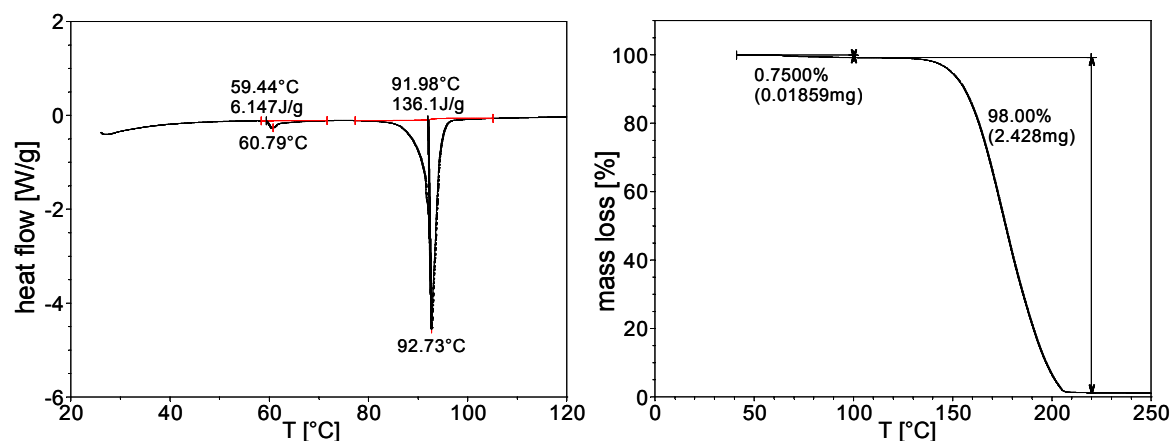


Figure 5-37: P-5-s: Thermal analysis: left: DSC, right: TGA, x-axis in T [°C]

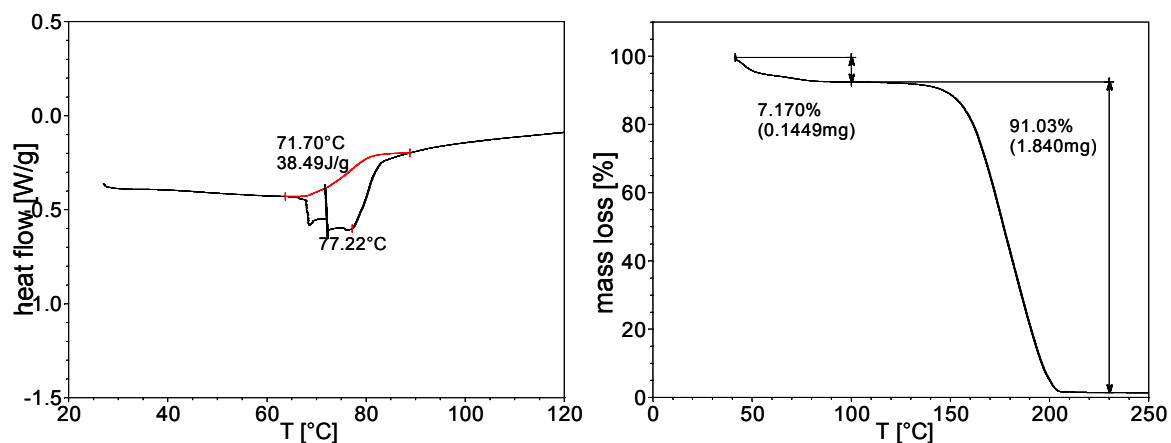


Figure 5-38: P-5-L: Thermal analysis: left: DSC, right: TGA, x-axis in T [°C]

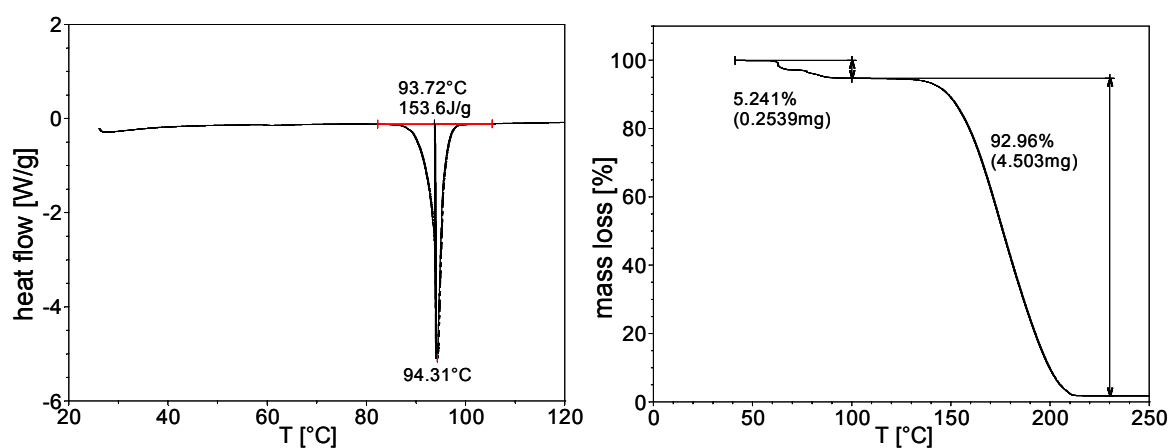


Figure 5-39: P-10-s: Thermal analysis: left: DSC, right: TGA, x-axis in T [°C]

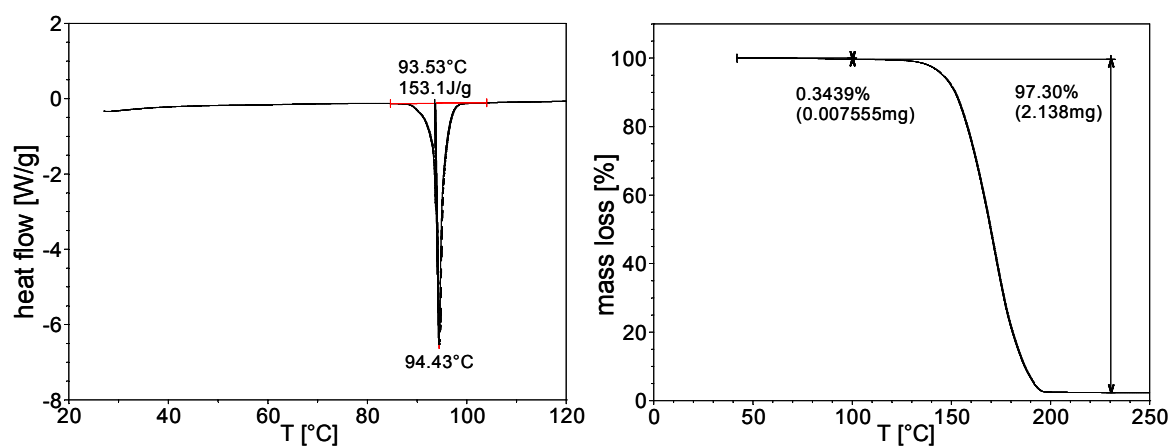


Figure 5-40: P-10-L: Thermal analysis: left: DSC, right: TGA, x-axis in T [°C]

Process monitoring

Chord length measurement using a Lasentec FBRM were applied for the large scale experiments P-5-L and P-10-L. The development of the number of detected chord lengths between 1 μm and 10 μm is displayed together with the electrolytic conductivity and the temperature during the process.

Figure 5-41 shows the results for P-5-L. The cooling process is beginning at $t = 11:55$. The value for EC at $T = 40\text{ }^\circ\text{C}$ is $EC_{P-5-L, 40\text{ }^\circ\text{C}} = 10290\text{ }\mu\text{S/cm}$. The chord lengths number starts to increase at $t = 12:10$ (corresponding temperature $T = 38.6\text{ }^\circ\text{C}$). From this time on, peaks of the electrolytic conductivity are formed: EC is increasing due to the settlement of the solid ADN. The number of chord lengths counted per second is increasing rapidly at $t = 14:30$ (corresponding temperature $T = 27.7\text{ }^\circ\text{C}$) from approximately 200 counts per second to approximately 1000 counts per second. After reaching the end temperature $T = 20\text{ }^\circ\text{C}$, the values for EC keeps constant ($EC_{P-5-L, 20\text{ }^\circ\text{C}} = 4060\text{ }\mu\text{S/cm}$, $EC_{P-5-L, 20\text{ }^\circ\text{C}, \text{PEAK}} = 4610\text{ }\mu\text{S/cm}$).

The results for P-10-L are plotted in Figure 5-42. At $t = 09:55$, the cooling started. The electrolytic conductivity is $EC_{P-10-L, 40\text{ }^\circ\text{C}} = 10260\text{ }\mu\text{S/cm}$. At the same time, the formation of particles is detected by the Lasentec measurement; a first maximum of counts per second is reached at $t = 10:13$ ($T = 36.6\text{ }^\circ\text{C}$). At $t = 11:30$ ($T = 24.6\text{ }^\circ\text{C}$) the number of counts per second is increasing from approximately 400 counts/s to approximately 1300 counts/s. After the cooling phase is finished, the electrolytic conductivity keeps constant at $EC_{P-10-L, 20\text{ }^\circ\text{C}} = 4120\text{ }\mu\text{S/cm}$ respectively $EC_{P-10-L, 20\text{ }^\circ\text{C}, \text{PEAK}} = 4710\text{ }\mu\text{S/cm}$.

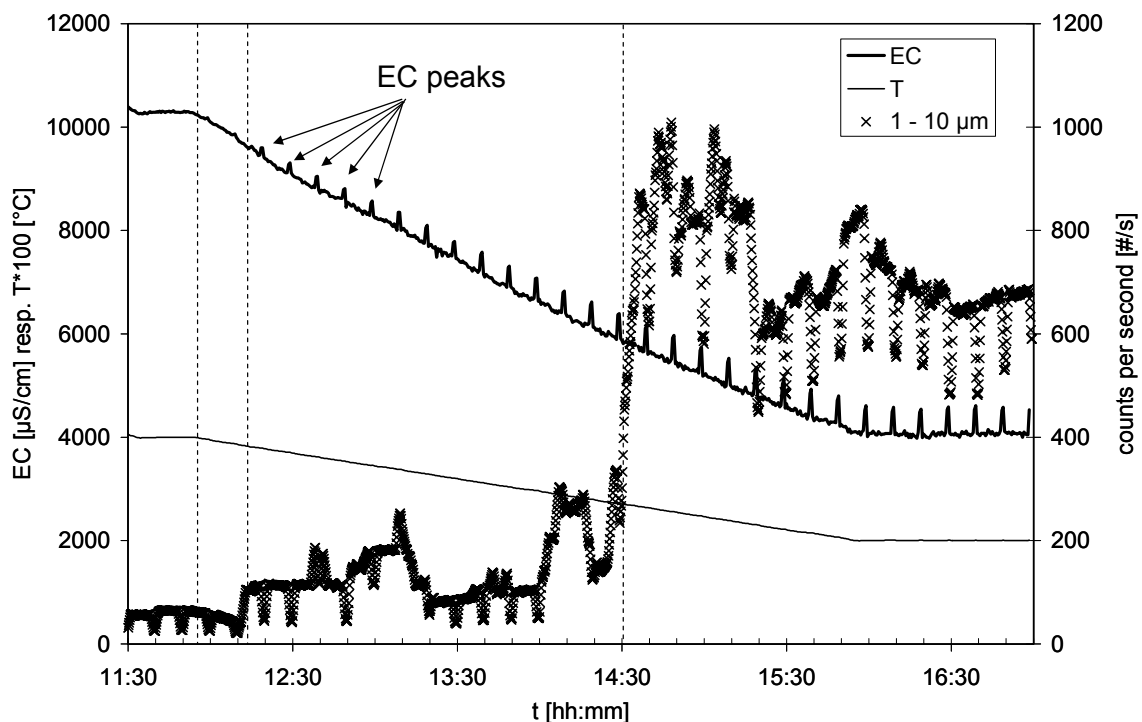


Figure 5-41: P-5-L: Lasentec and EC measurement

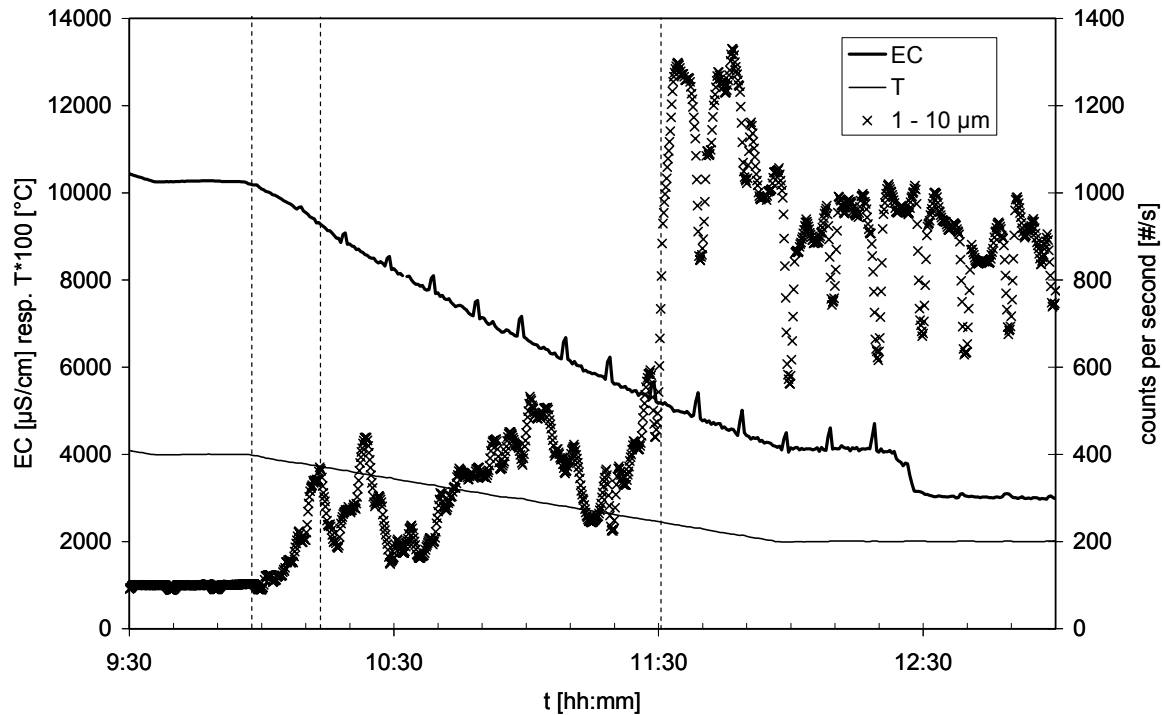


Figure 5-42: P-10-L: Lasentec measurement

Supersaturation

The EC measurement (peak values) was evaluated by using the characteristic curves (Figure 5-18). The actual concentration during the process was determined in this way. By comparing the actual concentration with the concentration of the saturated solution at the same temperature (see also Chapter 11, Figure 11-9 and 11-10) the supersaturation S was determined for the four crystallization experiments from 1-propanol.

The development of S is plotted against process time for four experiments. At the beginning of each crystallization process, the supersaturation is $S = 1$.

For P-5-s (Figure 5-43, left), supersaturation is slowly increasing from the beginning of the cooling rate. The maximum value $S = 1.04$ is reached at $t = 01:42$ ($T = 31.2$ °C). Within approximately 1 h ($t = 02:42$ to $02:52$), a reduction of the supersaturation back to $S = 1$ is taking place. S is then more or less constant for the remaining process time.

The supersaturation of the process P-5-L (Figure 5-43, right) is jumping from $S = 1.01$ to $S = 1.05$ in the time frame $t = 34 - 44$ min ($T = 37.1 - 36.2$ °C). The maximum supersaturation $S = 1.07$ is reached at $t = 01:42$ ($T = 32.9$ °C). S is on a constant level until $t = 02:54$ ($T = 25.6$ °C). Then, it is instantly reduced to $S = 1$.

The supersaturation of the small-scale experiment with a cooling rate of 10 K/h (P-10-s) is plotted in Figure 5-44 (left). S is increasing within the time frame $t = 20 - 30$ min ($T = 36.8 - 35.1$ °C) to $S = 1.07$. After the cooling is finished, S is decreasing from $S = 1.03$ ($t = 01:50$, $T = 22.0$ °C) to $S = 1.01$ ($t = 02:10$, $T = 20.0$ °C).

The results of the large scale experiment with a cooling rate of 10 K/h (P-10-L) are displayed in Figure 5-44 (right). An increase of the supersaturation from $S = 1$ to $S = 1.05$ takes place at $t = 00:12 - 00:22$ ($T = 38.0 - 36.3$ °C). S is on a constant level for the duration of 1 hour until $t = 01:22$ ($T = 26.5$ °C) and is reduced to the initial value after the cooling is finished.

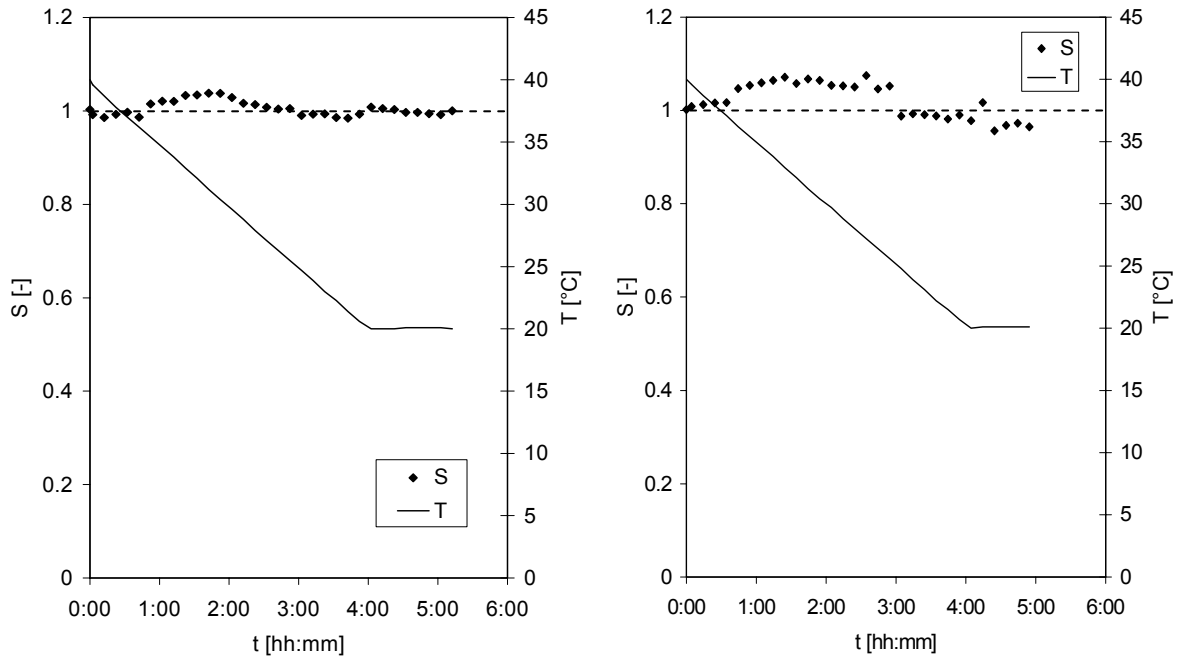


Figure 5-43: Supersaturation S during the crystallization process for P-5-s (left) and P-5-L (right)

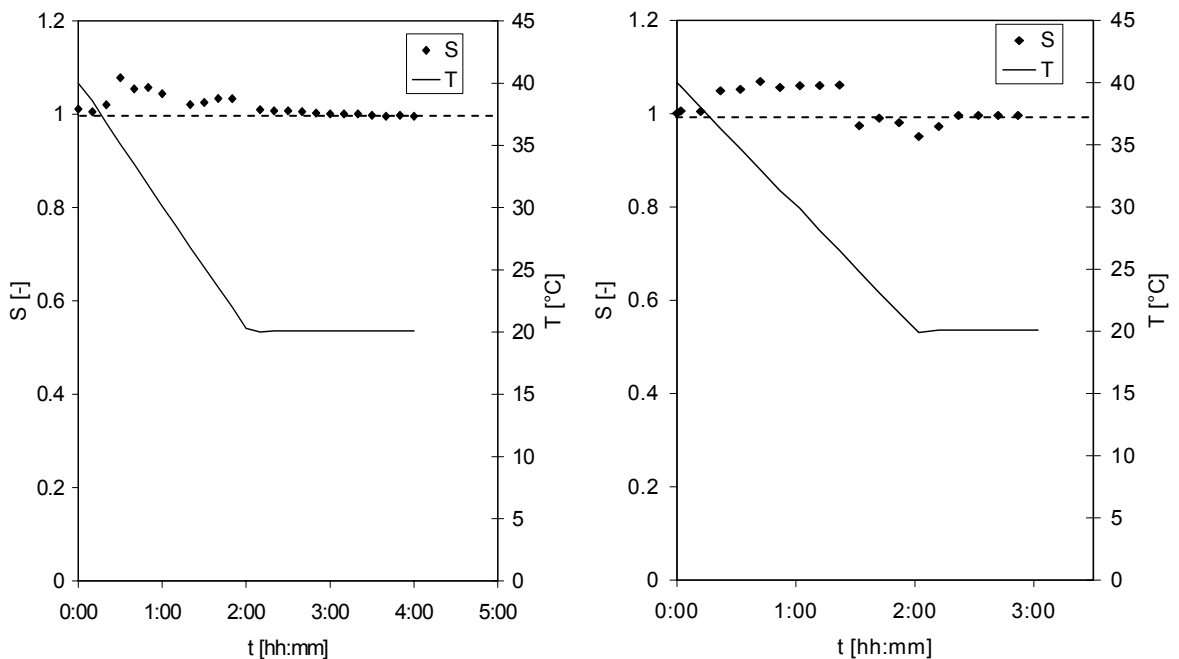


Figure 5-44: Supersaturation S during the crystallization process for P-10-s (left) and P-10-L (right)

5.2.3.4 1-octanol

The second solvent that was used for detailed crystallization experiments is 1-octanol. In Table 5-12 the experiments that were carried out are listed. Table 5-13 gives an overview on the analytics.

Table 5-12: 1-octanol: Overview on experiments

experiment	solvent	concentration c (g/g)	cooling rate	set up
O-5-s	1-octanol	0.0180	5 K/h	small
O-5-L-#1	1-octanol	0.0180	5 K/h	large
O-5-L-#2	1-octanol	0.0179	5 K/h	large
O-10-s	1-octanol	0.0180	10 K/h	small
O-10-L-#1	1-octanol	0.0180	10 K/h	large
O-10-L-#2	1-octanol	0.0180	10 K/h	large
O-10-L-#3	1-octanol	0.0180	10 K/h	large

Table 5-13: 1-octanol: Overview on analytics

experiment	SEM and microscopy	thermal analysis (DSC and TGA)	S(t)	Lasentec; EC(t)
O-5-s	Figure 5-45	Figure 5-52	Figure 5-62	—
O-5-L-#1	Figure 5-46	Figure 5-53	Figure 5-62	—
O-5-L-#2	Figure 5-47	Figure 5-54	Figure 5-62	Figure 5-60
O-10-s	Figure 5-48	Figure 5-55	Figure 5-63	—
O-10-L-#1	Figure 5-49	Figure 5-56	Figure 5-63	—
O-10-L-#2	Figure 5-50	Figure 5-57	Figure 5-63	Figure 5-61
O-10-L-#3	Figure 5-51	Figure 5-58	Figure 5-63	—

Morphology

The crystal shape of ADN from 1-octanol from the different crystallization experiments is described below.

ADN crystals received from the experiments with a cooling rate of 5 K/h (O-5-s: Figure 5-45; O-5-L-#1: Figure 5-46; O-5-L-#2: Figure 5-47) and ADN crystals from experiment O-10-s (Figure 5-48) are all of a plate-shaped morphology. They all have a basis area with a length – width – ratio of approximately 1:1.5.

The basis area of the particles obtained from O-5-s and O-10-s can be described as a rectangle with slightly truncated edges. Their surface is smooth with only a few scratches on them.

The basis areas of O-5-L-#1 and O-5-L-#2 can also be inscribed into a rectangle but their edges are truncated to a much larger extent than those of O-5-s and O-10-L. The surfaces of some of the crystals obtained from O-5-L-#1 and O-5-L-#2 are slightly fissured.

By crystallizing in the large vessel with a cooling rate of 10 K/h two different morphologies are emerging simultaneously. The ADN crystals are visualized in Figure 5-49 (O-10-L-#1), Figure 5-50 (O-10-L-#2) and Figure 5-51 (O-10-L-#1). One fraction of the product consists of rod-shaped particles with partly very fissured surfaces (O-10-L-#2). The second fraction is built of flat to compact shaped particles smaller than the rod-shaped ones.

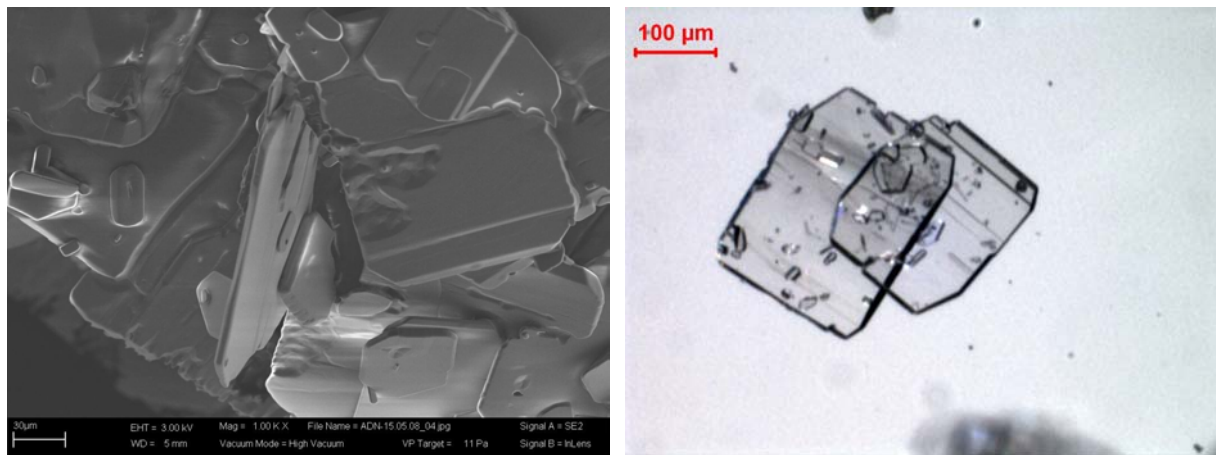


Figure 5-45: O-5-s: SEM and microscopy

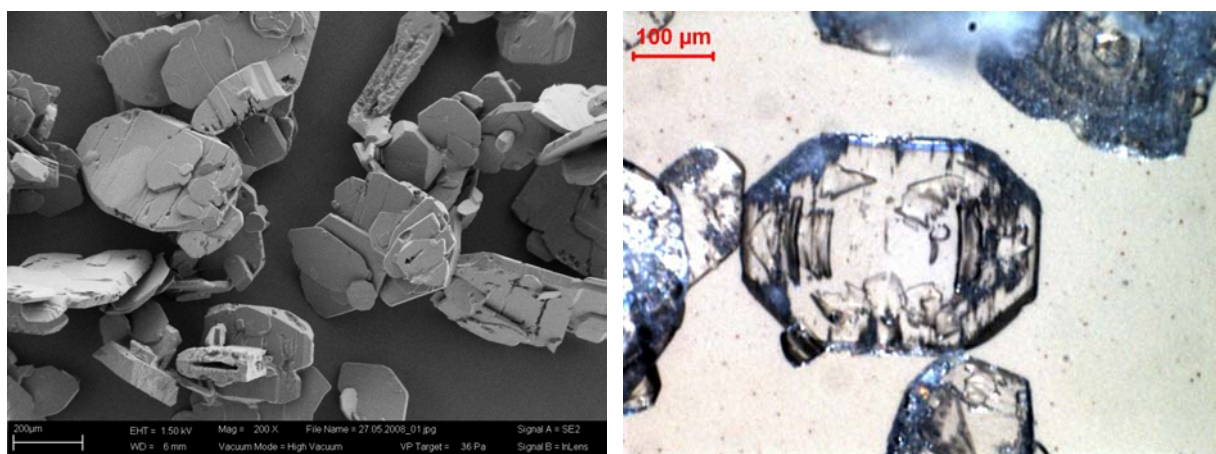


Figure 5-46: O-5-L-#1: SEM and microscopy

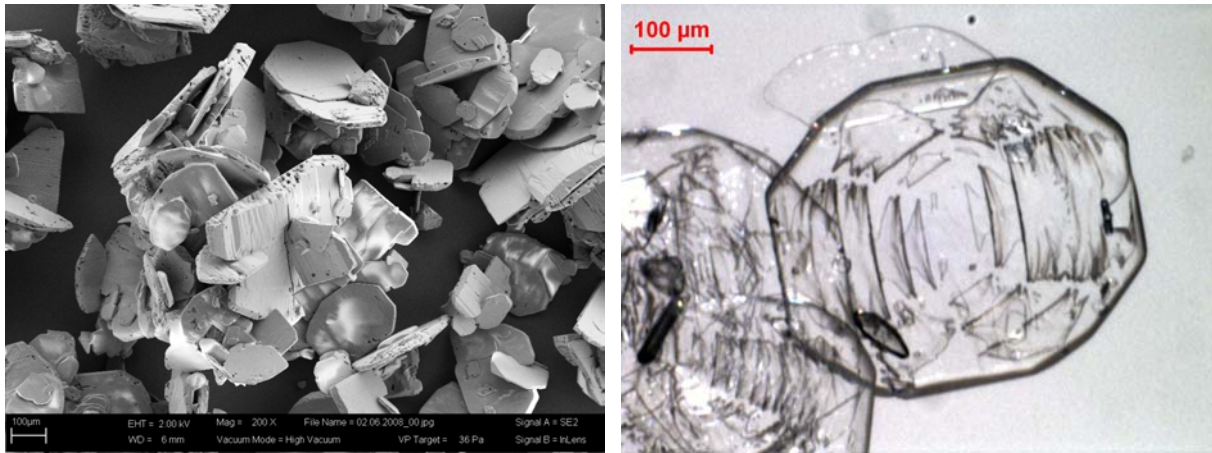


Figure 5-47: O-5-L-#2: SEM and microscopy

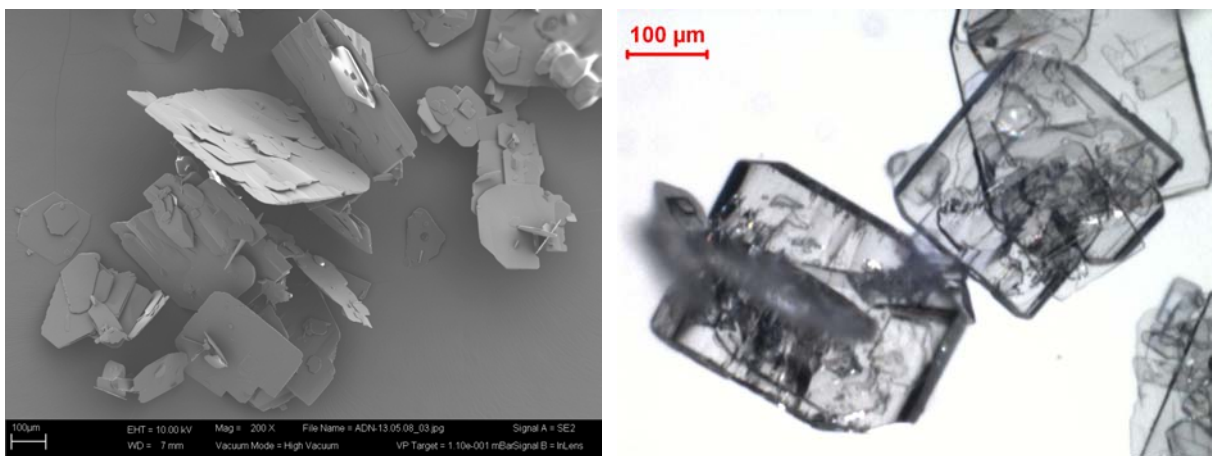


Figure 5-48: O-10-s: SEM and microscopy



Figure 5-49: O-10-L-#1: SEM and microscopy

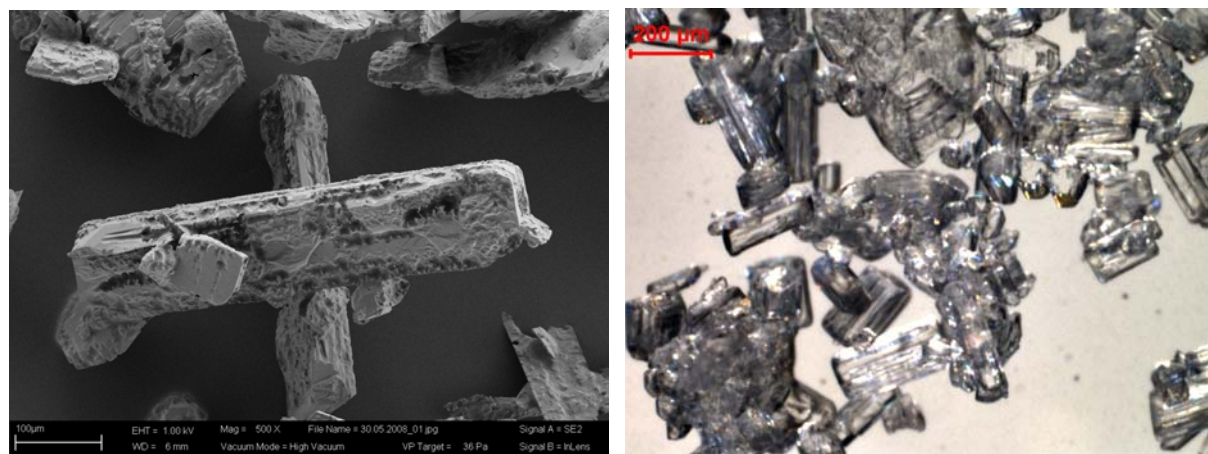


Figure 5-50: O-10-L-#2: SEM and microscopy

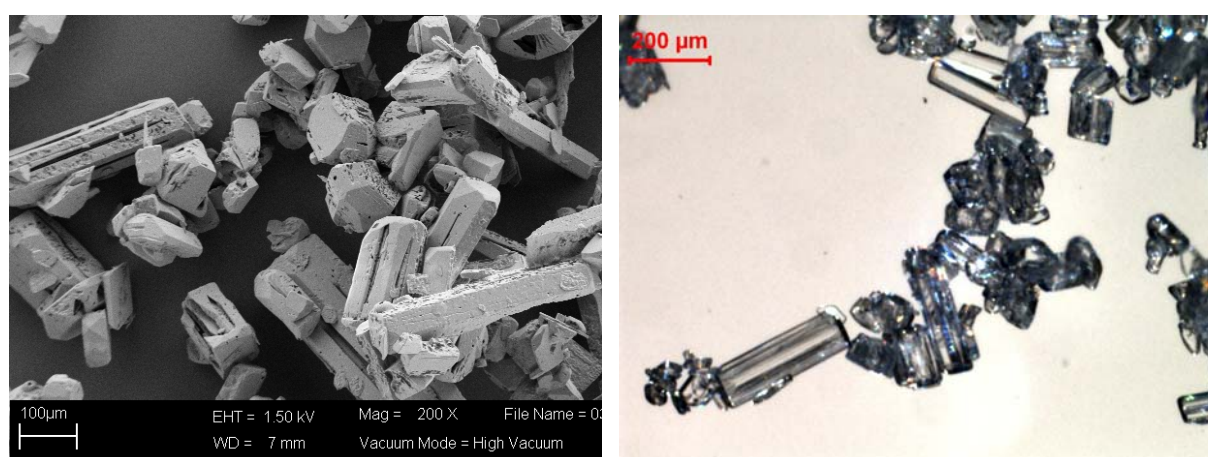


Figure 5-51: O-10-L-#3: SEM and microscopy

Thermal analysis

The results of the thermal analysis (DSC and TG) for ADN from 1-octanol are described in this paragraph.

The DSC of O-5-s (Figure 5-52, left) shows a sharp melting peak at $T_{\text{ONSET, O-5-s}} = 91.58 \text{ }^{\circ}\text{C}$ ($H_{\text{MELT, O-5-s}} = 119.4 \text{ J/g}$) and an additional endothermic peak at $T_{\text{ONSET}} = 59.02 \text{ }^{\circ}\text{C}$ ($H = 6.336 \text{ J/g}$). O-5-L-#1 (Figure 5-53, left) and O-5-L-#2 (Figure 5-54, left) both revealed one endothermic peak, the melting peak. For both samples, the peak is broadened; melting starts at $T_{\text{ONSET, O-5-L-#1}} = 90.31 \text{ }^{\circ}\text{C}$ ($H_{\text{MELT, O-5-L-#1}} = 114.4 \text{ J/g}$) respectively at $T_{\text{ONSET, O-5-L-#2}} = 86.89 \text{ }^{\circ}\text{C}$ ($H_{\text{MELT, O-5-L-#2}} = 90.97 \text{ J/g}$).

ADN from crystallization in the small vessel with a cooling rate of 10 K/h (O-10-s, Figure 5-55, left) provides a sharp melting peak at $T_{\text{ONSET, O-10-s}} = 94.00 \text{ }^{\circ}\text{C}$ with a corresponding melting enthalpy $H_{\text{MELT, O-10-s}} = 155.5 \text{ J/g}$.

A broadened melting peak is observed for O-10-L-#1 (Figure 5-56, left: $T_{\text{ONSET, O-10-L-#1}} = 89.56 \text{ }^{\circ}\text{C}$, $H_{\text{MELT, O-10-L-#1}} = 127.7 \text{ J/g}$) whereas the two experiments O-10-L-#2 and O-10-L-#3 do show other thermal behaviours: O-10-L-#2 has a broad peak at $T_{\text{ONSET, O-10-L-#2}} = 74.33 \text{ }^{\circ}\text{C}$ and a melting enthalpy $H_{\text{MELT, O-10-L-#2}} = 23.57 \text{ J/g}$. The

DSC from O-10-L-#3 possesses two endothermic peaks: one at $T_{\text{ONSET, O-10-L-#3}} = 57.84 \text{ }^{\circ}\text{C}$ ($H_{\text{PEAK}} = 6.263 \text{ J/g}$) and a melting peak at $T_{\text{ONSET, O-10-L-#3}} = 83.98 \text{ }^{\circ}\text{C}$ ($H_{\text{MELT, O-10-#3}} = 82.59 \text{ J/g}$).

The results of the TG analysis are summarized in Table 5-14 for a better overview. It was distinguished between the mass loss below $100 \text{ }^{\circ}\text{C}$ and above $100 \text{ }^{\circ}\text{C}$. The mass loss is given in percent of the initial mass [%]. The decomposition of ADN is completed for $T = 200\text{-}210 \text{ }^{\circ}\text{C}$. The total mass loss is additionally given.

Table 5-14: TG analysis of ADN from 1-octanol: Mass losses (ML) [%]

T	O-5-s	O-5-L-#1	O-5-L-#2	O-10-s	O-10-L-#1	O-10-L-#2	O-10-L-#3
ML < $100 \text{ }^{\circ}\text{C}$	0.96	0.43	1.56	0.92	0.53	6.89	1.58
ML > $100 \text{ }^{\circ}\text{C}$	96.40	98.31	96.66	95.89	98.04	91.38	96.98
total ML	97.36	98.74	98.22	96.81	98.57	98.27	98.56

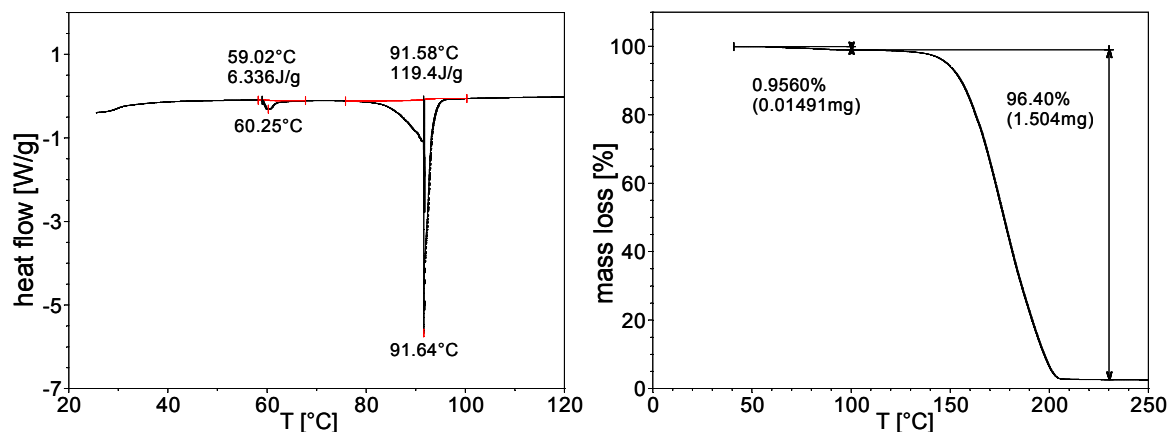


Figure 5-52: O-5-s: Thermal analysis: left: DSC, right: TGA, x-axis in T [°C]

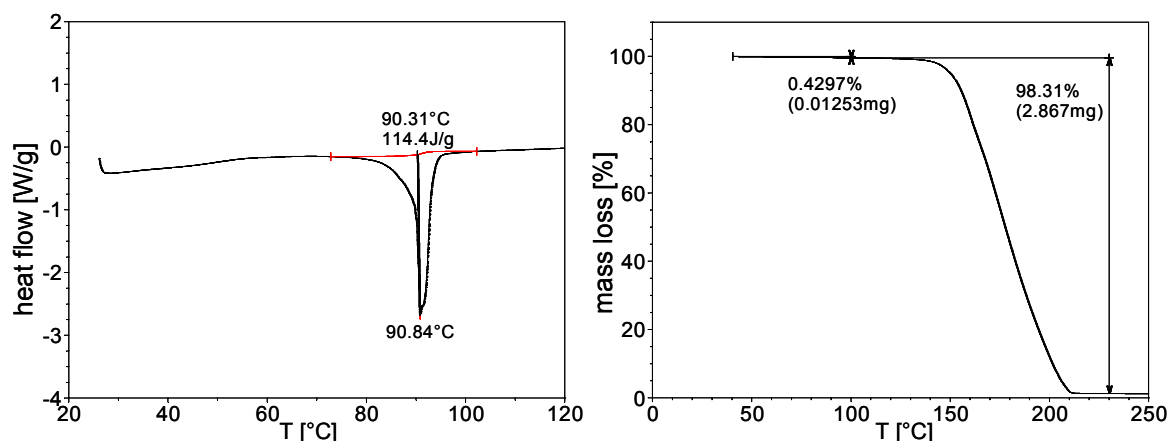


Figure 5-53: O-5-L-#1: Thermal analysis: left: DSC, right: TGA, x-axis in T [°C]

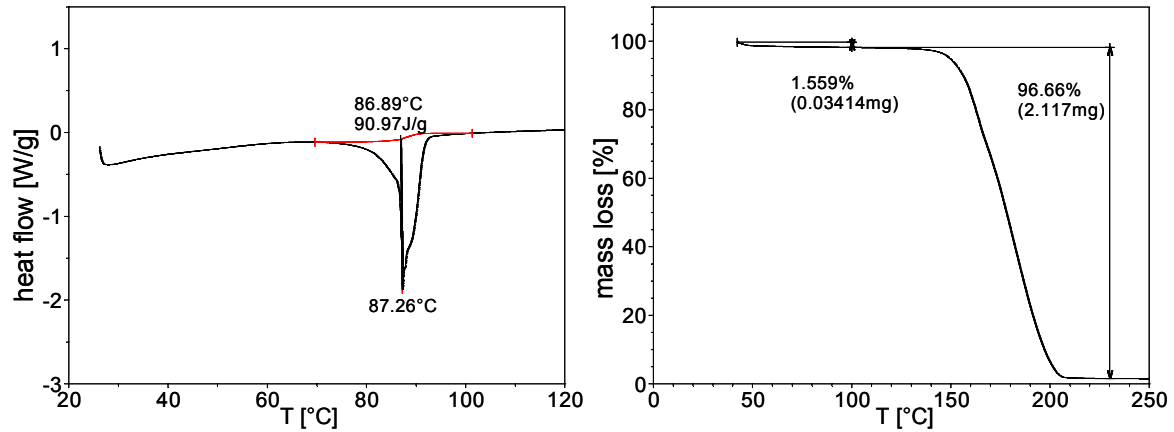


Figure 5-54: O-5-L-#2: Thermal analysis: left: DSC, right: TGA, x-axis in T [°C]

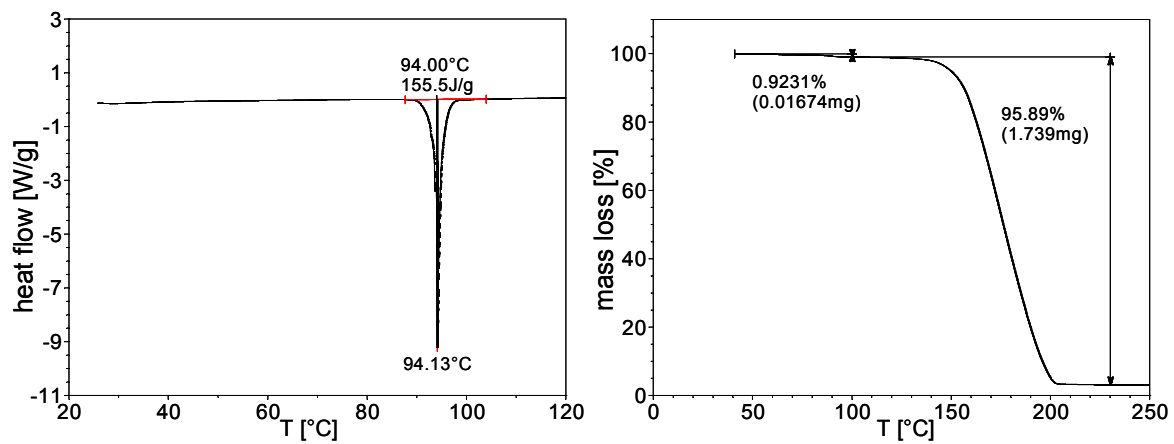


Figure 5-55: O-10-s: Thermal analysis: left: DSC, right: TGA, x-axis in T [°C]

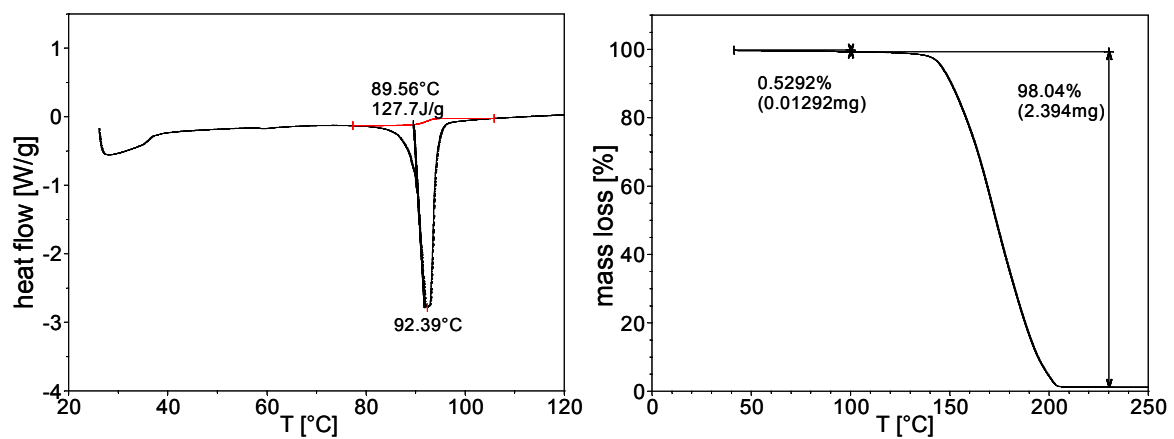


Figure 5-56: O-10-L-#1: Thermal analysis: left: DSC, right: TGA, x-axis in T [°C]

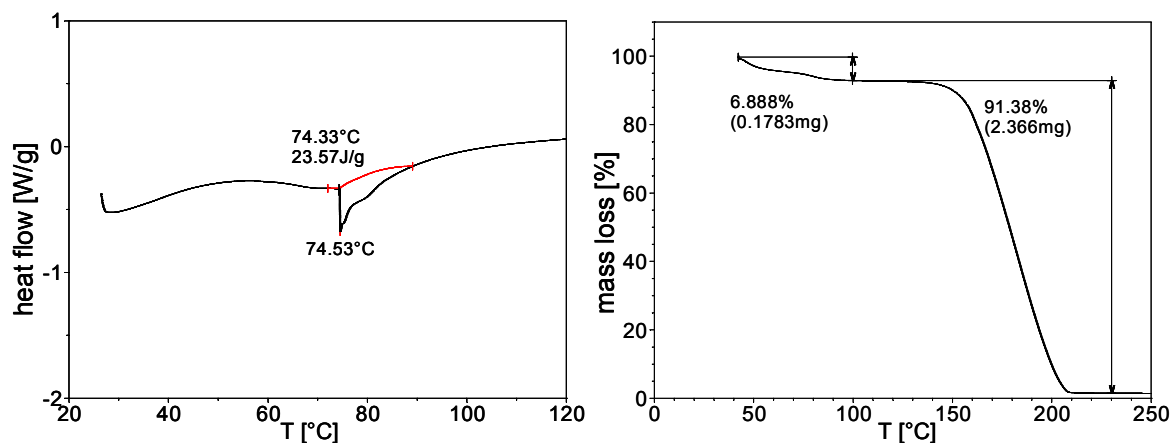


Figure 5-57: O-10-L-#2: Thermal analysis: left: DSC, right: TGA, x-axis in T [°C]

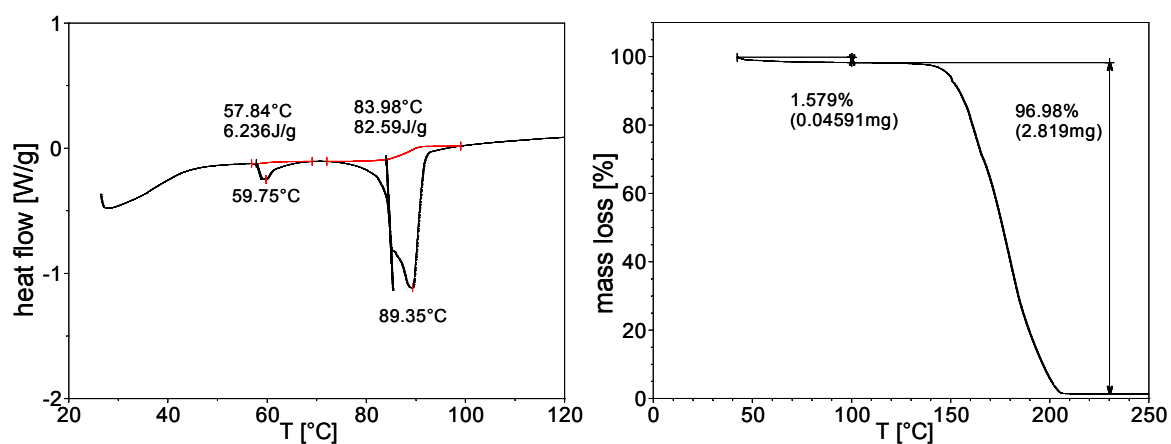


Figure 5-58: O-10-L-#3: Thermal analysis: left: DSC, right: TGA, x-axis in T [°C]

Comparison of the processes

The electrolytic conductivities for the seven crystallization processes are compared by plotting the EC values against the process temperature T. This is done for the cooling rate of 5 K/h in Figure 5-59 (left) and for the cooling rate of 10 K/h in Figure 5-59 (right). The values for O-5-L-#1 and O-5-L-#2 are approximately the same. The values for O-10-L-#1, O-10-L-#2 and O-10-L-#3 are also in the same range.

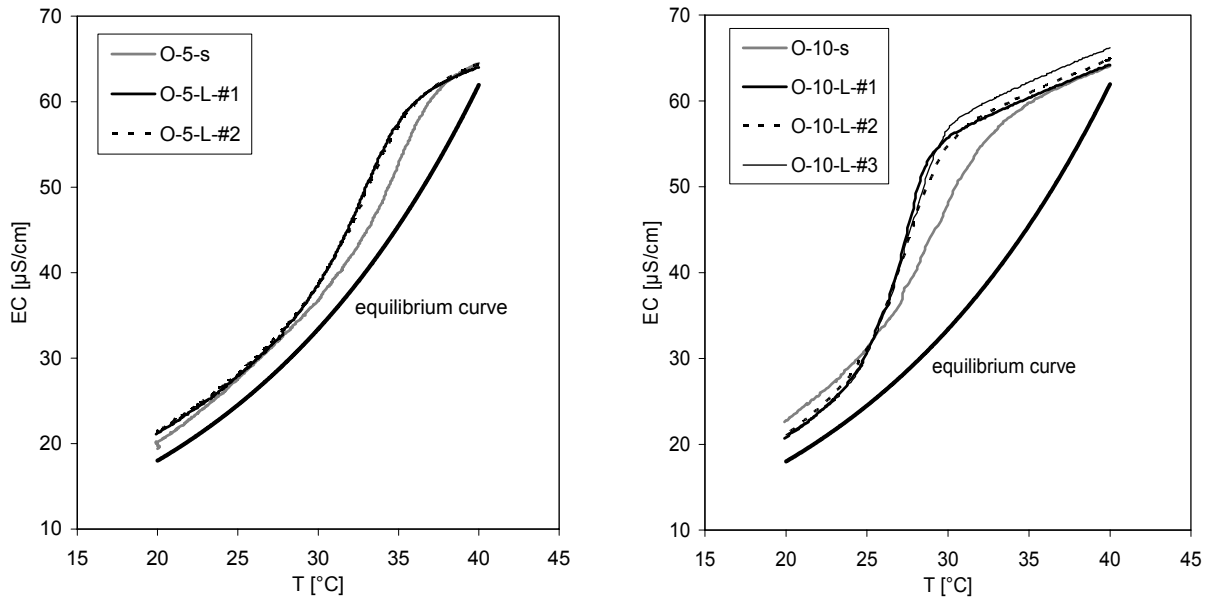


Figure 5-59: Comparison of the EC run of small scale and large scale experiments during the cooling phase for 5 K/h (left) and 10 K/h (right)

Process monitoring

The results of the process monitoring by Lasentec measurement and EC measurement for the large-scale experiments are plotted in Figure 5-60 (O-5-L) and Figure 5-61 (O-10-L) together with the process temperature T.

The cooling period of experiment O-5-L starts at $t = 11:02$ at 40°C . An increase of the numbers of chord lengths ($1 - 10\ \mu\text{m}$) is detected starting at $t = 11:40$ / $T = 36.6^{\circ}\text{C}$ on. About one hour later, at $t = 12:35$, the number of chord lengths is nearly on a constant level (approximately. 40 counts/s), it is only slightly increasing with time. The initial value for EC at $T = 40^{\circ}\text{C}$ is $64.5\ \mu\text{S}/\text{cm}$. EC is decreasing while no particles are detected by the Lasentec ($36.6^{\circ}\text{C} < T < 32.2^{\circ}\text{C}$). After $t = 11:40$, a rapid decrease of EC is observed.

The initial EC at $T = 40^{\circ}\text{C}$ is $64.9\ \mu\text{S}/\text{cm}$ for O-10-L. The cooling starts at $t = 11:12$. From this time on, EC is decreasing linearly. The number of chord lengths ($1 - 10\ \mu\text{m}$) that are detected by Lasentec is increasing from approximately 2 counts/s up to 10 counts/s at $t = 11:53$ ($T = 32.9^{\circ}\text{C}$). At $t = 12:10$ ($T = 30.2^{\circ}\text{C}$), a strong increase of the number of counts per second to 80 counts/s is taking place within minutes. EC decreased to $18.8\ \mu\text{S}/\text{cm}$ one hour after the cooling phase was finished.

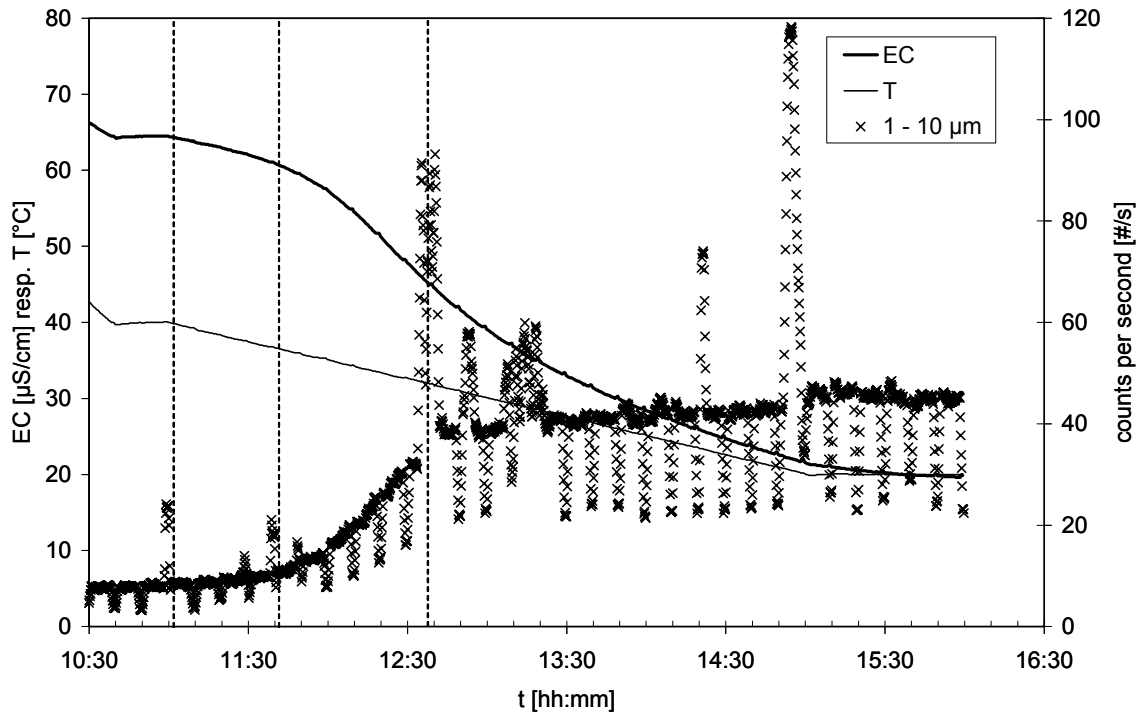


Figure 5-60: O-5-L: Lasentec measurement

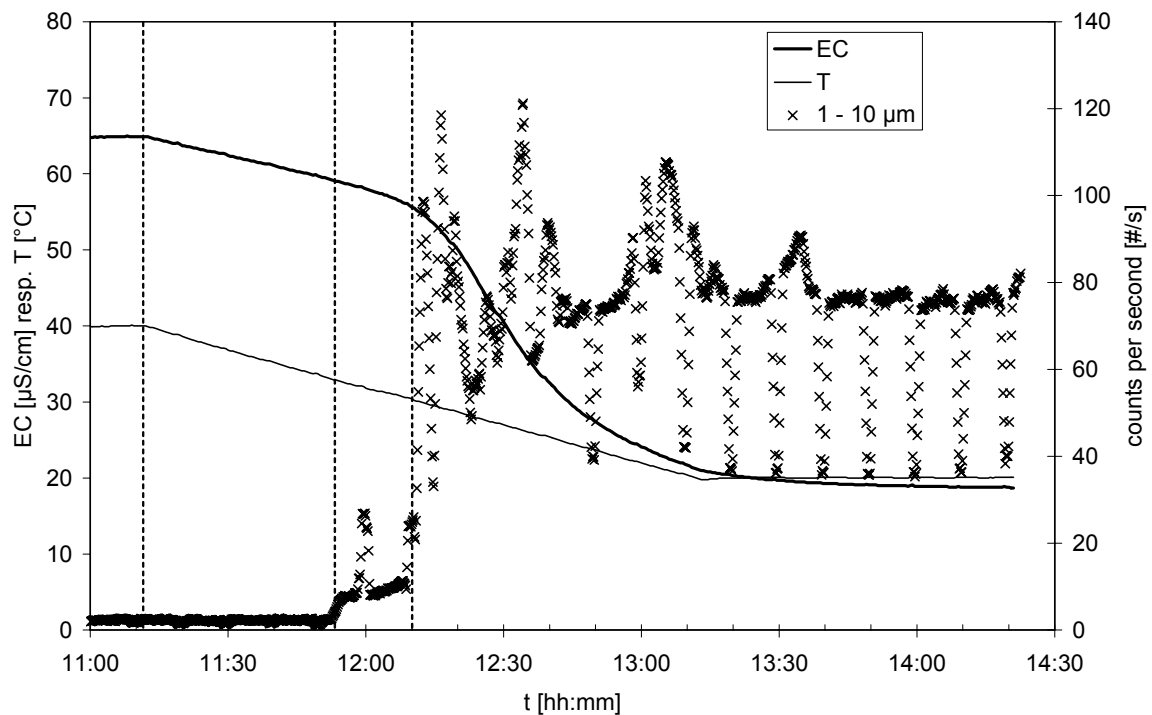


Figure 5-61: O-10-L: Lasentec measurement

Supersaturation

The development of supersaturation for the four process conditions is shown in this paragraph. The supersaturations are determined by comparing the actual process

concentration with the equilibrium concentration at the same temperature (see also Chapter 11, Figures 11-11 and 11-12). All four processes are starting at $S = 1$.

For O-5-s (Figure 5-62, left), supersaturation is increasing within 22 min to $S = 1.08$ ($T = 38.1$ °C). S is constant until $t = 00:42$ ($T = 36.5$ °C). Then it is decreased to a minimum saturation $S = 1.04$ and afterwards it increased again to $S = 1.11$ ($t = 02:32$, $T = 27.4$ °C). S is constant for the remaining cooling period. At $t = 04:02$ ($T = 20$ °C), S is reduced within an hour to $S = 0.99$.

In the large-scale experiment O-5-L (Figure 5-62, right), supersaturation is increasing to $S = 1.17$ until $t = 01:09$ ($T = 34.4$ °C). Then, the supersaturation is reduced to $S = 1.13$ ($t = 01:39$ to $t = 03:09$ respectively $T = 32$ °C to $T = 24.5$ °C). After this plateau, supersaturation increased again to $S = 1.18$ ($t = 04:02$, end of the cooling phase). Supersaturation is reduced to 1.08 within one hour.

By cooling with 10 K/h in the small batch (O-10-s, Figure 5-63, left), supersaturation is increasing to $S = 1.33$ ($t = 00:53$, $T = 31.2$ °C). After reaching this maximum, a decrease of supersaturation to $S = 1.23$ ($t = 01:33$, $T = 24.8$ °C) is occurring followed by a second maximum $S = 1.26$ ($t = 02:03$, $T = 20$ °C) at the end of the cooling phase. One hour after the cooling phase was ended, S is reduced to 1.07 ($t = 03:03$, $T = 20$ °C).

Supersaturation is linearly increasing within $t = 01:07$ ($T = 28.8$ °C) to $S = 1.54$ for O-10-L (Figure 5-63, right). After reaching this maximum value, a rapid decrease of the supersaturation to $S = 1.18$ occurs until the cooling phase is finished ($t = 01:37$, $T = 23.8$ °C). A second maximum ($S = 1.26$, $t = 01:47$, $T = 22.1$ °C) is occurring before supersaturation is reduced to $S = 1.03$ during the relaxation phase of one hour ($t = 03:07$).

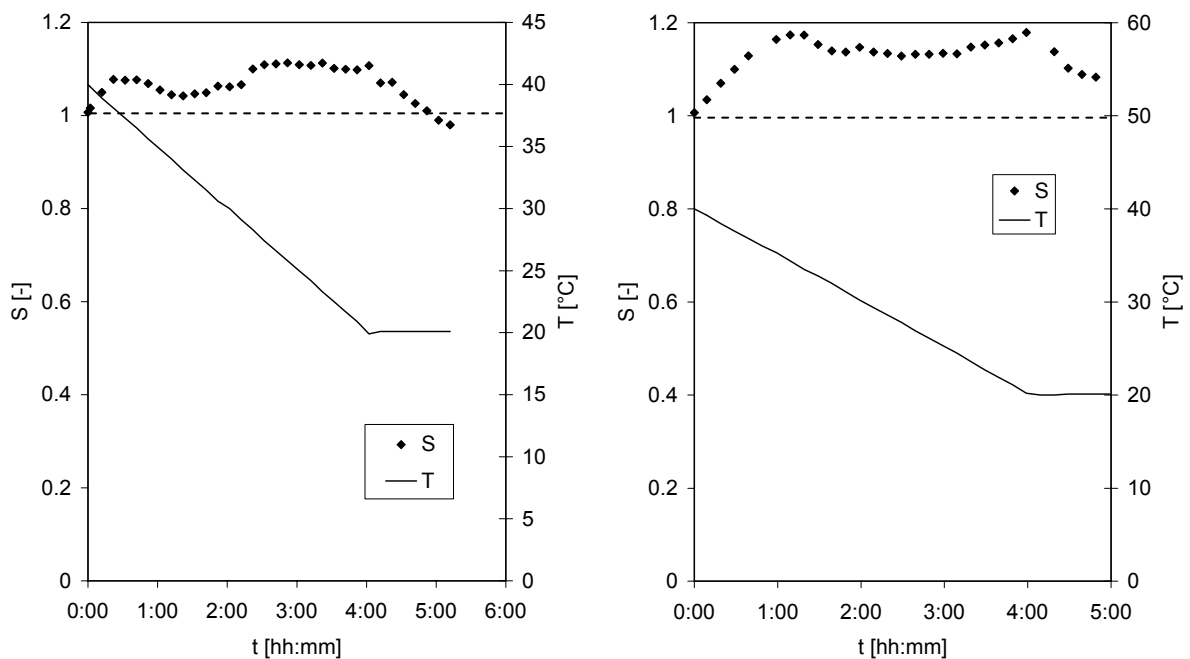


Figure 5-62: Supersaturation S during the crystallization process for O-5-s (left) and O-5-L (right)

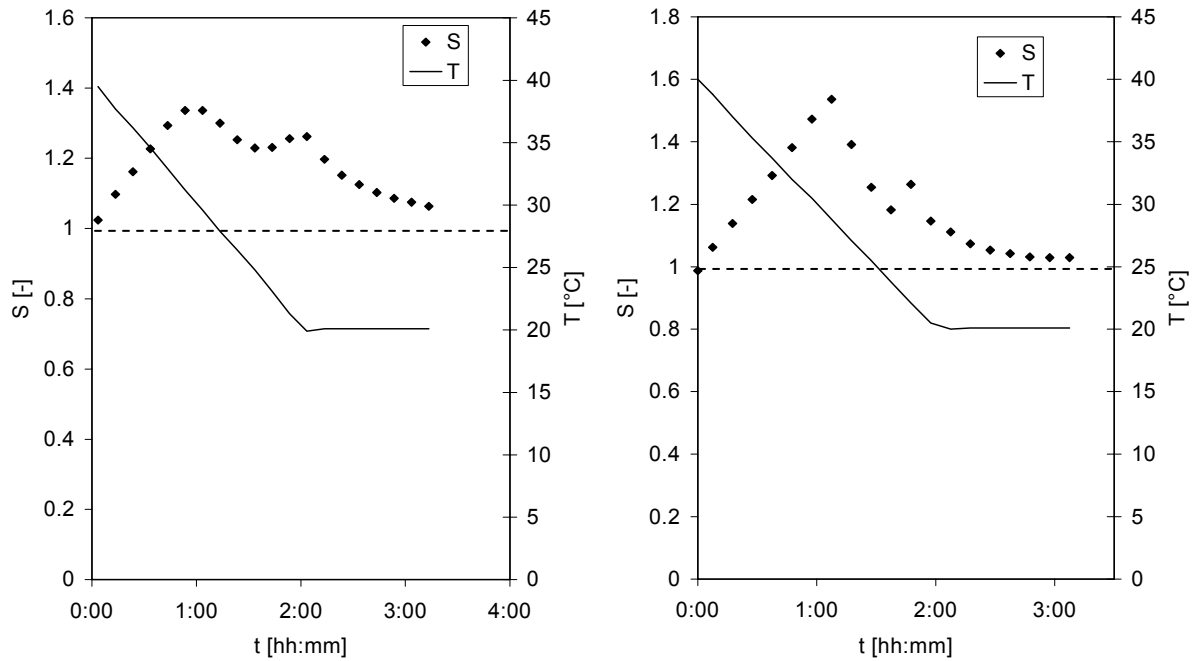


Figure 5-63: Supersaturation S during the crystallization process for O-10-s (left) and O-10-L (right)

5.2.4 Dynamic viscosity

The dynamic viscosities were measured for both solvents in the temperature range from 20 °C to 40 °C (Figure 5-64). There was no shear-rate dependency observed.

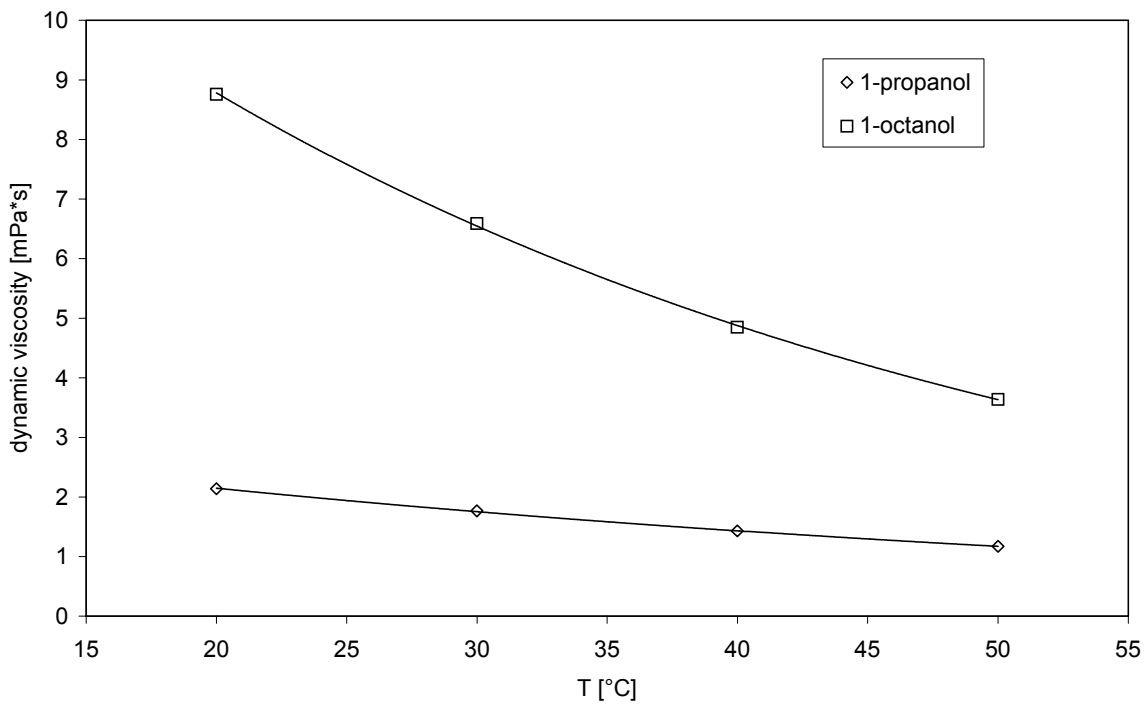


Figure 5-64: Dynamic viscosities of the solvents 1-propanol and 1-octanol

5.2.5 X-ray powder diffraction of ADN

For ADN recrystallized from 1-octanol and 1-propanol in the natural cooling experiments, X-ray powder diffraction was carried out. The XRD patterns shown in Figure 5-65 were evaluated by means of Rietveld analysis yielding the Miller indices hkl , the positions in 2θ -scale and intensities for each peak. Precipitated ADN was used as reference as it is assumed to have no preferred orientation because of its compact, nearly spherical shape (see Chapter 11, Figure 11-13). The peak areas of the different patterns were scaled and the normalized intensities of the recrystallized samples were compared to the normalized intensities of the reference. The quotients obtained from this method are listed in Table 5-15 for the relevant faces together with the peak positions in 2θ -scale. The crystal faces obtained from the morphology calculation are analyzed in this context including higher order peaks.

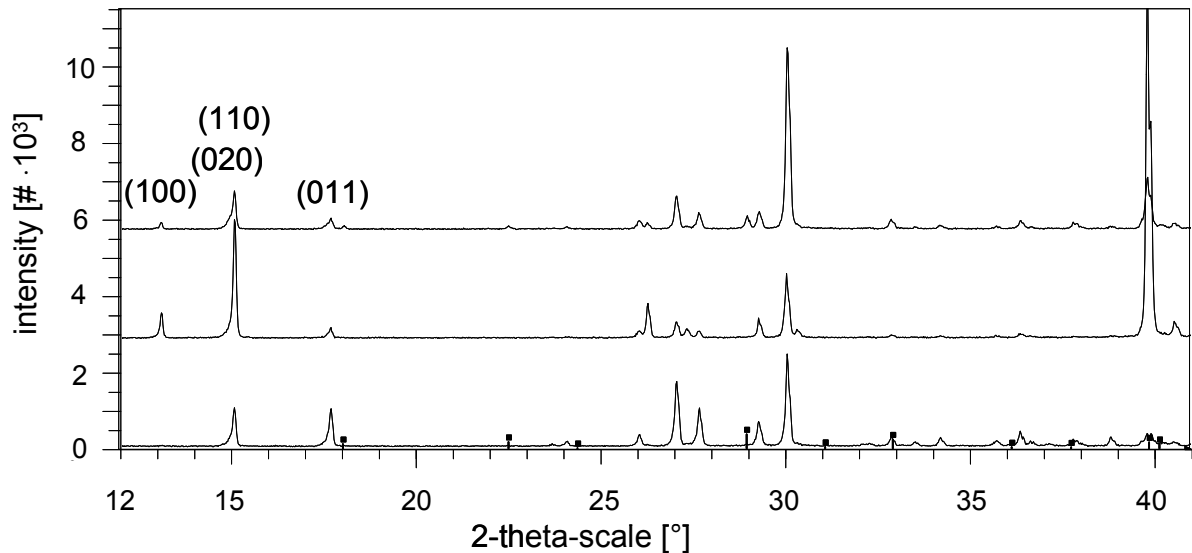


Figure 5-65: Diffraction patterns of ADN recrystallized from 1-octanol (upper pattern), 1-propanol (middle) and of the precipitated sample as reference (lower pattern). Bars indicate the peak positions of ammonium nitrate

Table 5-15: Quotients of normalized intensities of recrystallized to precipitated ADN

hkl	2θ	normalized intensities			
		1-propanol	average value	1-octanol	average value
(100)	13.02919	7.78		3.68	
(200)	26.23073	9.43	8.77	3.26	3.22
(300)	39.79869	9.10		2.74	
(020)	14.87235	0.16	0.20	1.83	1.54
(040)	30.00288	0.23		1.26	
(110)	15.01006	0.85	1.11	0.56	0.69
(220)	30.28570	1.38		0.82	
(011)	17.62081	0.08	0.09	0.20	0.22
(022)	35.67646	0.11		0.24	
(111)	23.65713	0.06	0.06	0.25	0.25
(002)	32.23977	0.08	0.08	0.27	0.27

5.3 Comparison of simulated and experimental morphology

As described in Chapter 5.1 ADN was investigated by computer simulation methods to find possible morphological important crystal faces and to clarify their molecular structure. In parallel, crystallization experiments were carried with different solvents (Chapter 5.2.3). The objective of this chapter is to identify the crystal faces appearing in the crystallization process. This is done by measuring and comparing the angles between the crystal faces for both the simulated and experimental morphologies. Microscopic pictures are taken from ADN samples. The crystal shape of ADN from both solvents is plate-shaped so the crystals have a preferred orientation when they are placed on the microscope's sample carrier. The angles that are measured from the microscopy pictures do not represent the angles between the crystal faces but the angles between the projected crystal faces. To be able to compare these angles with the simulated results, the simulated morphologies are arranged the way that they have the same orientation as the experimental morphologies. Now it is possible to deduce the indexing of the crystal faces from comparing the angles. The original simulated crystal shape is reduced to the actually appearing crystal faces.

5.3.1 ADN / 1-propanol

Figure 5-66 (left) shows an example of an ADN crystal from 1-propanol. The angles that are measured are also drawn in. Figure 5-66 (right) shows the BFDH morphology oriented in such a way that the (100) plane is parallel to the plane of projection. After comparing the angles, the simulated morphology was reduced to the (100), (011) and (020) crystal faces (Figure 5-67) and the proportions were modified for a better comparison with the experimental crystals. From SEM pictures, a fourth face was detected and the morphology was improved by adding the (110) face to the simulated crystal shape (Figure 5-68).

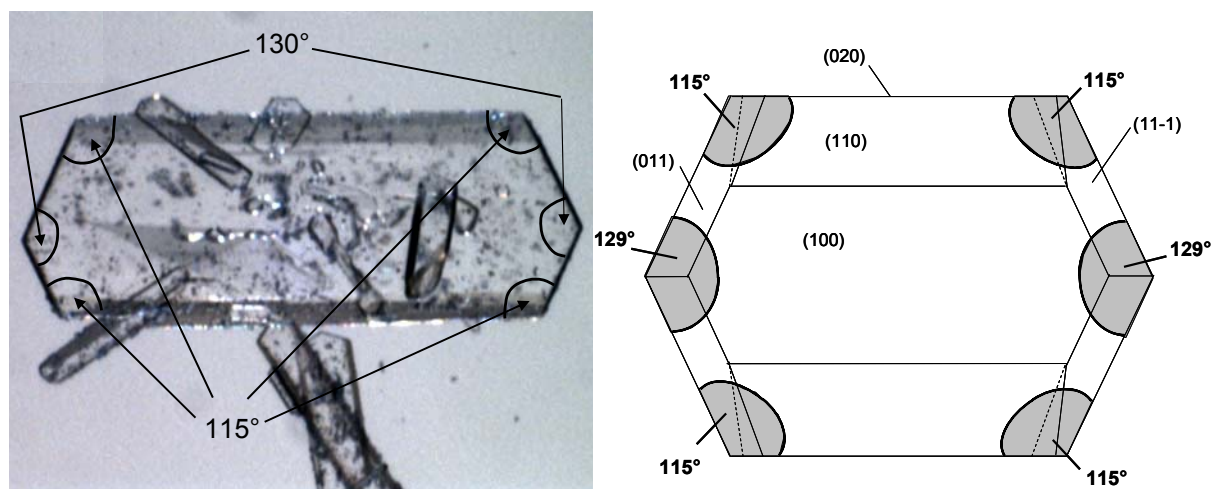


Figure 5-66: ADN from 1-propanol: angles, left: crystal from experiment, right: simulated morphology

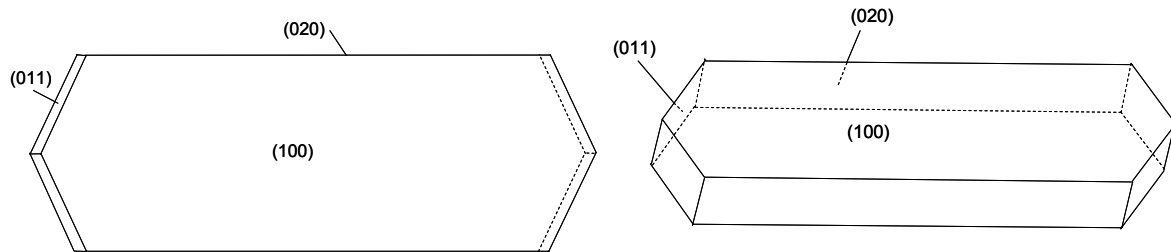


Figure 5-67: Simulated ADN morphology

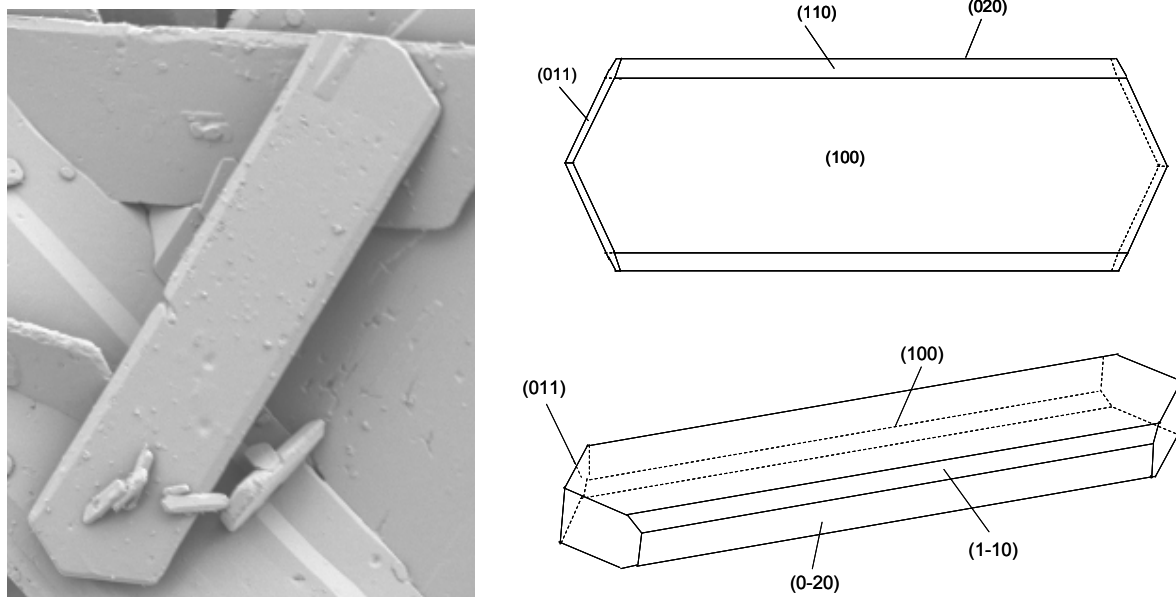
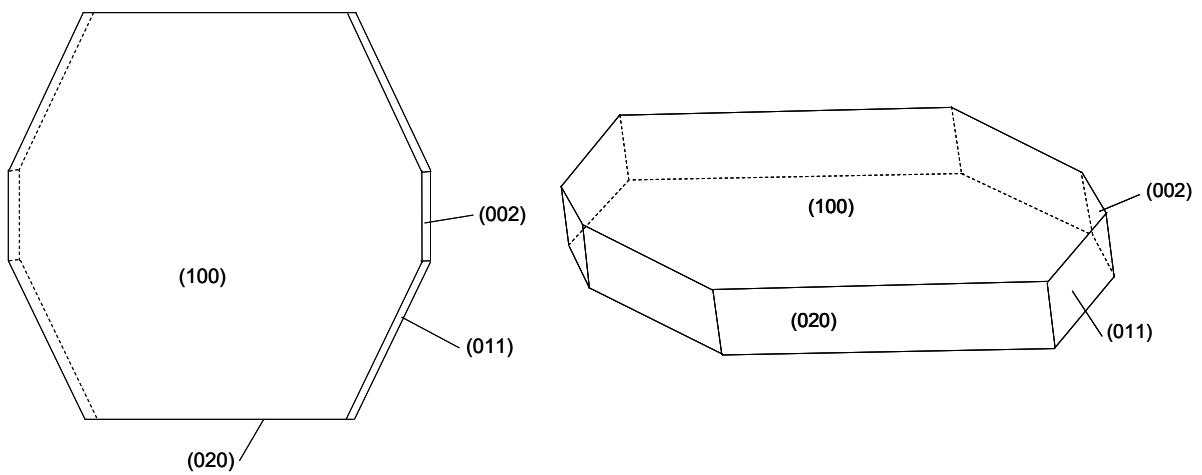
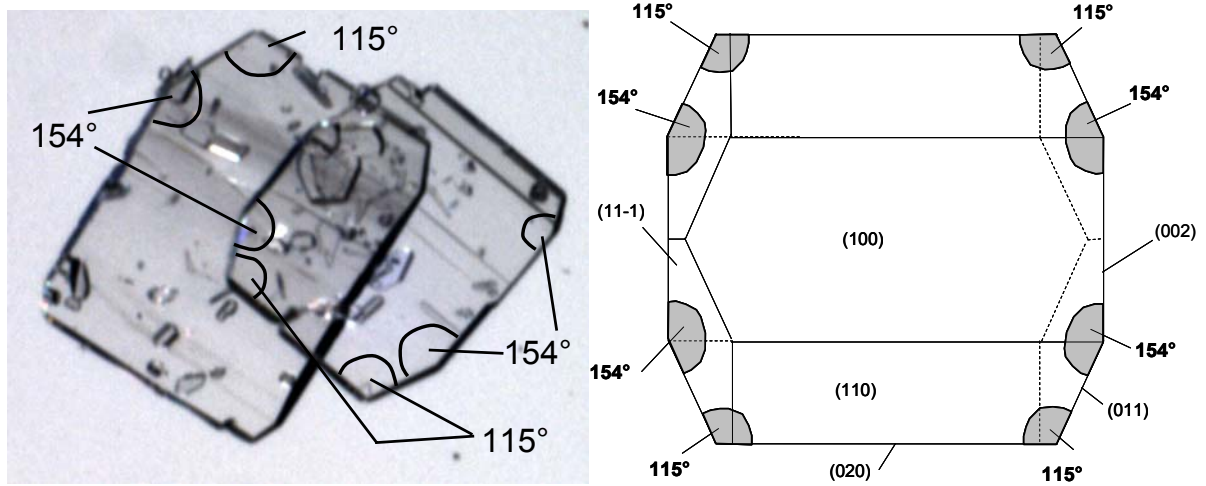


Figure 5-68: Refined morphology: ADN from 1-propanol

5.3.2 ADN / 1-octanol

An ADN crystal from 1-octanol with the corresponding angles is visualized in Figure 5-69 on the left. On the right, a projection of the BFDH morphology with the additional (002) face is shown. The angles measured for the crystal obtained from experiment are also detected in the simulated crystal shape so the occurring crystal faces can be identified. Figure 5-70 shows the simulated morphology adapted to the experimentally obtained crystal shape.



6 Discussion

6.1 The ADN unit cell

6.1.1 Geometrical setup

The ADN unit cell was constructed by using the atom positions published by Gilardi et al. [GIL97] in combination with unit cell dimensions determined at room temperature because they were measured in the same temperature range as the crystallization experiments in this work were accomplished. Both, the data published by Östmark et al. [ÖST00] and the data from ICT/ANKA are measured at ambient temperature ($T_{\text{ÖSTMARK}} = 293 \text{ K}$ resp. $T_{\text{ICT/ANKA}} = 291 \text{ K}$). In the following, it is explained why the data from ICT/ANKA was used for the preparation of the ADN unit cell instead of the data published by Östmark et al. [ÖST00]. The thermal behaviour of the ADN crystal was investigated by Löbbecke [LÖB99] and Sorescu et al. [SOR99]. Löbbecke [LÖB99] considered the thermal behaviour of ADN at ambient pressure in the temperature range $T = -150 \text{ °C}$ to $T_{\text{MELT}} = 90 \text{ °C}$ by DSC analysis. He stated that no solid-solid phase transition is taking place in the mentioned temperature range so the density is continuously running with the temperature without any discontinuity. Sorescu et al. [SOR99] determined the thermal expansion behaviour of the unit cell by means of molecular dynamics calculations. His results are shown together with the experimental data published by Ritchie et al. [RIT03], Gilardi et al. [GIL97], Östmark et al. [ÖST00] and the data received from the synchrotron measurements (ICT/ANKA) in Figure 6-1. The absolute crystal density calculated from molecular dynamic methods is diverging from the crystal density obtained from experiments. However, the volumetric thermal expansion coefficient γ determined from Sorescu's data (γ_{SORESCU}) and the experimental data of Gilardi et al. and Ritchie et al. (γ_{EXP}) are in the same range ($\gamma_{\text{SORESCU}} = 1.70 \cdot 10^{-4} \text{ K}^{-1}$, $\gamma_{\text{EXP}} = 1.68 \cdot 10^{-4} \text{ K}^{-1}$). γ is calculated according to Equation 6-1 with the data listed in Table 6-1. By a linear extrapolation of the densities from Gilardi et al. and Ritchie et al. to ambient temperature by means of the thermal expansion coefficient, it is obvious that the data from ICT/ANKA fits better than the data published by Östmark et al. (Figure 6-1).

$$\gamma = -\frac{1}{\rho_1} \cdot \frac{\rho_1 - \rho_2}{T_1 - T_2} \quad \text{Equation 6-1}$$

Table 6-1: Data used for calculating the thermal expansion coefficient

	T_1 [K]	T_2 [K]	ρ_1 [g/cm ³]	ρ_2 [g/cm ³]	γ [K ⁻¹]
[RIT03], [GIL97]	223	90	1.831	1.872	$1.68 \cdot 10^{-4}$
[SOR99]	273	100	1.736	1.787	$1.70 \cdot 10^{-4}$

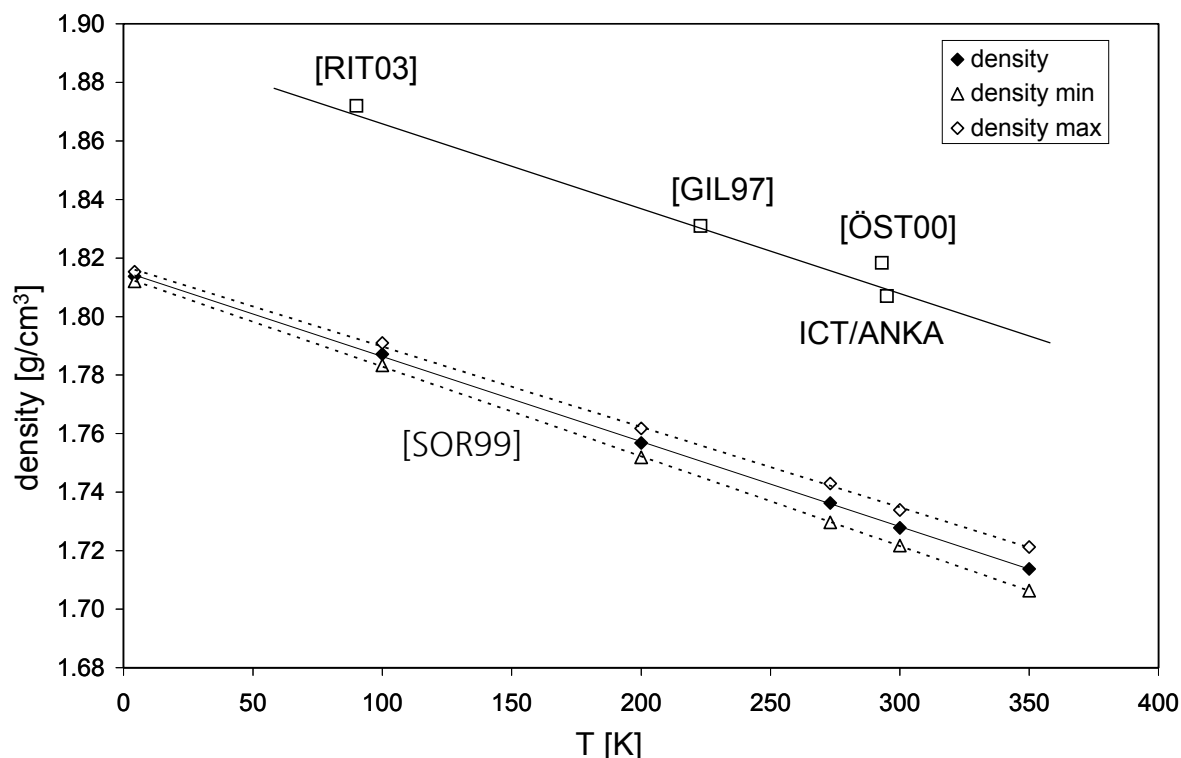


Figure 6-1: The volumetric thermal expansion of the ADN unit cell illustrated by the temperature dependant crystal density: Comparison of literature data and data determined at the synchrotron source ANKA

6.1.2 The application of the COMPASS force field to the dinitramide ion

As reported in Chapter 5.1.1 the dinitramide ion was not treated correctly in terms of charges, force field types and bonds when the COMPASS force field was applied for the minimization of the unit cell. For example, the N2-N1-N3 bond angle increased from 113.19° (original crystal structure from Gilardi et al. [GIL97]) to 180°. So the general geometry of the dinitramide ion changed dramatically by applying COMPASS directly to the ADN structure. Therefore, a special focus was put on the dinitramide ion by adapting these parameters manually before the minimization was carried out.

Because the dinitramide ion exhibits resonance structures (Figure 6-2) as described by Löbbecke [LÖB99], all bonds were set to partial double bonds. Therefore, the force field for the N1 molecule was chosen as n2a what means that the hybridization is sp² and an aromatic bond is present. COMPASS proposed n2= (sp², 1 double bond, non-aromatic) as force field type for N1 which is not describing this atom correctly. The nitrogen atoms N2 and N3 are both participating in nitro groups. COMPASS provides an adequate force field type for them: They are typed as n3o, with a sp² hybridization for nitrogen atoms in nitro groups. The same with the oxygen atoms of the dinitramide ion: The force field type o12 (sp² hybridization) is especially provided for oxygens in nitro groups. The atomic charges of the dinitramide ion were determined by a single molecule calculation using DFT methods (Gaussian 03, DFT method: B3LYP, basis set: 6-31G(d,p)).

The results are listed in Table 5-2 as $q_{\text{DN,DFT}}$ and are compared to the calculations of Ritchie et al. [RIT03] and to the results of Nagao [NAG98]. The ICT/DFT values have been calculated by using the same DFT method as Ritchie. Nagao has determined the charge distribution of the dinitramide ion by using spherical atom X-ray refinements. The charges calculated in this work are lying in between the values of Ritchie [RIT03] and Nagao [NAG98], they are closer to the charges calculated by Ritchie. The calculated atomic charges are thus ensured to be in a reliable range and are applied for the minimization of the unit cell.

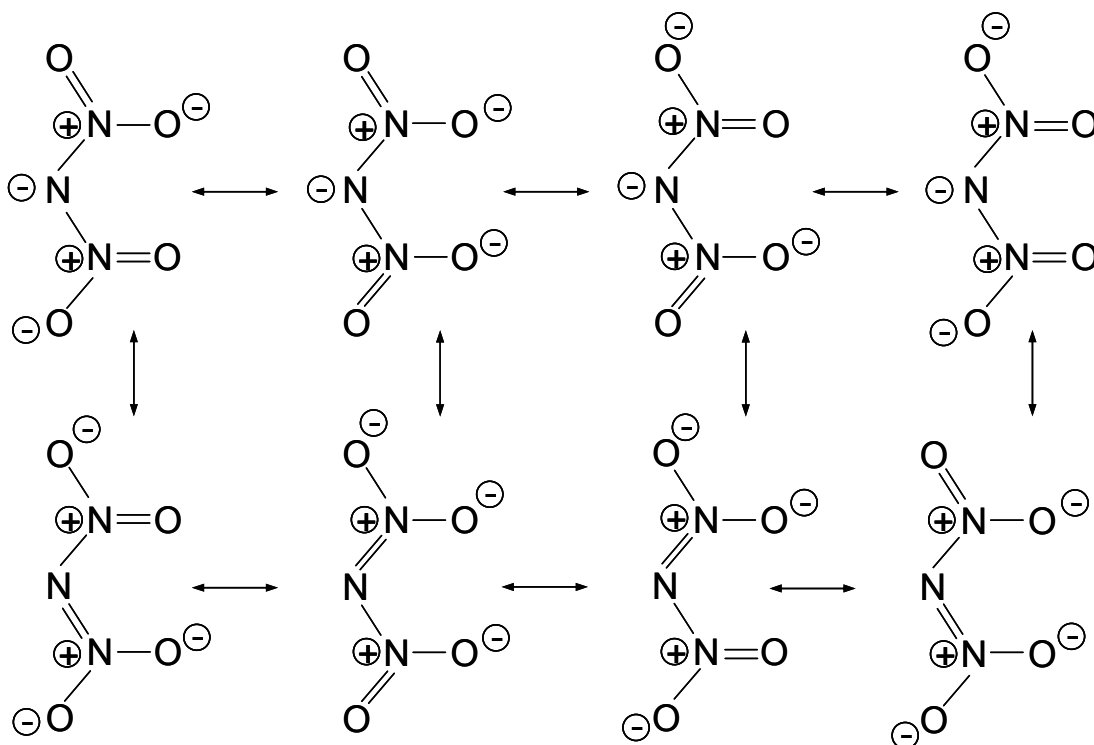


Figure 6-2: Resonance structures of the dinitramide ion published by Löbbecke [LÖB99]

6.1.3 Comparison of the minimized and original ADN unit cell

The energetic minimization of the ADN unit cell was done by using the parameters described in Chapter 6.1.2.

The crystal structure of the ADN unit cell changed to a large extent during the minimization. Especially the bond angles and torsion angles of the dinitramide ion are modified compared to the experimental geometry published by Gilardi et al. [GIL97]. The dinitramide ion is getting more twisted by minimizing the starting geometry: Three of four torsion angles are increased after the minimization (see Table 6-2). Figure 5-3 and Figure 5-4 visualize the unit cell before and after minimization, obviously characterized by a displacive rearrangement of the unit cell. Because one aim of this work is to test the applicability of the COMPASS force field for ADN, the minimized unit cell is used for the following calculations despite its deficiencies in terms of geometry. Additionally, the unit cell with the original atom positions published by Gilardi et al.

[GIL97] is used for calculating the vacuum morphologies (Chapter 5.1.2) and the interaction energies (Chapter 5.1.3).

Table 6-2: Torsion angles before and after minimization

α_{TORSION} [°]	after minimization (DFT)	before minimization [GIL97]
N3 – N1 – N2 – O1	-63.01	-23.74
N3 – N1 – N2 – O2	156.57	162.19
N2 – N1 – N3 – O3	175.69	157.24
N2 – N1 – N3 – O4	-45.39	-28.27

6.2 Computer simulation of the crystal shape of ADN

6.2.1 Vacuum morphology calculation

Both the BFDH and the growth morphologies were calculated on the basis of the minimized unit cell by using the morphology module of Materials Studio. 3-D views of the crystal shapes resulting from these calculations are shown in Figure 6-3 (see Chapter 5.1.2.1, Figure 5-5 and 5-6 for more details). The vacuum morphologies simulated by the two methods are different in shape. The crystal faces that are defining the crystal habit are listed in Chapter 5.1.2.1, Table 5-6.

The morphology calculated by the pure geometric BFDH method is of a compact shape with a ratio between the longest and the shortest diameter of the crystal habit (= aspect ratio) of 1.713. According to Bravais [BRA13] and Friedel [FRI07] the important growth planes are those with large lattice-plane spacing d_{hkl} . This is rationalized by assuming that the ease of adding a plane is proportional to its thickness. Thin planes are thus growing faster and have larger center-to-face distances [ACC04].

The growth morphology of ADN is plate-like with an aspect ratio of 3.816. The faces with a low attachment energy E_{ATT} are defining the shape as it is assumed that the growth rate of a face is proportional to E_{ATT} .

The crystal faces (100) and (11-1) exhibit relatively large lattice-plane spacings ($d_{100} = 6.797 \text{ \AA}$, $d_{11-1} = 4.396 \text{ \AA}$). For this reason they are of morphological importance for the BFDH morphology. Their attachment energies ($E_{\text{ATT},100,\text{MIN}} = -472.26 \text{ kJ/mol}$ and $E_{\text{ATT},11-1,\text{MIN}} = -535.87 \text{ kJ/mol}$) are three to four times the attachment energy of the morphological most important crystal face (020) of the growth morphology $E_{\text{ATT},020,\text{MIN}} = -149.97 \text{ kJ/mol}$. As result, (100) and (11-1) are not arising from the growth morphology calculation; they are supposed to grow very fast so they are rapidly growing out and are not participating in the crystal habit.

The original unit cell was used for a comparative morphology calculation (Chapter 5.1.2.2, Figure 5-7 and Table 5-7). It results in a very similar BFDH morphology as obtained from the calculation from the minimized unit cell. The lattice spacings are

changed to a small extent after the minimization of the unit cell. This leads to a slightly different morphology. The differences in the BFDH morphologies are too small to be realized so just the morphology obtained from the minimized unit cell is shown in Figure 6-3.

The calculation of the growth morphology by using the original unit cell leads to two new morphological important crystal faces: the (111) and the (11-1) face are both part of the morphology but their total part is only 5.16% (see Figure 6-4). On the other hand, the (10-2) face is not present in the new morphology. Again, the (100) has a high attachment energy ($E_{\text{ATT},100,\text{ORIGINAL}} = -3044.58 \text{ kJ/mol}$); this is an indication for rapid growth and a hint for a possible outgrowth of the morphology.

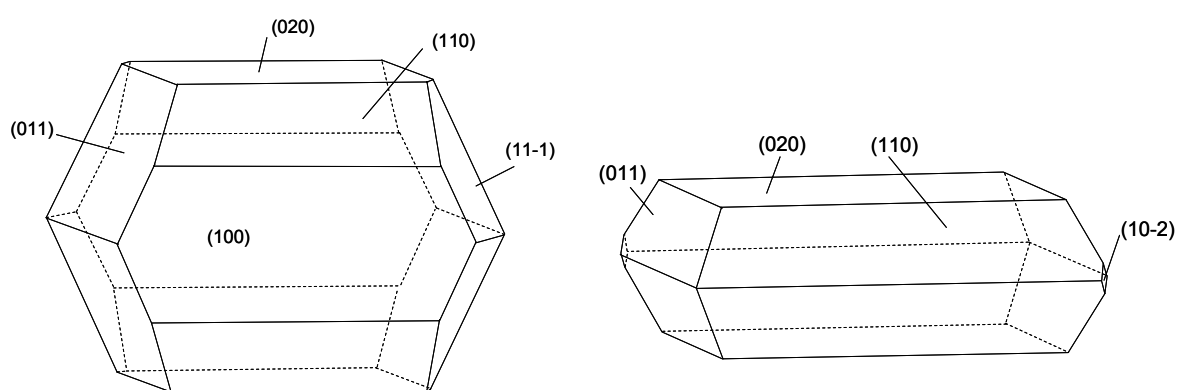


Figure 6-3: Simulated vacuum morphologies of ADN from the minimized unit cell: BFDH morphology (left), growth morphology (right)

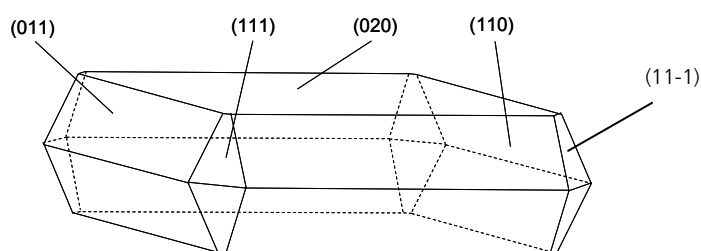


Figure 6-4: Vacuum morphology of ADN simulated by the growth method starting from the original unit cell

6.2.2 The growth faces and their interactions with building blocks and foreign molecules

Starting from the minimized unit cell and the calculated morphologies, the possible growth faces were cleaved and visualized on a molecular level in Chapter 5.1.3. The two different kinds of crystal faces that were characterized are either consisting of neutral lattice layers or of alternating positive and negative charged layers. In Chapter 5.1.4, the interaction energies of the cleaved growth faces with solvent molecules (1-propanol and 1-octanol), with the ammonium ion, the dinitramide ion and with a potassium ion as

impurity were calculated for both the minimized unit cell and the original unit cell. This was done because the geometry of the unit cell changed to a large extent during the minimization procedure. The comparison of the interaction energies calculated from the minimized and the original unit cell shows that they are mostly in the same range.

The interaction energies of the crystal faces with the solvent molecules are compared to the interaction energies between the faces and additional ADN ions (Chapter 5.1.4 Figure 5-13). It is noticeable that the amount of interaction energies between solvent molecules and crystal faces are much lower than between the ammonium ion or the dinitramide ion and the crystal faces. This implies that the solvents do not influence the crystal shape by disturbing the incorporation of the ADN ions into the crystal lattice by the occupation of lattice positions.

The calculation of interaction energies of ammonium and dinitramide ions with morphology defining crystal faces (see also Chapter 6.2.3) show that the interaction energies with the most important crystal face (100) are about 35 and 24 times smaller than the interaction energy with the (110)₁ and (110)₂ face, respectively. This indicates a relatively fast growth of the (110) face in contrast to the (100) face. These results obtained from the interaction energy calculation are consistent with the results obtained from the crystallization experiments (Chapter 5.3).

It is noticeable that the interaction energies calculated with the COMPASS force field are much higher than the intermolecular interaction energies published in literature, e.g. by Atkins [ATK98]. The simulated interaction energies are up to 20 times (for dinitramide position on face (011)₁) the interaction energies listed in Table 6-3 for ion – ion interactions. Therefore, the absolute values of the interaction energies obtained from the calculation with the COMPASS force field are not considered as very reliable regarding the order of magnitude. The relative interaction energies are more meaningful in the case of ADN as the basic growth behaviour and growth rates of the different morphological important faces are explained by them.

Table 6-3: Intermolecular interaction energies specified by Atkins [ATK98]

interacting species	interaction energy [kJ/mol]	description
ion – ion	250	only between ions
A-H...B for A, B = N, O, F	20	hydrogen bonds
ion – dipole	15	between an ion and a stationary polar molecule
dipole – dipole	2	between stationary polar molecules
dipole – dipole	0.6	between rotating polar molecules
London (dispersion)	2	between all types of molecules

6.2.3 Experimental morphology versus simulated vacuum morphology

The next step is to compare the simulated vacuum morphologies with those obtained from crystallization experiments to identify the morphological important crystal faces that are defining the shape of the ADN crystals.

Preferentially, the crystals used for comparison were obtained from experiments where a low supersaturation was present to reduce the influence of kinetic effects on the crystal shape. The attachment energy method attempts to simulate the crystal habit as obtained under non-equilibrium growth conditions, however, from the gas phase and not the liquid phase. So it takes neither the solution as crystallization environment into account nor its non-equilibrium behaviour. Another critical point is that supersaturation is influencing the crystal growth mechanism and therefore also the crystal habit. This is demonstrated by Lu and Ulrich [LU05] for paracetamol from different solvents for low ($S < 1.07$) and high ($S > 1.11$) supersaturations.

For 1-propanol, all crystallization experiments showed low supersaturations throughout the whole cooling phase ($S_{MAX, 1-PROPANOL} = 1.07$) and the crystals obtained from these experiments all looked similar. The crystals from P-5-s and P-5-L were used for comparison. The angles that are measured on the microscopic pictures are compared to the angles of the simulated crystals (see Chapter 5.3.1) and thus the faces (100), (020) and (011) are identified as dominant faces. After taking a look at the SEM pictures, the crystal morphology was refined by considering the (110) face as a supplementary growth face defining the crystal shape.

Regarding the crystallization processes from 1-octanol, the lowest supersaturation is determined for O-5-s ($S_{MAX, O-5-s} = 1.11$). The (100), (020) and (011) faces can be identified by comparing the BFDH morphology and the microscopic picture of O-5-s. These faces are also found when ADN is recrystallized from 1-propanol. Additionally, the (002) face is present by crystallizing from 1-octanol. In the SEM pictures, the (110)-face is also detected for some crystals.

The comparison of the simulated BFDH and growth morphology with the experimental crystals shows that only the BFDH method is leading to suitable results. All faces that are present on the crystals from experiment are also found on the BFDH morphology. The growth morphology does not exhibit the (100) face which is identified as the morphological most important one on real ADN crystals. The reason for this may be that the COMPASS force field can not cope with ADN sufficiently in terms of charge and bond type determination. This topic is discussed in detail in Chapter 6.1.2.

In addition to the comparison of the included angles measured on the pictures, X-ray powder diffraction was carried out for ADN from 1-propanol, ADN from 1-octanol and a reference sample (see Chapter 5.2.5). The aim was to estimate preferred orientations caused by the crystal shape to identify the morphological important crystal faces (see

also Figure 6-5 for illustration). The preferred orientations of the samples were estimated on the basis of peak intensities compared to the reference sample.

In Table 6-4 the quotients of the normalized average peak intensities are shown. A quotient of 1 means that the reflexes of the recrystallized and the reference sample are developed equally. High values indicate preferred orientations; the correspondent crystal faces are preferentially parallel to the sample's surface. The intensity of the (100) face, including its higher order peaks, is 8.8 times (1-propanol) and 3.2 times (1-octanol) higher than the intensity of (100) peak of the reference sample. This proves that the dominant crystal face of ADN recrystallized from both 1-propanol and 1-octanol is (100). This is in accordance with the results obtained from the BFDH morphology calculation where the (100) face is the morphological important one.

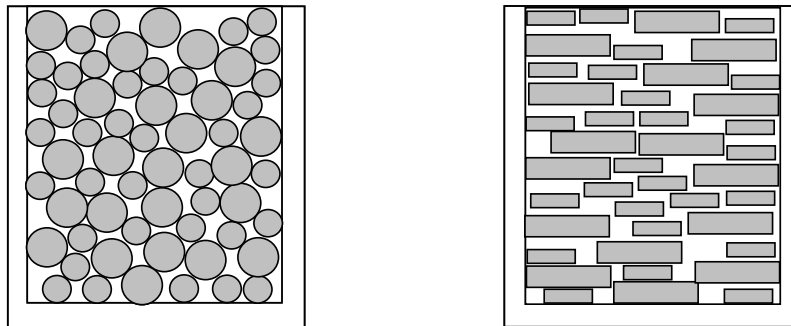


Figure 6-5: Reference sample with no preferred orientation (left), and ADN from crystallization experiments with a preferred orientation due to the crystal shape

Table 6-4: XRD: preferred orientations, quotients of the normalized intensities

face	(100)	(020)	(110)	(011)	(111)	(002)
1-propanol	8.8	0.2	1.1	0.1	0.1	0.1
1-octanol	3.2	1.5	0.7	0.2	0.2	0.3

The ADN morphology obtained from 1-propanol is compared to literature (Figure 6-6). Nagao [NAG98] published an ADN crystal habit defined by the faces (100), (110) and (111) whereas (100) is dominating the crystal shape (Figure 6-6 left). Both morphologies in Figure 6-6 provide a blade-shaped habit. They are defined by the (100) surface as hexagonal basis area. The upper and lower edges (related to Figure 6-6) are build of the (110) face ([NAG98], Figure 6-6 left) respectively the (110) and the (020) face (Figure 6-6 right). The (020) face is build of layers that are neutral in charge because they consist of both ammonium and dinitramide ions (see Chapter 5.1.3 Figure 5-8 right). In contrast to the (020) face, the (110) face is built of positive charged layers composed of ammonium ions and negative charged crystal layers composed of dinitramide ions whereas the layers are alternating. Crystal growth implies that the building blocks of the crystal are incorporated into the surface. Incorporation is eased when the building block is

attracted by the surface, e.g. by electrostatic forces, so it comes close to the particular surface and is placed on the appropriate lattice position. Because the (020) face is neutral in charge, it is more difficult for the building blocks to get part of the crystal. This results in a slow growth compared to the (110) face. For this reason, the (020) face was taken into account as a morphological important crystal face of ADN.

The ends of the blades or needle-shaped flat crystals are confined by the face (111) according to Nagao [NAG98]. By comparing the angles between the faces as described in RESULTS Chapter 5.3, the terminal crystal faces are indicated as (011) face. Both the (111) and the (011) face are possible faces for defining the ends of the crystals. Regarding the lattice plane spacing d_{hkl} of the two faces, the (011) face is the more probable one because of the larger interplanar distance ($d_{011} = 5.028 \text{ \AA}$, $d_{111} = 4.396 \text{ \AA}$). Nagao [NAG98] does not describe how the face indexing was done.

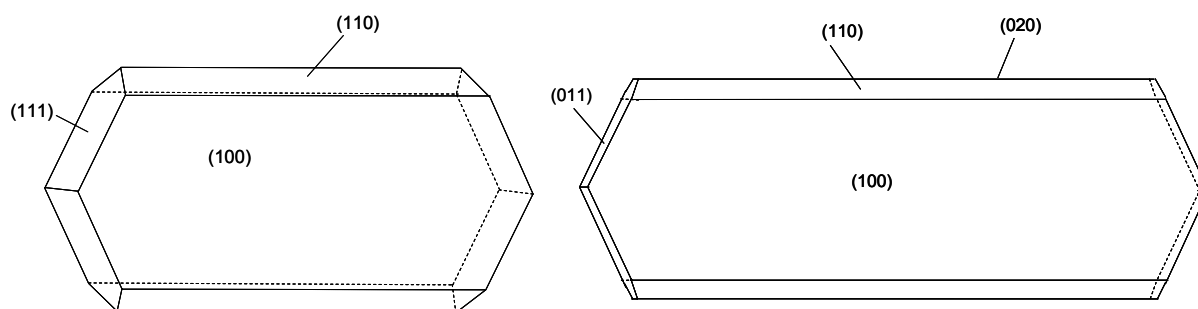


Figure 6-6: Left: ADN crystal habit described by Nagao [NAG97]
right: ADN morphology obtained by recrystallization from 1-propanol

6.3 Process monitoring

6.3.1 The application of the electrolytic conductivity measurement

6.3.1.1 Range of the measured data

By observing the EC values obtained from ADN / 1-propanol and ADN / 1-octanol solutions, it is attracting attention that the order of magnitude of the measured EC values is different for 1-octanol and 1-propanol (Table 6-5). EC_{REL} is calculated according to Equation 6-2 and gives the relative ECs based on the concentrations. The values for EC_{REL} are in the range of $EC_{REL} = 19 - 27$ (Table 6-5). This means that EC for ADN dissolved in 1-propanol is 19 to 27 times higher than EC for ADN dissolved in 1-octanol for equal concentrations.

EC is proportional to the ionic mobility v_{\pm} of the dissolved ions and to their grade of dissociation α (Equation 6-3). Equation 6-4 shows that one of the influencing factors on v_{\pm} is the dynamic viscosity η of the liquid. For the two solvents 1-octanol and 1-propanol, η was measured (see Chapter 5.2.4). A comparison of the viscosities for different temperatures (Table 6-6) shows that the maximum value for $\eta_{1-octanol} / \eta_{1-propanol}$

is 4.09. As EC is proportional to v_{\pm} , a maximum variation of EC by the factor 4.09 can emerge for the different solvents. Because EC is also depending on the dissociation grade α (Equation 6-3), the low $EC_{1\text{-octanol}}$ is also an indication that the dissociation of ADN in 1-octanol is much lower than the dissociation in 1-propanol. The dissociation grade of ADN in the two solvents was not qualified in this work. It can be concluded that the different orders of magnitude for $EC_{1\text{-octanol}}$ and $EC_{1\text{-propanol}}$ is caused by both the difference in the viscosities and different dissociation grades in the two solvents 1-propanol and 1-octanol.

$$EC_{REL} = \frac{EC_{1\text{-propanol}}}{EC_{1\text{-octanol}}} \cdot \frac{c_{1\text{-octanol}}}{c_{1\text{-propanol}}} \quad \text{Equation 6-2}$$

$$EC \propto \alpha \cdot v_{\pm} \propto \frac{\alpha}{\eta} \quad \text{Equation 6-3}$$

$$v_{\pm} = \frac{z_{\pm} \cdot e_0 \cdot \vec{E}}{6 \cdot \pi \cdot \eta \cdot R} \quad \text{Equation 6-4}$$

Table 6-5: Electrolytic conductivities for different ADN solutions

solvent	c [g/g]	EC [$\mu\text{S}/\text{cm}$]	T [$^{\circ}\text{C}$]	EC_{REL} [-]
1-propanol	0.04	1948	20	23
1-octanol	0.004	8.5	20	
1-propanol	0.04	2700	40	27
1-octanol	0.004	10.1	40	
1-propanol	0.12	4830	20	19
1-octanol	0.012	25.6	20	
1-propanol	0.12	7610	40	21
1-octanol	0.012	35.6	40	

Table 6-6: Comparison of the dynamic viscosities for 1-propanol and 1-octanol

T [$^{\circ}\text{C}$]	$\eta_{1\text{-propanol}}$ [mPa·s]	$\eta_{1\text{-octanol}}$ [mPa·s]	$\eta_{1\text{-octanol}} / \eta_{1\text{-propanol}}$
20	2.14	8.76	4.09
30	1.77	6.59	3.72
40	1.43	4.85	3.39

6.3.1.2 Solubility data

The electrolytic conductivity measurement was used for the determination of the solubility curves (Chapter 5.2.2). The results are compared to the solubility data obtained from the evaporation method described in Chapter 4.1.4.

Regarding ADN in 1-propanol (Chapter 5.2.2, Figure 5-20, right), the solubility obtained from evaporation and the data obtained from the EC measurement are in good agreement. The slightly higher values for $T = 35\text{ }^{\circ}\text{C}$, $37.5\text{ }^{\circ}\text{C}$ and $40\text{ }^{\circ}\text{C}$ may be explained by a loss of solvent caused by evaporation during the handling of the samples as 1-propanol is a volatile solvent.

By measuring the solubility of ADN in 1-octanol, the evaporation method and the EC measurement method show different results for higher temperatures (Chapter 5.2.2, Figure 5-21, right). This is because the evaporation of 1-octanol was not accomplished successfully in the vacuum drier for all samples. During the drying process, the solution was splashing out of the vessel and thus the mass of ADN was reduced. This led to an incorrect value for the saturation concentrations.

For both solvents, the saturation data obtained from EC measurement was used to determine the supersaturation that was present during the crystallization process.

6.3.2 Supersaturation and nucleation

One of the aims of this work was the monitoring of the crystallization processes of ADN for the solvents 1-propanol and 1-octanol. The determination of the supersaturation during the crystallization process was of special interest as it is a key parameter of crystallization processes. It was determined by comparing the equilibrium concentration for a definite temperature with the actual concentration obtained from the EC measurement by means of the characteristic curves (Chapter 5.2.1). By using a time switch, the stirrer was stopped and it was possible to measure the concentration of the particle free solution inside the vessel. The disadvantage of this method is that it is not possible to measure continuously. Data was acquired only every 10 minutes to minimize the number of interruption of the crystallization process. For the crystallization processes with a cooling rate of 10 K/h , only 13 measurements can be performed during the cooling phase, hardly enough to describe the development of supersaturation in detail. The number of interruptions was minimized because they can influence the crystallization process. The homogeneity of the solution is reduced when the stirrer is stopped and this leads to a change in heat and mass transfer conditions compared to a stirred system. The start of the stirrer can also damage the crystals as they accumulate on the bottom of the vessel and are in direct mechanical contact with each other.

The detection of nucleation respectively the appearance of particles with a chord length of $1\text{-}10\text{ }\mu\text{m}$ was carried out by laser backscattering with a Lasentec FBRM. This was done to verify the trend of supersaturation results as supersaturation must decrease

when nucleation takes place. In Figure 6-7 and Figure 6-8, the run of the supersaturation S and the number of particles detected during the processes P-5-L and O-10-L are shown as examples.

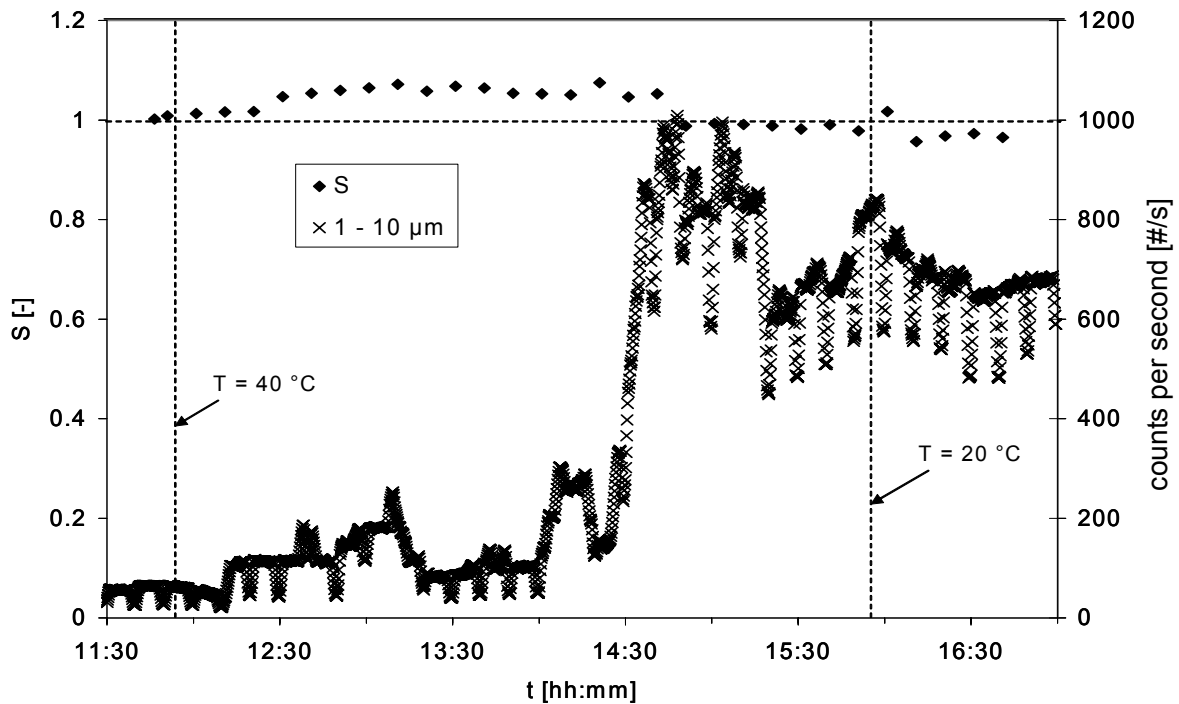


Figure 6-7: Process monitoring for P-5-L: direct compare of the development of the supersaturation S and the presence of particles with a chord length of 1-10 μm

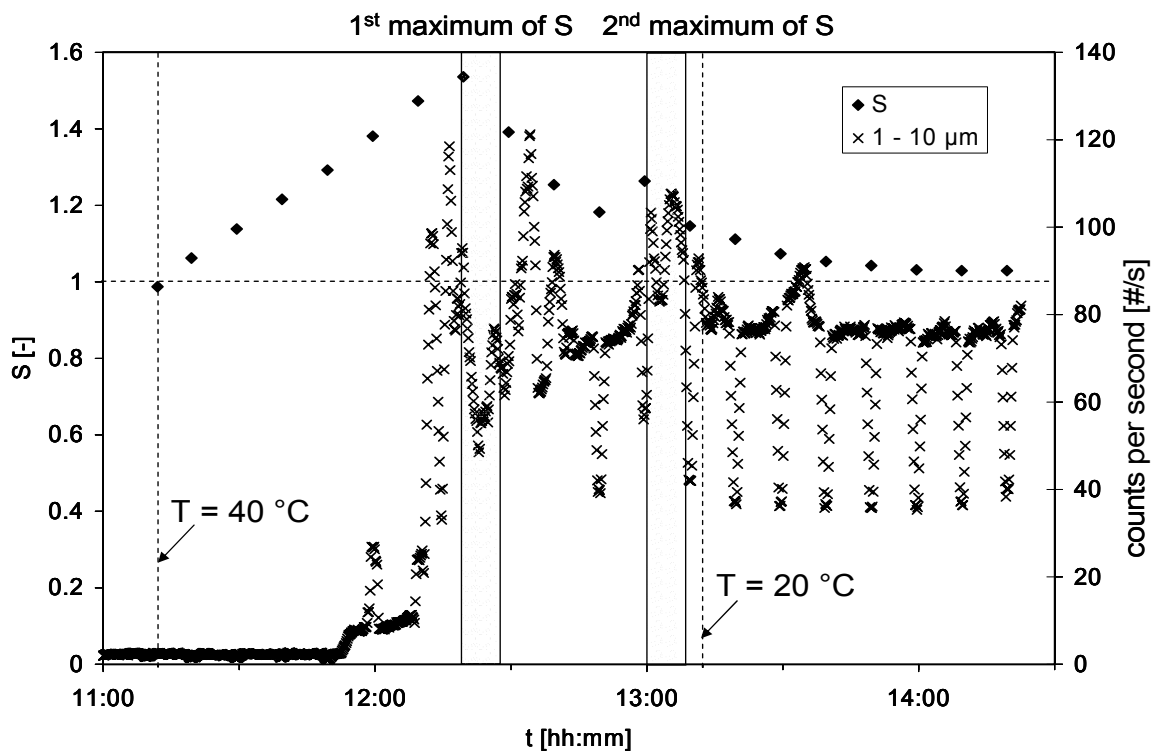


Figure 6-8: Process monitoring for O-10-L: direct compare of the development of the supersaturation S and the presence of particles with a chord length of 1-10 μm

6.4 Solvent crystallization of ADN

6.4.1 Choice of the solvents

The different morphologies of the ADN crystals obtained from natural cooling crystallization (Chapter 5.2.3.1 Figure 5-22 to 5-24) are showing that the solvent plays an important role in ADN crystallization as it influences the crystal shape to a large extent. Because 1-propanol turned out to be the most promising solvent in terms of a compact crystal shape, an alcohol screening (Chapter 5.2.3.2) was done subsequently. As result, plate shaped crystals with different length-width ratio were obtained. Because the recrystallized ADN showed the biggest difference in the length-width ratio for 1-propanol and 1-octanol, detailed crystallization experiments (Chapter 5.2.3.3 and 5.2.3.4) are carried out for these two solvents. In terms of length-width ratio of the crystals, 2-propanol would also be an adequate solvent because the recrystallized ADN is similar to the ADN from 1-propanol. 1-propanol was chosen because it is a primary alcohol and is therefore differing from 1-octanol only in the length of the carbon chain.

6.4.2 Crystal morphology

One of the main aims of this work is to investigate the influence of the solvent and the supersaturation on the crystal morphology of ADN. The results concerning crystal shape are discussed in this chapter.

By crystallizing ADN from 1-propanol, the morphologies of the ADN crystals are very similar for all experiments (Chapter 5.2.3.3, Figure 5-33 to 5-36). Plate-shaped crystals are obtained for both cooling rates and both experimental setups as shown in Figure 6-9.

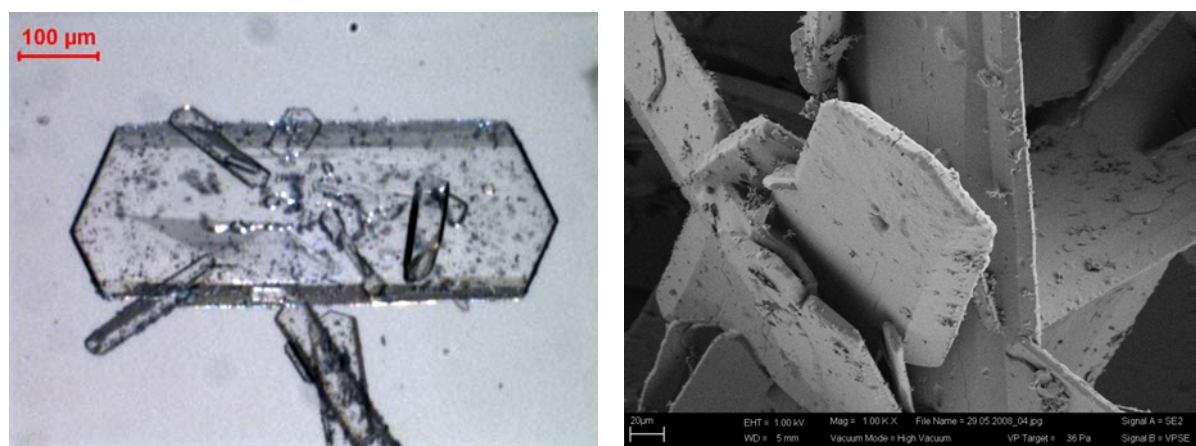


Figure 6-9: ADN from 1-propanol: left: P-5-L, right: P-10-L

The maximum supersaturation S_{MAX} of all four experiments (Chapter 5.2.3.3, Figure 5-43 and 5-44) is $S_{MAX} = 1.04 - 1.07$. The trend of supersaturation over the process time is also similar for all experiments. As there is no significant difference in supersaturation, which is the driving force of a crystallization process, the morphologies of ADN crystals

obtained from 1-propanol does not change under the chosen process conditions. It is noticeable that supersaturation is higher in the large-scale setup than in the small scale setup for both cooling rates.

The use of 1-octanol as solvent is leading to different supersaturation-depending crystal shapes and is discussed in the following.

Chapter 5.2.3.4, Figure 5-59 shows the EC measurements for all crystallization experiments. As there is no significant difference by comparing the trends of EC in O-5-L-#1 and O-5-L-#2 and the trends of EC in O-10-L-#1, O-10-L-#2 and O-10-L-#3, the supersaturation runs of the corresponding experiments are reproducible. For this reason only one data set is evaluated in terms of supersaturation for processes that are accomplished under the same conditions. The data for O-5-L is obtained from O-5-L-#2, the data for O-10-L from O-10-L-#2.

By cooling down with 5 K/h (experiments O-5-s and O-5-L), plate-shaped crystals are obtained from both experiments but with differently shaped basis areas (Chapter 5.2.3.4 Figure 5-45 to Figure 5-47). By taking a look at the supersaturations during the processes, it can be seen that the maximum supersaturation in O-5-s is $S = 1.11$ in contrast to the maximum supersaturation in O-5-L ($S = 1.18$). The variation of the experimental setup leads to a slight increase in supersaturation and to crystals with a different morphology.

The crystals obtained from cooling with 10 K/h are shown in Chapter 5.2.3.4, Figure 5-48 to 5-51. It is attracting attention that the crystals formed by the processes carried out with the higher cooling rate in the large-scale setup exhibit two different crystal morphologies. One fraction of the crystals is rod-shaped, the other plate-shaped similar to those obtained by slow cooling (O-5-L-#1 and O-5-L-#2) while the plates from O-10-L have a higher thickness. The variation of the morphologies resulting from one experiment can be explained by the range of supersaturation that is run through during the process. Two maxima of supersaturation are degraded both times by nucleation. This is shown in Chapter 6.3.2, Figure 6-8. It is not clear which crystal fraction is formed first. As the rod-shaped crystals are more voluminous than the plate-shaped crystals, it is supposed that they are occurring during the degradation of the first maximum of supersaturation. An indication for this statement is that the amount of dissolved ADN available is higher than the amount that is available when the second maximum of supersaturation is decomposed: The concentration is reduced from $c = 0.0180$ g/g to $c = 0.0114$ g/g ($\Delta c_{1st\ maximum} = 0.0066$ g/g) at the first maximum. At the second maximum, the concentration is reduced from $c = 0.0114$ g/g to $c = 0.0086$ g/g ($\Delta c_{2nd\ maximum} = 0.0028$ g/g). The concentration diagram is shown in Chapter 11, Figure 11-12. On the other hand, the number of plate-shaped crystals is larger compared to

the number of rod-shaped crystals. A large amount of small crystals is normally caused by nucleation at high supersaturations. This detail has to be clarified in future experiments by taking samples during the crystallization process.

It can be concluded that ADN from 1-propanol is of a plate-shaped morphology. It was not possible to influence the crystal shape by varying the experimental setup and the cooling rates that were used in this work. ADN from 1-octanol is sensitive to both the experimental setup and the cooling rates that induce different supersaturation during the processes. Different crystal shapes (rods, plate-shaped crystals with differently formed basis areas) are obtained from the processes.

6.4.3 Thermal analysis of recrystallized ADN

The thermal behaviour of ADN crystals resulting from crystallization experiments was analyzed by differential scanning calorimetry (DSC) and thermogravimetric analysis (TGA) (see Chapter 11, Table 11-4).

For the DSC analysis, the focus was put on the temperature range from 20 °C to 120 °C where the solid-liquid phase transition occurs. Due to the fact that the melting peak of the original ADN used in this work is a sharp endothermic peak with an onset temperature $T_{\text{ONSET}} = 92 - 93$ °C, changes in product quality are observable by a reduced onset temperature of the melting peak, a broadening of the melting peak and the appearance of additional peaks.

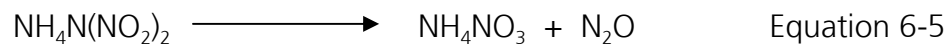
The TGA was evaluated in that way that $ML_{100\text{ °C}}$, the mass loss below 100 °C, is specified as well as the mass loss from 100 °C until the complete decomposition of the material. A clearly arranged overview on the DSC and TGA results of ADN obtained in the crystallization experiments is given in Table 6-7.

Table 6-7: Overview on the results of the thermal analysis of the recrystallized ADN

sample	H_{MELT} [J/g]	T_{ONSET} [°C]	$H_{\text{2nd PEAK}}$ [J/g]	$T_{\text{ONSET, 2nd PEAK}}$ [°C]	$ML_{100\text{ °C}}$ [%]
1-propanol, screening	145.8	93.47	-	-	0.442
2-propanol, screening	112.4	91.90	2.802	58.08	1.444
1-pentanol, screening	26.76	71.64	-	-	5.224
1-octanol, screening	145.2	93.43	-	-	1.868
P-5-s	136.1	91.98	6.147	59.44	0.750
P-5-L	38.49	71.70	-	-	7.170
P-10-s	153.6	93.72	-	-	5.241
P-10-L	153.1	93.53	-	-	0.344
O-5-s	119.4	91.58	6.336	59.02	0.956
O-5-L-#1	114.4	90.31	-	-	0.430
O-5-L-#2	90.97	86.89	-	-	1.559

sample	H _{MELT} [J/g]	T _{ONSET} [°C]	H _{2nd PEAK} [J/g]	T _{ONSET, 2nd PEAK} [°C]	ML _{100°C} [%]
O-10-s	155.5	94.00	-	-	0.923
O-10-L-#1	127.7	89.56	-	-	0.529
O-10-L-#2	23.57	74.33	-	-	6.888
O-10-L-#3	82.59	83.98	6.236	57.84	1.579

For some ADN samples, a second endothermic peak is observed at $T_{\text{ONSET}} = 57 - 60$ °C. As pure ADN does not show solid-solid phase transitions, this is an indication for the presence of at least one additional substance. The appearance of a second peak was also observed by Löbbecke [LÖB99] who investigated the thermal behaviour of ADN by DSC and TGA in detail. According to him, the second peak at $T = 55 - 65$ °C is caused by an endothermic phase transition of an eutectic mixture of ADN and ammonium nitrate (AN). With an increasing AN concentration, the phase transition enthalpy of the eutectic mixture is increasing and at the same time, the melt enthalpy of ADN is decreasing. The exothermic decomposition of ADN to AN starting at $T_{\text{ONSET}} = 127$ °C was published by Löbbecke et al. [LÖB97] while the actual composition of the gaseous side products is more complex than formulated in the simplified reaction that is shown in Equation 6-5. The formation of AN from ADN in the liquid phase is proofed to happen. In contrast to Löbbecke et al. [LÖB97], the ADN crystals that are investigated in this work are produced by solvent crystallization. This means that the temperature did not exceed $T_{\text{MAX}} = 45$ °C for 1-propanol and $T_{\text{MAX}} = 55$ °C for 1-octanol and is therefore much lower than $T_{\text{ONSET}} = 127$ °C. An energetic activation barrier $E_{\text{ACTIVATION}} = 1633.4$ J/g for the formation of a transition state, an energy gain $E_{\text{GAIN}} = -2210.5$ J/g by the formation of the nitrate ion from the transition state and a resulting overall energy $E_{\text{OVERALL}} = -577.1$ J/g was published by Politzer et al. [POL98] for the decomposition of ADN to AN. If it is possible to overcome the activation barrier in an ADN solution, the dissociation of ADN to AN will be possible.



The mass loss $\text{ML}_{100^\circ\text{C}}$ is listed in Table 6-7 because ADN is a hygroscopic substance and the weight loss below 100 °C can be referred to water present in the ADN samples. The water content of the raw ADN and the solvents was measured by Karl-Fischer-Titration when the experiments were carried out (see Chapter 11, Table 11-1 and 11-2). All experiments are carried out in an air-conditioned work room with a relative humidity of approximately 30 %. The laboratories where the DSC and TG measurements are carried out are not equipped with an appropriate air-condition and are therefore not convenient for hygroscopic substances. According to Wingborg [WIN06], the critical

relative humidity at $T = 25\text{ }^{\circ}\text{C}$ is $\varphi_{\text{CRITICAL},25^{\circ}\text{C}} = 55.1\%$. This means that storing, handling and processing of ADN must be done at a relative humidity below $\varphi_{\text{CRITICAL},25^{\circ}\text{C}}$ to maintain the original properties of an ADN sample. The ADN samples that show a significant $\text{ML}_{100^{\circ}\text{C}}$ do all have a reduced melt enthalpy and a broadened melt peak except for P-10-s. The influence of water on the crystal quality was not examined more closely in this work as the water content is most likely caused by the handling in not air-conditioned laboratories.

6.5 Conclusions

The following conclusions are made from this work:

- 1) The combination of the atom positions published by Gilardi et al. [GIL97] with the lattice parameters ICT/ANKA that are resulting from the measurement at the synchrotron source ANKA is reasonable. A model of the unit cell at $T = 295\text{ K}$ was generated and used as geometrical basis for the computer simulation.
- 2) The COMPASS force field is not appropriate for the treatment of the dinitramide ion and therefore for the ADN unit cell. The force field based calculation of the force field types and the atomic charges leads to unsuitable results. The total charge of the dinitramide ion is determined to $q_{\text{DN,COMPASS}} = 0$. Therefore force field types, the bonds and the atomic charges were applied manually to get a feasible model of the ADN unit cell.
- 3) The morphological important crystal faces calculated by the geometric BFDH method and those identified on the crystals from experiment are in coincidence. The dominance of the (100) face was also verified by powder XRD.
- 4) The growth morphology that was calculated by taking the attachment energies into account does not agree with the crystal shape from experiment. The most important crystal face (100) is not part of the calculated growth morphology.
- 5) The calculation of the interaction energies of the crystal faces with the building blocks and the solvent molecules show that there is no influence of the solvents on the crystal morphology caused by an inhibition of the incorporation of the building units into the crystal lattice.
- 6) ADN is not dissociated completely in 1-octanol due to the big difference of $EC_{1\text{-octanol}}$ and $EC_{1\text{-propanol}}$.
- 7) The process monitoring by EC and laser backscattering was successful. The supersaturation and the formation of particles can be observed by these methods. A continuous measurement of the concentration would increase the quality of supersaturation measurement.
- 8) The variation of the crystal shape is not possible by using 1-propanol as solvent. The application of 1-octanol in the crystallization processes leads to differently shaped crystals.

To sum up, there were two main aims defined in Chapter 3. The first objective was to find out to what extent the process parameters allow to influence the crystal shape. It was shown that the use of different solvents results in differently shaped crystals (Chapters 5.2.3.1 to 5.2.3.4). It is also demonstrated that supersaturation influences the growth conditions during the crystallization process and therefore the crystal shape. It can be concluded that crystallization is a reasonable tool towards ADN particles appropriate for propellant formulations.

The second focus was put on the prediction of the crystal morphology of ADN. It was demonstrated that it is possible to identify the morphological important crystal faces and their molecular structures by applying computer simulation methods. Additionally, the growth behaviour of the individual crystal faces can be related to the interaction energies calculated for the dominant faces and different molecules.

7 Summary

The oxidizer salt ADN is currently the only high performance oxidizer with the potential to replace AP. Progress was achieved in the formation of ADN particles with a shape suitable for the use in propellant formulations during the last years e.g. by the development of an emulsion prilling process and by the use of habit modifiers during solvent crystallization.

This work focuses on the crystallization of ADN from pure solvents without using additives. The crystallization behaviour with regard to the crystal morphology was the overall aim of this work.

Computer simulation methods were applied to calculate the morphology and to visualize the structure of the dominant crystal faces. The ab-initio force field COMPASS was used for all energy calculations.

The crystallization processes were monitored by two different testing methods: EC measurement was used to determine the ADN concentration and the supersaturation during the process. A laser backscattering method (Lasentec FBRM) was applied for the detection of the crystal formation. 1-Propanol and 1-octanol were selected as solvents for detailed experiments.

The recrystallized ADN was analyzed by SEM and microscopy and by thermal analysis methods (DSC and TGA).

The unit cell model was set up by using the atom positions from literature data in combination with the lattice parameters determined by XRD. The atomic charges of the dinitramide ion were calculated by DFT methods because COMPASS was not able to treat the dinitramide ion correctly.

The BFDH and the growth morphology were calculated with the generated unit cell model. The morphological most important crystal face (100) was identified by comparing the geometry of the simulated crystal shape with crystals obtained from experiment. This result was validated by XRD.

The crystallization of ADN from 1-octanol resulted in differently shaped crystals depending on the supersaturation during the process. At low supersaturations, plate-shaped crystals with a compact base area are obtained. High supersaturations lead to rod-shaped crystals but with a rough surface. Plate-shaped crystals resulted from all crystallization experiments with 1-propanol as solvent. The different cooling rates did not change the morphology.

The DSC of some ADN samples exhibited a second endothermic peak at about 60 °C what is an indication for the decomposition of ADN to ammonium nitrate. Mass losses

below 100 °C are ascribable to water present in the ADN samples. It is assumed that the water content is caused by handling the hygroscopic ADN samples in not appropriately air-conditioned work rooms.

It was shown that the COMPASS force is not suitable for ADN because the dinitramide ion was not considered sufficiently in terms of atomic charges and force field types.

The morphological important crystal faces calculated by geometric BFDH method and those identified on the crystals from experiment are in coincidence. Their molecular structures are confirming the growth behaviour of the ADN crystals.

A process monitoring was successfully established. EC and laser backscattering turned out to be a suitable combination for monitoring the crystallization process of the present systems. EC measurement showed that the dissociation grade of ADN in 1-octanol is much lower than the dissociation grade of ADN in 1-propanol.

In this work, the experimental results demonstrate that it is possible to influence the morphology of ADN by varying the temperature run and therewith the supersaturation during the process. This serves as a basis for continuative work in the field of crystallization of ADN.

8 Zusammenfassung

Ammoniumdinitramid (ADN), ein anorganisches Salz, ist zur Zeit der einzige Hochleistungsoxidator, der das Potential hat, Ammoniumperchlorat in Treibstoffformulierungen zu ersetzen. Bei der Herstellung von ADN-Partikeln mit einer für Formulierungen geeigneten Partikelform wurden in den letzten Jahren bereits Fortschritte erzielt, insbesondere durch die Entwicklung eines Emulsionskristallisationsprozesses und die Verwendung von Wachstumsmodifikatoren während der Lösungsmittelkristallisation.

Das übergeordnete Ziel dieser Arbeit ist die Untersuchung des Kristallisationsverhaltens von ADN im Hinblick auf die Kristallform. Das Hauptaugenmerk liegt hierbei auf der Kristallisation von ADN aus reinen Lösungsmitteln ohne Verwendung von Additiven.

Computersimulationsmethoden wurden angewendet, um Vakuummorphologien zu berechnen und um die molekulare Strukturen der vorherrschenden Kristallflächen aufzuklären. Das ab-initio-Kraftfeld COMPASS wurde für alle Energiebetrachtungen verwendet.

Die Kristallisationsprozesse wurden mit Hilfe zweier Messmethoden überwacht: Die Messung der elektrolytischen Leitfähigkeit diente dazu, die Konzentration von ADN und die daraus resultierende Übersättigung während des Prozesses zu ermitteln. Eine Laserrückstreuungsmethode (Lasentec FBRM) kam zum Einsatz, um die Partikelbildung zu detektieren. 1-Propanol und 1-Octanol wurden als Lösungsmittel für die Durchführung detaillierter Kristallisationsexperimente ausgewählt.

Das aus den Kristallisationsprozessen erhaltene ADN wurde mittels Rasterelektronenmikroskopie, Lichtmikroskopie und thermischer Analysenmethoden (DSC und TGA) untersucht.

Ein Modell der Elementarzelle wurde erstellt, indem die in der Literatur publizierten Atompositionen mit den Gitterparametern kombiniert wurden, die aus Röntgendiffraktometriemessungen hervor gingen. Die Atomladungen des Dinitramidions wurden mit Hilfe von DFT-Methoden berechnet, da sich das COMPASS-Kraftfeld für die Betrachtung des Dinitramidions als ungeeignet erwiesen hat.

Das Modell der Elementarzelle diente als Basis für die Berechnung der Morphologie nach der BFDH- und der Growth-Methode. Die morphologisch wichtigste Kristallfläche (100) ist durch den Vergleich der Geometrie der simulierten Morphologie mit den experimentell erhaltenen Kristallformen ermittelt worden. Dieses Ergebnis wurde zusätzlich durch die Röntgendiffraktometriemessungen verifiziert.

Abhängig von der Übersättigung während des Prozesses resultierten durch Kristallisation von ADN aus 1-Octanol Kristalle mit unterschiedlichen Morphologien. Bei niedrigen

Übersättigungen traten plättchenförmige Kristalle mit einer kompakten Grundfläche auf. Hohe Übersättigungen führten zu stäbchenförmigen Kristallen mit einer rauen Oberfläche. Die Kristallisation aus 1-Propanol führte in allen Experimenten zu plättchenförmigen Partikeln; die untersuchten Kühlraten hatten keinen Einfluss auf die Morphologie.

Die DSC-Analyse wies für einige ADN-Proben einen zweiten endothermen Peak im Bereich von 60 °C auf, was ein Zeichen für die Zersetzung von ADN zu Ammoniumnitrat ist. Die in der TGA detektierten Massenverluste für Temperaturen unter 100 °C wurden in den Proben vorhandenem Wasser zugeschrieben. Es wird angenommen, dass die Ursache des Wassergehalts die Handhabung des hygroskopischen ADN in nicht optimal klimatisierten Arbeitsräumen ist.

Zusammenfassend wurde gezeigt, dass das COMPASS-Kraftfeld für ADN aufgrund der unzureichenden Betrachtung des Dinitramidions bezüglich der atomaren Ladungen und der Kraftfeldtypen nicht geeignet ist.

Die morphologisch wichtigen Kristallflächen, die sich aus der Computersimulation mit der geometriebasierten BFDH-Methode ergaben, stimmen mit den Flächen überein, die an realen ADN-Kristallen identifiziert wurden. Ihre molekularen Strukturen bestätigen außerdem das Wachstumsverhalten der ADN-Kristalle.

Die Prozessüberwachung für die vorliegenden Stoffsysteme konnte erfolgreich durchgeführt werden. Die Messung der elektrolytischen Leitfähigkeit und die Laserrückstreuung stellen somit eine geeignete Kombination dar, um den Kristallisationsprozess von ADN aus 1-Octanol und 1-Propanol zu dokumentieren. Die Leitfähigkeitsmessung ergab außerdem, dass ADN in 1-Octanol zu einem wesentlich geringeren Grad dissoziiert ist als ADN in 1-Propanol.

Die experimentellen Ergebnisse dieser Arbeit demonstrieren, dass es möglich ist, durch Variation des Temperaturverlaufs und damit der Übersättigung während des Prozesses auf die Morphologie von ADN Einfluss zu nehmen. Dies dient als Grundlage für weiterführende Arbeiten auf dem Gebiet der Kristallisation von ADN.

9 Notations

latin symbols

a	[Å]	length of cell edges in direction a
b	[Å]	length of cell edges in direction b
c	[Å]	length of cell edges in direction c
c_{REAL}	[g/g]	actual concentration during the crystallization process
c_{EQU}	[g/g]	equilibrium concentration
d_{BOND}	[Å]	bond length
d_{hkl}	[Å]	interplanar spacing for face (hkl)
e	[C]	elementary charge
ΔE_{SYSTEM}	[kJ/mol]	energy difference after attaching the solvent to the face
$E_{\text{ACTIVATION}}$	[J/g]	activation barrier for the formation of a transition state
E_{ATT}	[kJ/mol]	attachment energy
E_{FACE}	[kJ/mol]	energy of the cleaved crystal face
E_{GAIN}	[J/g]	energy gain by the formation of the nitrate ion from the transition state
E_{SOLVENT}	[kJ/mol]	energy of the solvent molecule
E_{TOTAL}	[kJ/mol]	energy of the system consisting of the crystal face and the additive molecule
EC_{EQU}	[$\mu\text{S/cm}$]	EC of saturated ADN solution
EC_{PEAK}	[$\mu\text{S/cm}$]	peak values for EC while the stirrer is turned off
EC_{REL}	[-]	relative EC based on the concentration
h	[-]	Miller index, reciprocal axis intersection in direction a
H_{MELT}	[J/g]	melt enthalpy
H_{PEAK}	[J/g]	enthalpy corresponding to the peak area of a DSC measurement
k	[-]	Miller index, reciprocal axis intersection in direction b
$k_{\text{B+S}}$	[m/s]	coefficient for the birth and spread growth model
k_{BCF}	[m/(s·K)]	coefficient for the BCF growth model
$K_{\text{B+S}}$	[K ²]	coefficient for the birth and spread growth model
K_{BCF}	[K]	coefficient for the BCF growth model
l	[-]	Miller index, reciprocal axis intersection in direction c
m	[-]	axis intersection in direction a
m_{ADN}	[g]	mass of ADN
m_{SOLUTION}	[g]	mass of the solution, containing the solvent and ADN
m_{SOLVENT}	[g]	mass of the solvent

n	[-]	axis intersection in direction b
p	[-]	axis intersection in direction c
q_{DN}	[e]	charge of the dinitramide ion
$q_{\text{DN,COMPASS}}$	[e]	charge of the dinitramide ion, calculated with the COMPASS force field
$q_{\text{DN,DFT}}$	[e]	charge of the dinitramide ion, calculated by DFT methods
$r_{\text{B+S}}$	[m/s]	growth rate according to the birth and spread model
r_{BCF}	[m/s]	growth rate according to the BCF model
S	[-]	supersaturation
T	[°C]	temperature
$T_{\text{ICT/ANKA}}$	[K]	measuring temperature of ICT/ANKA
T_{MELT}	[°C]	melting temperature
T_{NUC}	[°C]	nucleation temperature
T_{ONSET}	[°C]	onset temperature of a peak of a DSC measurement
$T_{\text{ÖSTMARK}}$	[K]	measuring temperature of Östmark et al [ÖST00]
T_{SAT}	[°C]	saturation temperature
v_{\pm}	[m/s]	ionic mobility
V_{VESSEL}	[μL]	volume of the crystallization vessel
z_{\pm}	[-]	charge of an ion as the number of elementary charges

greek symbols

α	[-]	dissociation grade
α_{BOND}	[°]	bond angle
α_{TORSION}	[°]	bond torsion
β	[°]	interaxial lattice angle between basis vectors a and c
γ	[K ⁻¹]	volumetric thermal expansion coefficient
γ_{EXP}	[K ⁻¹]	volumetric thermal expansion coefficient from experiment
γ_{SORESCU}	[K ⁻¹]	volumetric thermal expansion coefficient from Sorescu's data
η	[mPa·s]	dynamic viscosity
φ	[-]	relative air humidity
θ	[°]	diffraction angle
σ	[-]	supersaturation

abbreviations

ADN	ammonium dinitramide
AM	ammonium ion
ANKA	Angströmquelle Karlsruhe
AP	ammonium perchlorate
AV	average
BCF	the Burton-Cabrera-Frank model
BFDH	the Bravais-Friedel-Donnay-Harker model
B+S	the birth and spread model
DFT	density functional theory
DSC	differential scanning calorimetry
DN	dinitramide ion
EC	electrolytic conductivity
FBRM	focused beam reflective monitoring
FOX-7	1,1-diamino-2,2-dinitroethylene
GAFF	generalized ABMER force field
ICT	Fraunhofer Institute for Chemical Technology
MAX	maximum
MIN	minimum
ML	mass loss
SEM	scanning electron microscope
TGA	thermogravimetric analysis
COMPASS	Condensed-Phase Optimized Molecular Potentials for Atomistic Simulation Studies
FFT	force field type
PTFE	polytetrafluorethylene
VDW	van-der-Waals
XRD	X-ray diffraction

other symbols

#	[-]	number of counts
---	-----	------------------

10 References

- [ACC04] Materials Studio 3.1 Help
- [ATK98] Atkins P.W., *Physical chemistry*, 6th edition (1998), Oxford University Press
- [BEA04] Beaucamp S., Bernand-Mantel A., Mathieu D., Agafonov V., *Ab initio solid-state heats of formation of molecular salts from ion packing and crystal modelling: application to ammonium crystals*, Mol. Phys., 102 (2004) 3, 253-258
- [BEN06] Benazet S., Jacob G., *Obtaining ammonium dinitramide (ADN) crystals, and crystals and the energetic composites containing them*, Patent WO 2006/108991 A2
- [BER85] Berkovitch-Yellin Z., *Toward an ab initio derivation of the crystal morphology*, J. Am. Chem. Soc. 107 (1985), 8239-8253
- [BRA13] Bravais A., *Etudes Crystallographiques*, Academie de Sciences (1913), Paris
- [CHR96] Christe K.O., Wilson W.W., Petrie M.A., Michels H.H., Bottaro J.C., Gilardi R., *The dinitramide anion $N(NO_2)_2^-$* , Inorg. Chem., 35 (1996) 5068-5071
- [DAV86] Davey R.J., *The role of solvent in crystal growth from solution*, J. Cryst. Growth 76 (1986) 637-644
- [DOC91] Docherty R., Clydesdale G., Roberts K.J., Bennema P., *Application of Bravais-Friedel-Donnay-Harker, attachment energy and Ising models to predict and understanding the morphology of molecular crystals*, J. Phys. D: Appl. Phys. 24 (1991) 89-99
- [FIE05] Fiebig A., Ulrich J., *Predicting the morphology of benzophenone crystals in the presence of additives*, Proceedings 16th International Symposium on Industrial Crystallization (2005) 399-404, ISBN 3-18-091901-9, Dresden, Germany
- [FRI07] Friedel G., Bull. Soc. Fr. Mineral. 30 (1907) 326
- [FUH05_1] Fuhr I., Teipel U., Ulrich J., *Molecular modelling of crystalline energetic materials*, Proceedings 16th International Symposium on Industrial Crystallization (2005) 453-458, ISBN 3-18-091901-9, Dresden, Germany
- [FUH05_2] Fuhr I., Heintz T., Kröber H., *Product design of energetic materials*, Chemical Engineering Transactions, 6 (2005) 413-418, ISBN: 88-900775-7-3

- [FUH07_1] Fuhr I., Kempa P.B., Herrmann M., Ulrich J., *Computer Simulation of ammonium dinitramide: State of the art*, Proceedings 38th International Annual Conference of ICT (2007), Karlsruhe, Germany
- [FUH07_2] Fuhr I., Reinhard W., *Crystallization of ammonium dinitramide –part 1: solvent screening*, Proceedings 38th International Annual Conference of ICT (2007), Karlsruhe, Germany
- [GID95] Gidasov B.V., *Crystal and molecular structure of dinitramide salts and acid-base properties of dinitramide*, Russ. J. Gen. Chem., 65 (1995) 6 906-913
- [GIL97] Gilardi R., Flippen-Anderson J., George C., Butcher R.J., *A new class of flexible energetic salts: The crystal structures of the ammonium, lithium, potassium and cesium salts of dinitramides*, J. Am. Chem. Soc., 119 (1997) 9411-9416 and supporting information herein
- [GNI93] Gnielinski V., Mersmann A., Thurner F., *Verdampfung, Kristallisation, Trocknung*, (1993) Vieweg Verlag, Braunschweig/Wiesbaden
- [GUA06] Guangyu Y., Kubota N., Zuoliang S., Louhi-Kultanen M., Jinfu W., *Crystal shape control by manipulating supersaturation in batch cooling crystallization*, Crystal growth & design, 6 (2006) 12 2799-2803
- [HAR55] Hartman P., Perdok W.G., *On the relations between structure and morphology of crystals I*, Acta Cryst. 8 (1955) 49 49-52
- [HAR80] Hartman P., Bennema P., *The attachment energy as a habit controlling factor*, J. Cryst. Growth 49 (1980) 145-156
- [HEI04] Heintz T., Pontius H., Teipel U., *Stabilized spherical particles of ammonium dinitramide (ADN)*, Proceedings 35th International Annual Conference of ICT (2004), Karlsruhe, Germany
- [HÜT96] *Hütte – Die Grundlagen der Ingenieurwissenschaften*, 30th edition 1996, Akademischer Verein Hütte e.V. (Ed.), Berlin
- [IBA03] Ibach H., Lüth H., *Solid-State Physics: an Introduction to Principles of Materials Science*, 3rd edition (2003), Springer Verlag, ISBN: 9783540438700
- [IWA94] Iwamoto N., *Molecular dynamics of binder-ADN interaction*, Proceedings of the ERDEC Scientific Conference on Chemical and Biological Defence Research, Aberdeen Proving Ground, Md., Nov.15-18 (1994), 493-500

-
- [JOH06] Johansson M., de Flon J., Petterson A., Wanhatalo M., Wingborg N., *Spray prilling of ADN and testing of ADN-based solid propellants*, 3rd Int. Conf. on Green Propellant for Space Propulsion, 17-20 September 2006, Poitiers, France
- [JUM] Datasheet 20.2930 JUMO Blackline LF-4C 4 electrode electrolytic conductivity measurement
- [KLE98] Kleber W., Bautsch H.-J., Bohm J., *Einführung in die Kristallographie*, 18th edition 1998, Verlag Technik, Berlin
- [LAC99] Lacmann R., Herden A., Mayer C., *Review: Kinetics of nucleation and crystal growth*, Chem. Eng. Technol. 22 (1999) 4 279-289
- [LEA01] Leach A.R., *Molecular Modelling – Principles and Applications*, 2nd Edition 2001, Pearson Education Limited
- [LIU96] Liu X.Y., Bennema P., *Prediction of the growth morphology of crystals*, J. Cryst. Growth, 166 (1996) 117-123
- [LÖB97] Löbbecke S., Krause H.H., Pfeil A., *Thermal analysis of ammonium dinitramide decomposition*, Propellants, Explos., Pyrotech. 22 (1997) 184-188
- [LÖB99] Löbbecke S., *Einsatz thermischer Analysenmethoden zur Charakterisierung neuer energetischer Materialien am Beispiel von Ammoniumdinitramid (ADN) und Hexanitrohexaazaisowurtzitan (HNIW)*, PhD, Universität Marburg, 1999, Fraunhofer-IRB-Verlag, Stuttgart
- [LU04] Lu J.J., *Predicting crystal morphology in the presence of additives by molecular modelling*, PhD, Martin-Luther-Universität Halle-Wittenberg, 2004, Shaker Verlag, Aachen.
- [LU05] Lu J.J., Ulrich J., *The influence of supersaturation on crystal morphology – experimental and theoretical study*, Cryst. Res. Technol. 40 (2005) 9 839-846
- [MAL99] Malesa M., Skupinski W., Jamroz M., *Separation of ammonium dinitramide from reaction mixture*, Propellants, Explosives, Pyrotechnics 24 (1999) 83-89
- [MEE91] Meenan P., Roberts K.J., Sherwood J.N., *Understanding and controlling the crystal morphology of some ionic crystals*, Powder Technology, 65 (1991) 219-225
- [MOR80] Mortimer C.E., *Chemie*, 3rd edition 1980, Georg Thieme Verlag, Stuttgart

- [NAG98] Nagao L.M., *Toward a habit modification of ammonium dinitramide*, dissertation 1998, Yale University
- [NIE97] Niehörster S., *Der Kristallhabitus unter Additiveinfluß: Eine Modellierungsmethode*, Dissertation, Universität Bremen (1997), Clausthal-Zellerfeld: Papierflieger 1997
- [ÖST00] Östmark H., Bemm U., Langlet A., Sandén R., Wingborg N., *The properties of ammonium dinitramide (ADN): Part 1, basic properties and spectroscopic data*, J. Energ. Mater. 18 (2000) 123-138
- [POL98] Politzer P., Seminario J.M., Concha M.C., *Energetics of ammonium dinitramide decomposition steps*, J. Mol. Struct. 427 (1998) 123-129
- [RIT03] Ritchie J.P., Zhurova E.A., Martin A., Pinkerton A.A., *Dinitramide ion: Robust molecular charge topology accompanies an enhanced dipole moment in its ammonium salt*, J. Phys. Chem. B, 107 (2003) 14576-14589
- [SCH04] Schmiech P., Ulrich J., *Improvement of a model for the crystal habit prediction by use of PBC-vectors*, Chem. Eng. Technol. 27 (2004) 7 733-736
- [SOR99] Sorescu D.C., Thompson D.L., *Classical and quantum mechanical studies of crystalline ammonium dinitramide*, J. Phys. Chem. B, 103 (1999) 6774-6782
- [SOR01] Sorescu D.C., Thompson D.L., *Quantum mechanical studies of pressure effects in crystalline ammonium dinitramide*, J. Phys. Chem. A, 105 (2001) 7413-7422
- [TEI00] Teipel U., Heintz T., Krause H., *Crystallization of spherical ammonium dinitramide (ADN) particles*, Propellants, Explosives, Pyrotechnics 25 (2000) 81-85
- [VAI00] Vainshtein B.K., Fridkin V.M., Indenbom V.L., *Structure of Crystals*, 3rd edition 2000, Springer Verlag, ISBN 9783540674740
- [VEL03] Velardez G.F., Alavi S., Thompson D.L., *Molecular dynamics studies of melting and liquid properties of ammonium dinitramide*, J. Chem. Phys. 119 (2003) 13 6698-6708
- [WIK08] http://en.wikipedia.org/wiki/Unit_cell
- [WIN06] Wingborg N., *Ammonium dinitramide - water: Interaction and properties*, J. Chem. Eng. Data 51 (2006) 1582-1586

11 Annex

Table 11-1: ADN batches: product specification, DSC analysis, potassium and water content

	ADN 2005-7014		ADN 2007-9003	
	specification	approved	specification	approved
ADN content	min 98 %	> 99 %	min 98 %	>98 %
T _{MELT}	min 92 °C	92 °C	min 92 °C	93.5 °C
T _{MELT} (ICT*) onset/peak	92.48 °C / 94.54 °C		92.22 °C / 93.34 °C	
H _{MELT} (ICT*)	144.8 J/g		156.9 J/g	
K content	-	-	max 0.4 %	0.2 %
K content (ICT*)	0.285 %		0.209 %	
water content*	0.067 %		0.047 %	

* measured at ICT

Table 11-2: Solvents used for alcohol screening

solvent	quality	purity	water content (specification)	maximum water content*
1-propanol	p.a.	> 99.5 %	< 0,05 %	0.088 %
2-propanol	dried	> 99.7 %	< 0,01 %	0.015 %
1-pentanol	p.a.	> 98.5 %	< 0,1 %	0.060 %
1-octanol	for synthesis	> 99 %	< -	-

* the maximum water content was measured when the crystallization experiments were finished. Karl-Fischer titration was applied for the solvents where the water content was specified by the manufacturer.

Table 11-3: Specification of the TetraCon 325 probe used for EC measurements

EC measurement		temperature measurement	
range	1 μ S/cm to 2 S/cm	range	-5 °C to +80 °C
# of electrodes	4	thermistor type	NTC (30K Ω / 25 °C)
electrode material	graphite	thermistor material	graphite
cell constant	0.475 cm ⁻¹ \pm 1,5%	sensor accuracy	\pm 0.2 K

Table 11-4: Standard analysis methods

Macroscopy
Z16 APO (Leica) Visualization of the crystal shape by operating with transmitted and reflected light and combination of both
Scanning electron microscopy
Supra 55 VP (Zeiss) Visualization of the crystal shape and the quality and habit of the crystal surface
X-ray powder diffraction
<ul style="list-style-type: none"> • ANKA synchrotron source, Karlsruhe Determination of the lattice parameters of ADN by X-ray diffraction methods for the construction of the molecular structure that provides the basis for computer simulation. • Bruker AXS D8, ICT laboratory Cu source, 2 Göbel mirrors (parallel beam optics) Determination of the dominant crystal faces using preferred orientations
Differential scanning calorimetry (DSC)
DSC Q1000 (TA Instruments) Determination of phase transitions (melting point and enthalpy) and decomposition behaviour during heating with a defined heating rate. The heating rate that was used was 5 K/min. Measurements carried out under argon atmosphere.
Thermogravimetric analysis (TGA)
TGA Q5000 (TA Instruments) Determination of solvent residues by measuring the weight loss during heating with a defined heating rate. The heating rate that was used was 5 K/min. Measurements carried out under nitrogen atmosphere.
Karl Fischer titration (volumetric)
795 KF Titrino and 703 Ti Stand (Metrohm) Measurement of the water content of ADN
Inductively Coupled Plasma Optical Emission Spectrometry (ICP-OES)
iCAP 6300 (Thermo) Measurement of the potassium content of ADN
Shear rate and temperature dependant dynamic viscosities
Rotation viscosimeter UDS 200 (Physica) Dynamic viscosities of 1-propanol and 1-octanol, shear-rate and temperature dependant

Table 11-5: Fractional atom positions of ammonium dinitramide, published by Gilardi et al. [GIL97]

	x	y	z
dinitramide ion			
O2A	0.02506	0.92697	0.24501
O2B	0.02272	0.80802	-0.05022
O3A	0.57344	0.85465	0.00026
O3B	0.30526	0.87465	-0.26368
N1	0.30866	0.89019	0.1442
N2	0.10816	0.87442	0.10163
N3	0.39147	0.86978	-0.05355
ammonium ion			
N4	0.7277	0.88407	0.5316
H1	0.781	0.9488	0.5576
H2	0.6577	0.8791	0.3958
H3	0.6517	0.8688	0.635
H4	0.8226	0.829	0.5327

Table 11-6: XRD of the ADN reference: Miller indices hkl, multiplicity of the face, peak positions in 2 θ -scale, intensities F²

h	k	l	multiplicity	d _{hkl} [Å]	2 θ	F ²
1	0	0	2	6.7894	13.029	0.037
0	2	0	2	5.9519	14.872	0.016
1	1	0	4	5.8976	15.010	1.042
0	1	1	4	5.0292	17.621	2.199
1	2	0	4	4.4756	19.821	0.002
1	-1	-1	4	4.4002	20.164	0.001
0	2	1	4	4.0586	21.882	0.06
1	1	1	4	3.7578	23.657	0.183
1	-2	-1	4	3.7058	23.995	0.45
1	3	0	4	3.4258	25.989	0.969
2	0	0	2	3.3947	26.231	0.081
1	2	1	4	3.2971	27.021	8.266
2	1	0	4	3.2645	27.296	0.118
0	3	1	4	3.2276	27.615	4.335
2	-1	-1	4	3.0550	29.209	3.515
1	-3	-1	4	3.0414	29.342	0.067
0	4	0	2	2.9759	30.003	9.888
2	2	0	4	2.9488	30.286	0.196
1	3	1	4	2.8031	31.901	0.021
2	-2	-1	4	2.7916	32.035	0.372
0	0	2	2	2.7744	32.240	0.625
1	0	-2	2	2.7478	32.560	0.057
1	4	0	4	2.7256	32.833	1.217
0	1	2	4	2.7020	33.129	0.185
1	-1	-2	4	2.6774	33.441	0.876
0	4	1	4	2.6226	34.162	1.301
2	1	1	4	2.6218	34.172	0.151
2	3	0	4	2.5795	34.750	0.01
1	-4	-1	4	2.5197	35.602	0.303

h	k	l	multiplicity	d_{hkl} [Å]	2θ	F^2
0	2	2	4	2.5146	35.676	1.103
1	-2	-2	4	2.4948	35.970	0.314
2	-3	-1	4	2.4723	36.308	3.37
2	2	1	4	2.4496	36.656	0.954
1	0	2	2	2.4198	37.124	0.695
1	4	1	4	2.3791	37.783	1.107
1	1	2	4	2.3713	37.912	0.785
2	0	-2	2	2.3678	37.970	0.364
2	-1	-2	4	2.3223	38.743	2.217
0	3	2	4	2.2737	39.606	1.245
3	0	0	2	2.2631	39.799	2.837
1	-3	-2	4	2.2590	39.875	2.083
1	5	0	4	2.2466	40.104	0.239
1	2	2	4	2.2416	40.197	0.553
2	4	0	4	2.2378	40.269	0.556
2	3	1	4	2.2253	40.504	0.719
3	1	0	4	2.2233	40.543	0.274
3	-1	-1	4	2.2031	40.931	0.282
2	-2	-2	4	2.2001	40.989	0.822
0	5	1	4	2.1879	41.229	0.009
2	-4	-1	4	2.1667	41.650	1.37
1	-5	-1	4	2.1271	42.463	0.198
3	2	0	4	2.1154	42.710	0.001
3	-2	-1	4	2.0980	43.082	0.006
1	3	2	4	2.0659	43.784	0.217
1	5	1	4	2.0404	44.360	0.647
2	-3	-2	4	2.0333	44.524	0.283
0	4	2	4	2.0293	44.617	0.337
1	-4	-2	4	2.0188	44.861	0.052
2	4	1	4	1.9947	45.434	0.037
0	6	0	2	1.9840	45.693	0.003

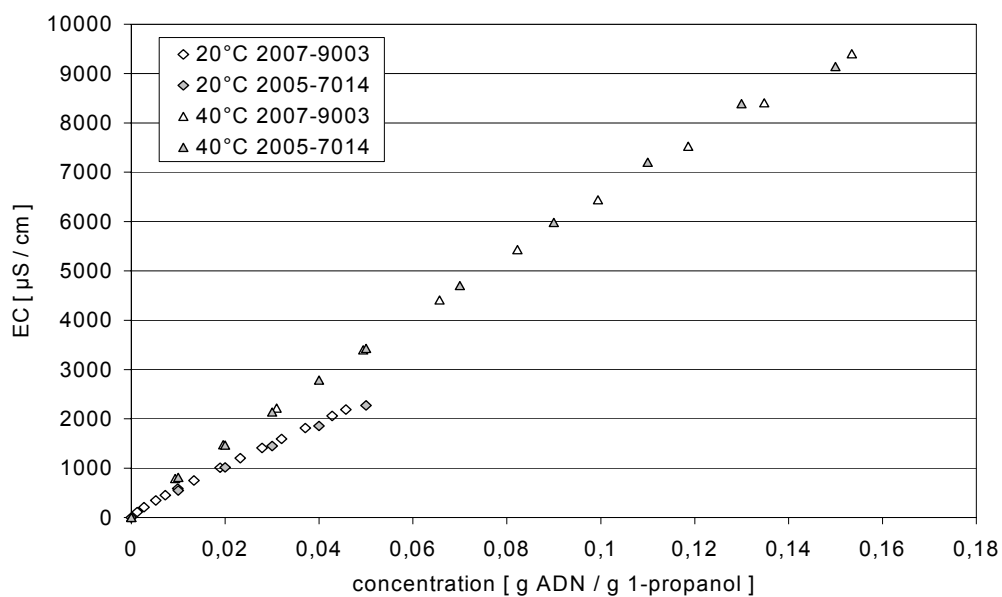


Figure 11-1: Comparison of the two ADN batches: EC measurement for defined concentrations at $T = 20\text{ °C}$ and $T = 40\text{ °C}$

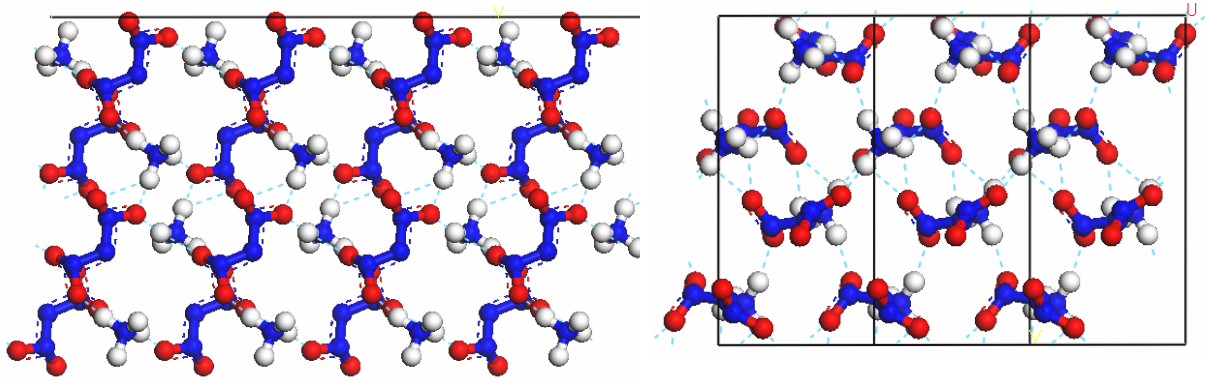


Figure 11-2: (100) face: molecular structure, two different views

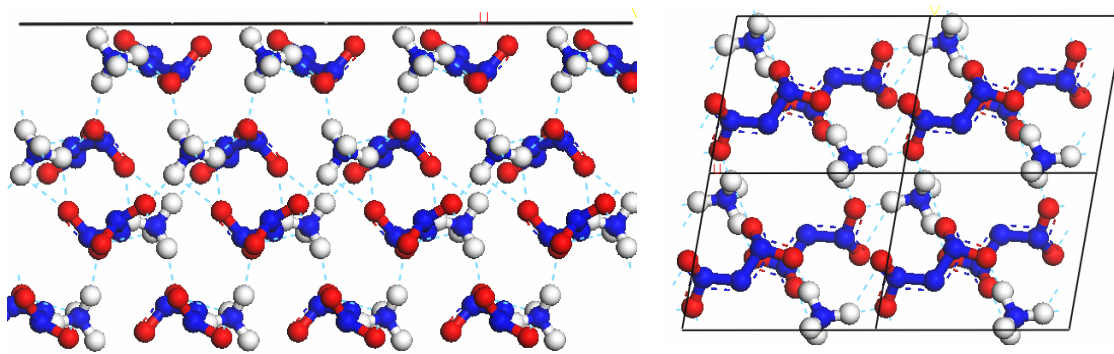


Figure 11-3: (020) face: molecular structure, two different views

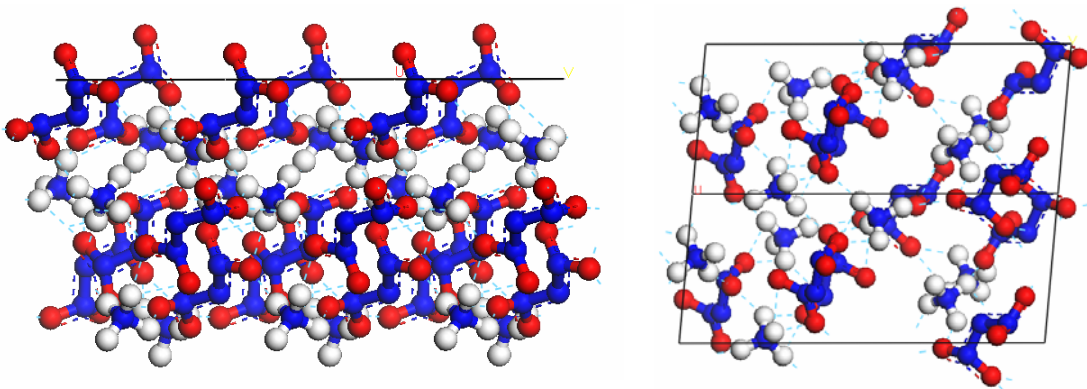


Figure 11-4: (110) face: molecular structure, two different views

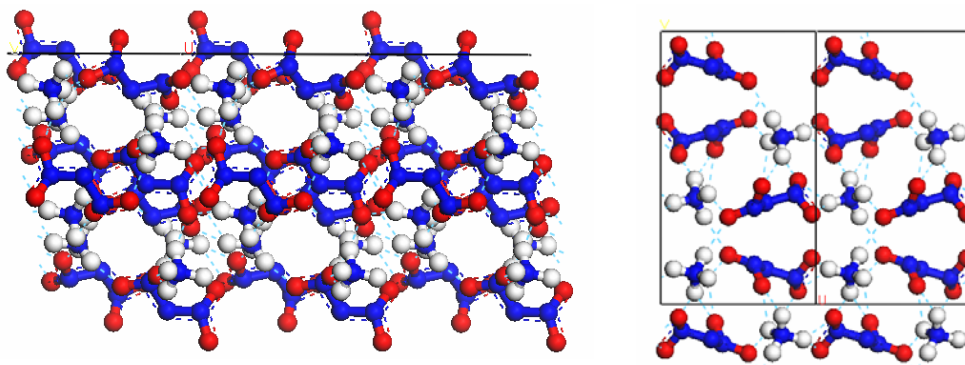


Figure 11-5: (011) face: molecular structure, two different views

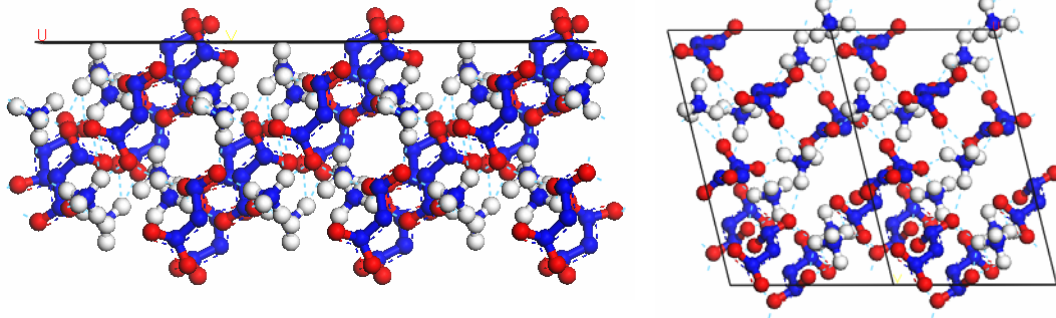


Figure 11-6: (11-1) face: molecular structure, two different views

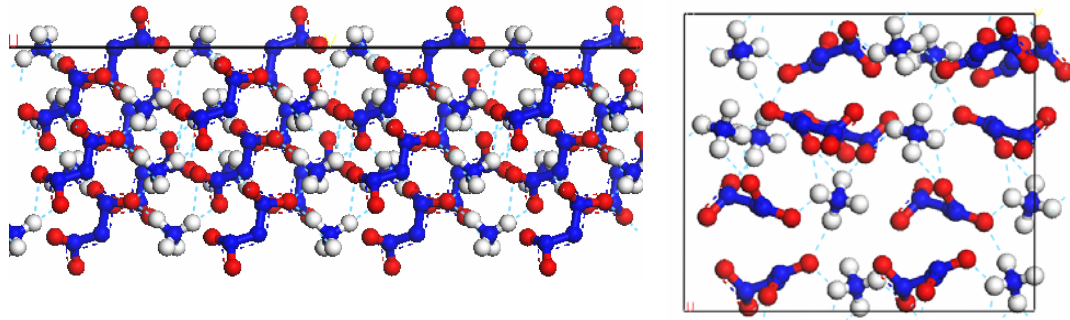


Figure 11-7: (10-2) face: molecular structure, two different views

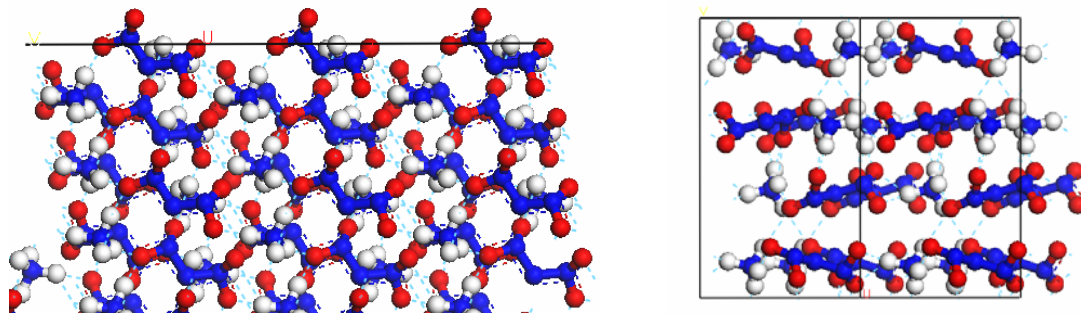


Figure 11-8: (002) face: molecular structure, two different views

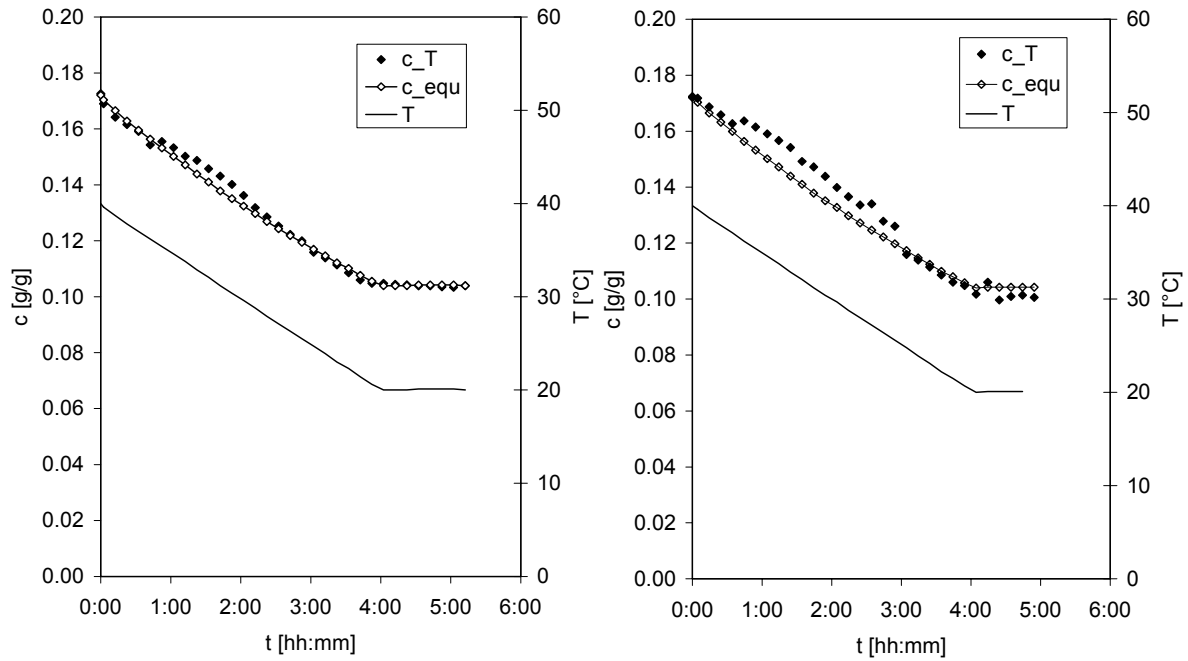


Figure 11-9: Process monitoring: Concentrations for P-5-s (left) and P-5-L (right)

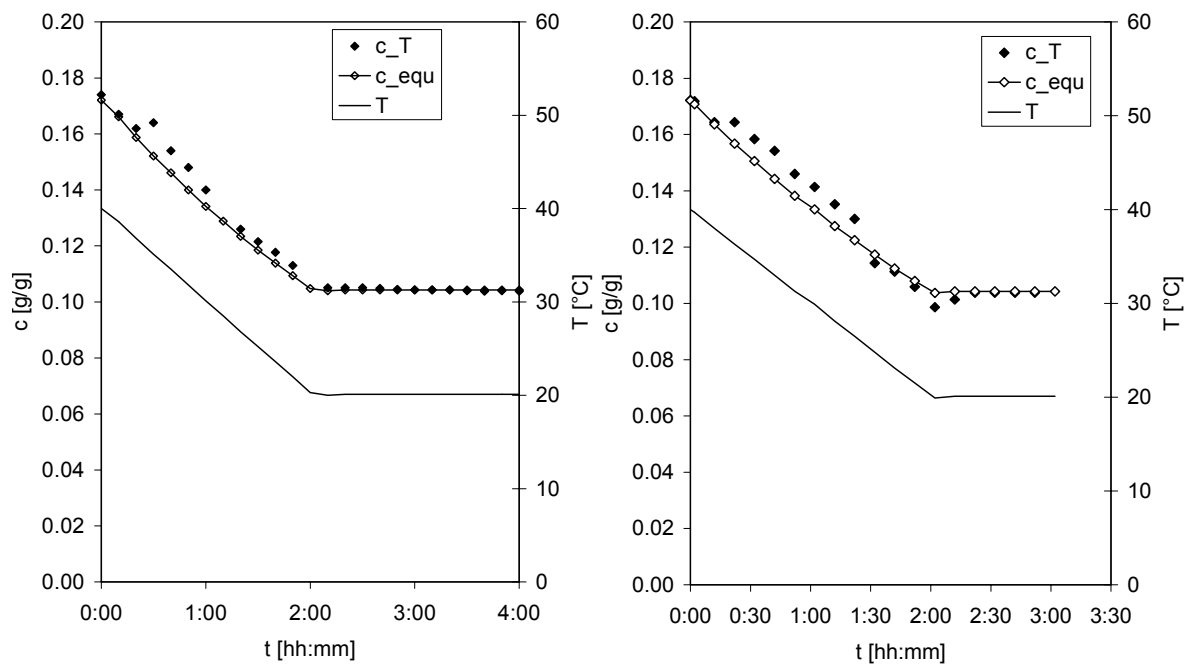


Figure 11-10: Process monitoring: Concentrations for P-10-s (left) and P-10-L (right)

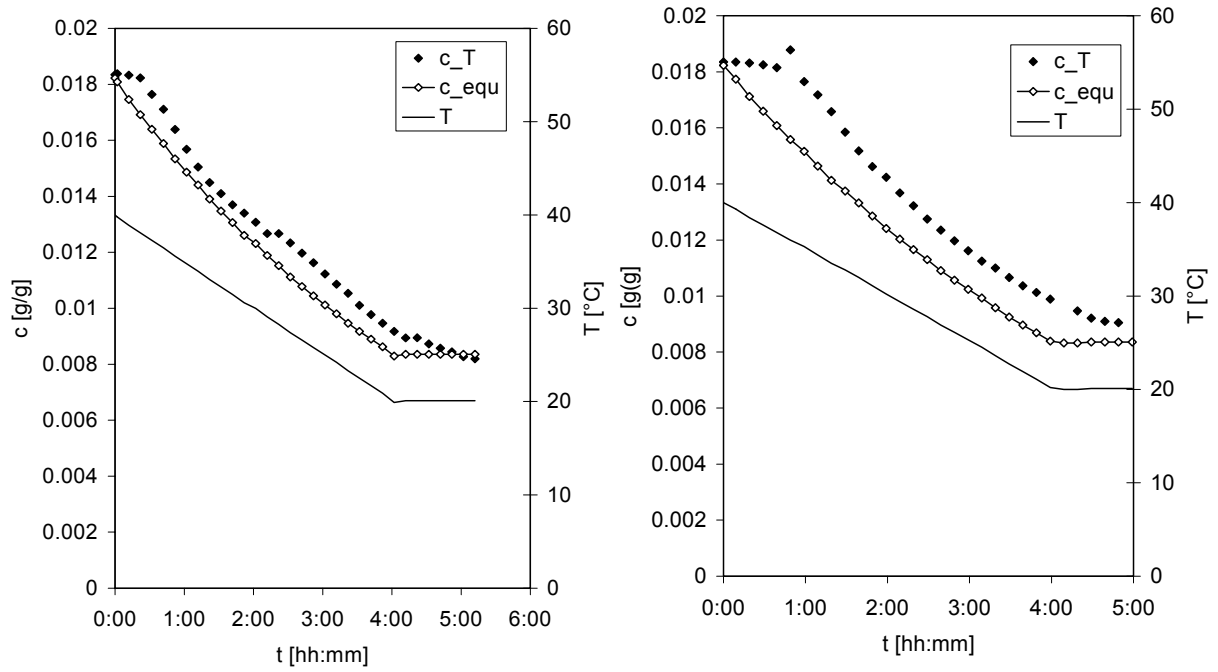


Figure 11-11: Process monitoring: Concentrations for O-5-s (left) and O-5-L (right)

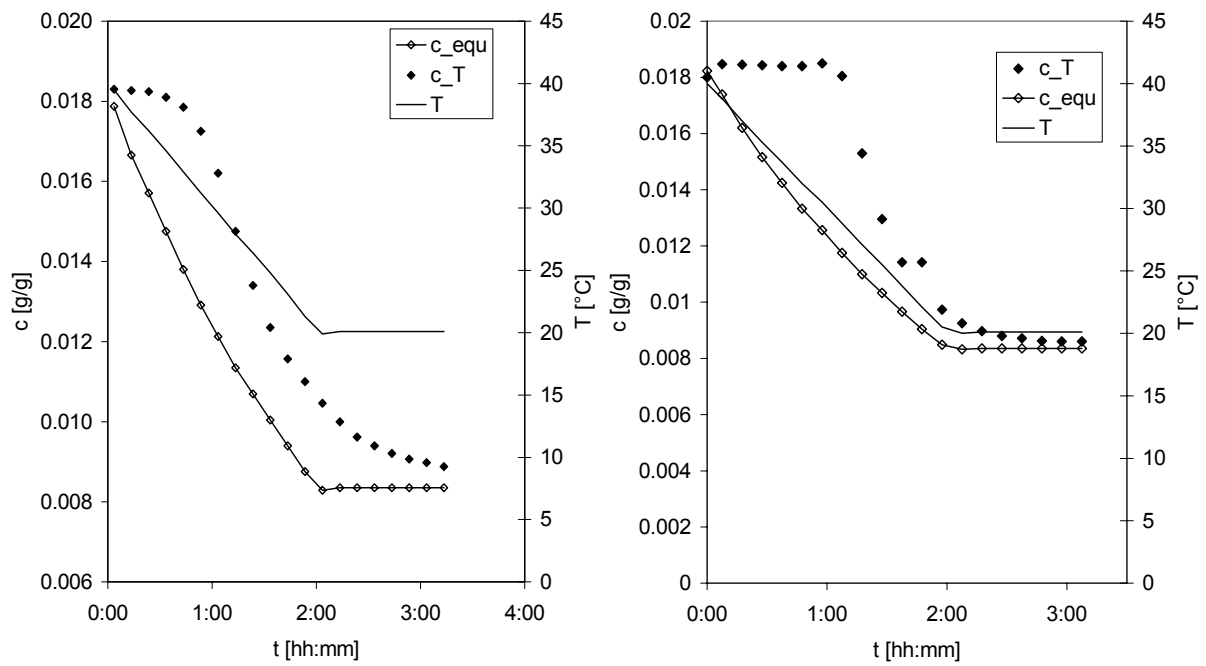


Figure 11-12: Process monitoring: Concentrations for O-10-s (left) and O-10-L (right)

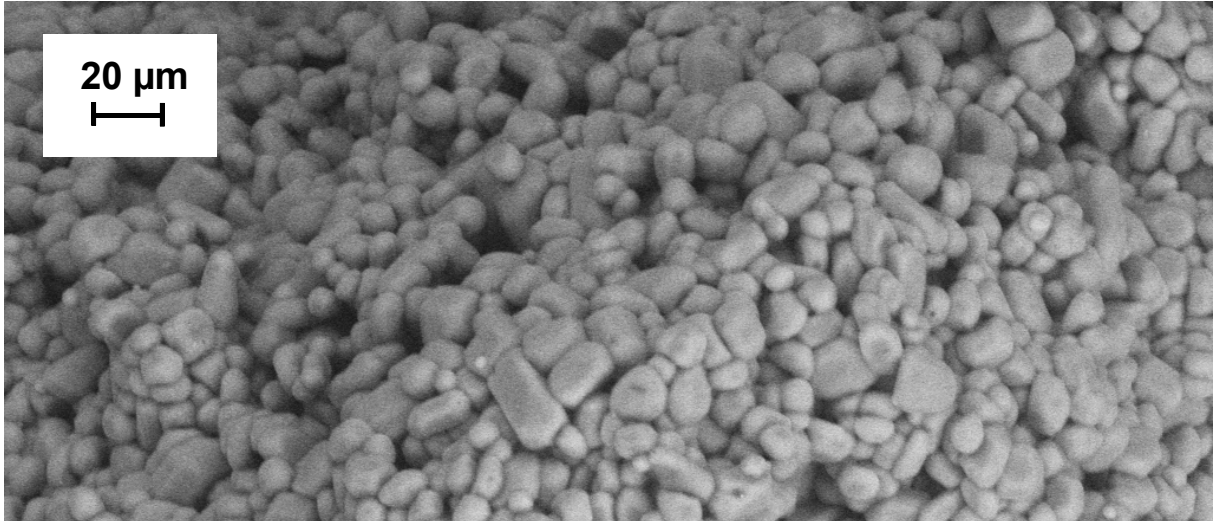


Figure 11-13: SEM of the ADN reference sample used for XRD

Lebenslauf

Angaben zur Person

Nachname: Fuhr
Vorname: Indra
Geburtsdatum: 04.01.1976
Geburtsort: Schwetzingen (Deutschland)
Nationalität: Deutsch

Ausbildung

08/82 – 07/86 Pestalozzi-Grundschule Hockenheim
08/86 – 07/95 Carl-Friedrich-Gauss-Gymnasium Hockenheim
Abschluss: Abitur
10/95 – 09/96 Physikstudium, Universität Karlsruhe
10/96 – 03/02 Studium Chemieingenieurwesen, Universität Karlsruhe
Abschluss: Diplom
seit 04/02 Wissenschaftliche Mitarbeiterin am Fraunhofer Institut für
Chemische Technologie (ICT), Pfinztal
09/02 Erstes Treffen und Beginn der wissenschaftlichen Betreuung durch
Prof. habil. Dr.-Ing. Joachim Ulrich
seit 10/05 Externe Doktorandin der Universität Halle-Wittenberg, Betreuer:
Prof. habil. Dr.-Ing. Joachim Ulrich

Indra Fuhr

Karlsruhe, den 11.08.08